UNIVERSITÀ DELLA CALABRIA

DEPARTMENT OF PHYSICS

Doctoral School "ARCHIMEDE" Science, Communication and Technology

Doctorate in
PHYSICS AND QUANTUM TECHNOLOGY

XXVIII Cycle

Financing by:
Secretaría de Educación Superior, Ciencia, Tecnología e Innovación
SENESCYT - ECUADOR

LOW DIMENSIONAL MATERIALS:

SYNTHESIS, CHARACTERIZATION AND APPLICATIONS

Scientific sector: FIS/01

Prof. Pietro Pantano	Prof. Lorenzo Caputi	Dr. Adalgisa Tavolaro
Coordinator	**Supervisor**	**Co-supervisor**

Biof. Diana Carolina Coello Fiallos

PhD Candidate

Italy, 2017

This thesis is dedicated to my dear parents
For their endless support, love
and encouragement.

Diana Carolina Coello Fiallos

Italy

ABSTRACT
(English Version)

This thesis was carried out at the laboratory of the Surface Nanoscience in the Department of Physics of University of Calabria, and at the Institute of Membrane Technology (ITM) of CNR, dealing the study of nanostructured systems with low dimensionality.

The first part of the work consisted in the synthesis and characterization of graphite oxide (GO), obtained by chemical oxidation and sonication of natural graphite. We used an innovative oxidation process with respect to those present in the literature, and the resulting material was studied by means of UV-visible and Infrared absorption spectroscopy, Raman and XPS spectroscopies, and by TEM and SEM microscopies. The sonicated graphite oxide (sGO) was tested for adsorption of dyes, with the aim to contribute to research in the field of the reduction of pollutants in the liquid phase. We used Methylene Blue, Acridine Orange and Cresyl Violet dyes, whose kinetics of adsorption on sGO was been meticulously studied by the UV-visible absorption spectroscopy. The results showed that the graphite oxide effectively absorbs the three dyes, and the chemical nature of the adsorption process was evidenced by means the kinetic simulations adopting different models.

The second part of the work relates to the synthesis of carbon-based nanostructures of the type "nano-onions" (CNOs), similar to multi-layer fullerenes, of great scientific and technological interest. The CNOs can be obtained by means of arc discharge between carbon electrodes immersed in deionized water. This method was used in this thesis work, and the produced carbonaceous nanomaterials have been characterized by Raman spectroscopy and TEM microscopy. Particular attention has been paid to those nanomaterials that contain a high percentage of CNO, since the arc discharge method also generates carbon nanotubes (CNT) and amorphous carbon. The main finding of the research was the identification of a solid agglomerate on the cathode, consisting almost exclusively of polyhedral CNOs and turbostratic graphite. The genesis of such CNOs is not attributable to a crystallization process of the carbon ions expelled from the plasma zone towards the surrounding water. The evidence of the fact that during the discharge the cathode remains at a temperature certainly lower respect to the anode, has permitted to hypothesize the CNOs training process, in which the carbon ions crystallize in the presence of a temperature gradient in the immediate vicinity of the cathode surface.

In the last part of this research activity, I investigated a crystal of Indium Selenium (InSe) by means of different electron spectroscopies, in ultra-high vacuum conditions. Through electron energy loss spectroscopy (EELS) the electronic properties of InSe and its reactivity towards oxygen and air have been studied. The results have allowed to identify

the most relevant transitions between electronic states in good agreement with existing theoretical calculations of the electronic structure and density of states. Experimental observations have also shown that the material is very stable with respect to possible oxidizing agents.

ABSTRACT
(Italian Version)

Questo lavoro di tesi è stato svolto presso il laboratorio di Nanoscienza di Superficie del Dipartimento di Fisica dell' Università della Calabria, e presso L'instituto di Tecnologia delle Membrane (ITM) del CNR, occupandomi dello studio di sistemi nanostrutturati a bassa dimensionalità.

La prima parte del lavoro è consistita nella sintesi e nella caratterizzazione di ossido di grafite (GO) ottenuto mediante ossidazione chimica di grafite naturale e sonicazione. Si è utilizzato un procedimento di ossidazione innovativo rispetto a quelli presenti in letteratura, e il materiale risultante è stato studiato mediante spettroscopia di assorbimento UV-visible e Infrarosso, spettroscopie Raman e XPS e mediante microscopia TEM e SEM. L'ossido di grafite sonicato (sGO) è stato testato come possibile adsorbente di coloranti, con il fine di contribuire alla ricerca nel campo della riduzione degli inquinanti in fase liquida. Sono stati utilizzati i coloranti methylene blue, acridine orange e cresyl violet, la cui cinetica di adsorbimento sul "sGO" è stata meticolosamente studiata mediante la spettroscopia di assorbimento UV-visible. I risultati hanno dimostrato che l'ossido di grafite assorbe efficacemente i tre coloranti, e la simulazione della cinetica mediante diversi modelli ha dimostrato che l'adsorbimento è di tipo chimico.

La seconda parte del lavoro si riferisce alla sintesi di nanostrutture a base di carbonio del tipo "nano-onions" (CNOs), simili a fullereni multistrato, di grande interesse scientifico e tecnologico. I CNOs possono essere ottenuti mediante scarica ad arco tra elettrodi di carbonio immersi in acqua deionizzata. Questo metodo è quello utilizzato in questo lavoro di tesi, e i nanomateriali carboniosi prodotti sono stati caratterizzati mediante spettroscopia Raman e microscopia TEM. In particolare l'attenzione è stata rivolta alla ricerca di quei nanomateriali che contenessero una percentuale elevata di CNO, in quanto il metodo di scarica ad arco genera anche nanotubi di carbonio (CNT) e carbonio amorfo. Il risultato principale della ricerca è stato l' individuazione di un agglomerato solido aderente al catodo, consistente quasi esclusivamente di CNO, di tipo poliedrico e con pareti simili a grafite turbostratica. La genesi di tali CNO non è attribuibile a un processo di cristallizzazione degli ioni di carbonio espulsi dalla zona plasmatica verso l'acqua circostante. L' evidenza del fatto che durante la scarica il catodo resta a una temperatura sicuramente inferiore a quella dell'anodo, ha permesso di ipotizzare il possibile processo di formazione dei CNO, nel quale gli ioni di carbonio cristallizzano in presenza di un gradiente di temperatura nelle immediate vicinanze della superficie del catodo.

L'ultima parte dell'attività di ricerca riguarda lo studio, mediante tecniche di spettroscopia elettronica in ultra-alto vuoto, di un cristallo di Indio Selenio (InSe).

Mediante la spettroscopia di perdita di energia degli elettroni (EELS) sono state studiate le proprietà elettroniche dell'InSe, e la sua reattività rispetto all'ossigeno e all'aria. Dai risultati prodotti è stato possibile individuare le principali transizioni elettroniche tra gli stati del cristallo e caratterizarne la loro natura. E' stato inoltre dimostrato un ottimo accordo tra le transizioni osservate sperimentalmente e quelle previste da calcoli teorici di struttura a bande e densità degli stati. Le nostre ossevazioni hanno dimostrato altresì che il materiale è molto stabile rispetto a possibili agenti ossidanti.

ABSTRACT
(Spanish Version)

Esta tesis se llevó a cabo en el laboratorio de la Nanociencia Superficial del Departamento de Física de la Universidad de Calabria y en el Instituto de Tecnología de Membranas (ITM) de CNR, enfocada al estudio de sistemas nanoestructurados de baja dimensionalidad.

La primera parte del trabajo consistió en la síntesis y caracterización del óxido de grafito (GO), obtenido por oxidación química y sonicación de grafito natural. Se utilizó un innovador proceso de oxidación con respecto a los que se encuentran en literatura y el material resultante se estudió mediante espectroscopia de absorción UV-visible e infrarrojo, espectroscopia Raman y XPS y a través microscopía TEM y SEM. El óxido de grafito sonicado (sGO) fue probado para la adsorción de colorantes, con el objetivo de contribuir a la reducción de contaminantes en la fase líquida. Estudiamos los colorantes azul de metileno, naranja de acridina y violeta de cresilo, cuya cinética de adsorción en sGO fue meticulosamente estudiada por la espectroscopia de absorción UV-visible. Los resultados mostraron que el óxido de grafito absorbe eficazmente los tres colorantes, y la naturaleza química del proceso de adsorción se evidenció mediante las simulaciones cinéticas adoptando diferentes modelos.

La segunda parte del trabajo se refiere a la síntesis de nanoestructuras basadas en carbono, del tipo "nano-onions" (CNOs) que son similares a fullerenos multicapa, de gran interés científico y tecnológico. Las CNOs se pueden obtener por medio de descarga de arco entre dos electrodos de carbono sumergidos en agua desionizada. Este método fue utilizado en este trabajo de tesis, y los nanomateriales de carbono producidos se han caracterizado por espectroscopia Raman y microscopía TEM. Se ha prestado especial atención a aquellos nanomateriales que contienen un alto porcentaje de CNO, ya que el método de descarga de arco también genera nanotubos de carbono (CNT) y carbono amorfo. El principal hallazgo de la investigación fue la identificación de un aglomerado sólido sobre el cátodo, constituido casi exclusivamente por CNO poliédricos y grafito turbo estatico. La génesis de tales CNO no es atribuible a un proceso de cristalización de los iones de carbono expulsados de la zona de plasma hacia el agua circundante. La evidencia del hecho de que durante la descarga el cátodo permanece a una temperatura ciertamente inferior respecto al ánodo, ha permitido plantear el proceso de formación de CNOs, en el cual los iones carbonos cristalizan en presencia de un gradiente de temperatura en la proximidad inmediata de la superficie del cátodo.

En la última parte de mi tesis esta actividad de investigación sobre un cristal de indio selenio (InSe), por medio de diferentes técnicas de espectroscopias electrónica de electrones en condiciones de ultra alto vacío. A través de la espectroscopia electrónica de pérdida de energía (EELS) se han estudiado las propiedades electrónicas de InSe y su

reactividad hacia el oxígeno y el aire. Los resultados han permitido identificar las transiciones más relevantes entre los estados electrónicos en buen acuerdo con los cálculos teóricos existentes de la estructura electrónica y la densidad de estados. Las observaciones experimentales han mostrado también que el material es muy estable con respecto a posibles agentes oxidantes.

ACKNOWLEDGEMENTS

All praises and thanks are to *Gloria Fiallos*, my dear and brave mommy, for help me to complete a goal more in mi life.

I would like to express my sincere gratitude to my advisors, *Prof. Lorenzo Caputi and PhD. Adalgisa Tavolaro* for their encouragement, kind support, enthusiastic attention, critical discussions, valuable advice and guidance. Also, I would like to express my sincere gratitude to Department of Physic and ITM-CNR for support me during my research.

I deserve my special thanks to my dear friends for their great assistance that really made my life very easy in Italy, in special to Dr. Dafni Mora, Dr. Yesenia Cevallos, Ing. Margarita Mayacela and PhD. Lorena Molina. I wish to give my special thanks to my dear brother Marquito for his constant encouragement during sad moments.

My deep gratitude is to my all seniors, friends and juniors for their constant encouragement.

I can't forget to praise my mother and father, Gloria and Marco, who gave me the vision to pursue for higher studies in other country and provided a ground to succeed in my life. Also I would like to give my very special thanks to my wonderful aunt Rosa, for her deep love, real care and encouragement at all times.

TABLE OF CONTENTS

CHAPTER 4

LIST OF FIGURES

LISTA OF TABLES

CHAPTER 1

TOP- DOWN APPROACH

CHEMICAL synthesis TO PRODUCE Graphite OXIDE

1 Chemical Synthesis to Produce Graphite Oxide

1.1 Introduction

In the world, human activity has changed our environment; there is currently a global effort to understand the influence of human activities on the environment and to look for new technologies to diminish both health and environmental problems. Among the different strategies to address these pressing challenges, recent developments in the field of nanotechnology increased attention on using the unique and promise properties of nanomaterials for several applications.

Two dimensional (2D) material studied in last years is *graphene*, which is composed of a single layer of carbon atoms arranged in a sp^2 bonded aromatic structure. In nature, graphene is found as the building block of graphite [1], where p-stacking of graphene sheets holds the lamellar graphite structure strongly in place with an interlayer spacing of 0.34 Å between the sheets. Graphite can be exfoliated to generate single layers of graphene [2–4], this procedure was initially demonstrated when Novoselov and Geim isolated the ***first single layer 2D material***, by micromechanical exfoliation [3]. Graphene produced by micromechanical exfoliation (Figure 1.1) presents a very high quality, ideal for the study of the properties of monolayer or bilayer graphene, showing remarkable electronic, thermal and mechanical properties [5–7].

A variety of applications have been demonstrated for graphene materials, such as structural nanocomposites [8–10], catalyst supports [11], electronic devices [12], and energy storage in batteries and supercapacitors [13, 14].

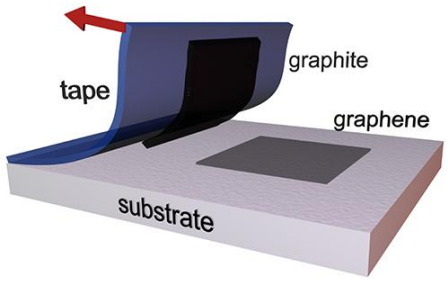

Figure 1.1 Schematic representation of micromechanical exfoliation of graphite.

In the 21st century the wonderful properties of graphene have been known and studied deeply. Numerous researchers have focused their studies on this material and more properties and applications for this Nobel material have been found regularly. One of the important focus in research is the production of this novel material. For the scalable production at low cost, the best way is using natural graphite. Graphene has then become a new super star after the famous carbon nanotube (CNT) in the carbon world. One of the biggest challenges was the large scale production of graphene after the first method performed by Geim's group. Different strategies to produce graphene have been introduced, and some of them with advantages and disadvantages, including metal ion intercalation, liquid phase exfoliation of graphite, Chemical Vapor Deposition (CVD) [2, 15–17], and the most widely used chemical reduction of Graphene Oxide (RGO) [18–20]. The oxidation of graphite was believed to be one of the three most promising pathways to obtain graphene, mainly due to its wet chemical processability and large scale availability. Graphene oxide is not a naturally occurring compound; the history of oxidation of graphite can be dated back to over one hundred and fifty years ago, when graphite was treated with oxidizing reagents, and after when graphene emerged in 2004, the researcher returned to use these process and called the final product graphene oxide.

Several experiments on graphene production were conducted to improve the chemical processes, and to make it possible to obtain a large amount of graphene oxide flakes in solution. We believe that GO powder or GO film is basically graphite oxide, then in the thesis content, we will abbreviate both Graphite Oxide and Graphene Oxide as GO,

as there is no significant difference between them, even in the context of electronic structures and properties [18] but the case is different for graphite and graphene.

1.2 Oxidation of Graphite

To discuss about graphene oxide, it is first necessary to consider the graphite oxide, which was successfully fabricated in a laboratory one and half centuries ago by Brodie [21]. Generally, GO sheets can be obtained between exfoliating of graphite oxide.

The most common method used to produce GO from graphite involves potassium permanganate ($KMnO_4$) as an oxidizing agent in concentrated sulfuric acid (H_2SO_4). Different reactions have been proposed to increase the yield and reduce the emission of toxic gases emitted during the reaction of oxidation but $KMnO_4$ remains the most frequently used oxidant in the chemical production of GO [22–24]. The oxygen-rich carbonaceous material obtained through the oxidation of graphite with strong oxidants, consists of randomly distributed regions of unoxidised (aromatic) graphene and regions of aliphatic six-membered rings, rich in oxygen-containing functional groups (Figure 1.2), including epoxys, hydroxyls carbonyl and carboxyl groups [1, 25]. The structure reported after oxidizing graphite results as being a good adsorbent for contaminated water and this property is widely studied to improve technologies for the environment.

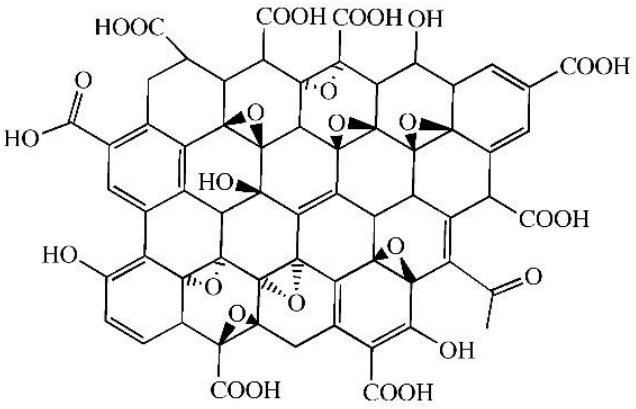

Figure 1.2 Layer of graphite after oxidation containing functional groups.

The interlayer distance of graphite is 0.34 nm and after oxidation the interlayer distance is 0.65 nm, consequently decreasing the energy required to separate the oxidized graphene layers with respect to pristine graphite. The hydrophilic nature of oxidized graphite will also permit water to adsorb into the lamellar structure, further increasing the interlayer distance to 1.15 nm [26, 27], then with the oxidation method can be obtained the novel material.

1.3 Oxidation methods

We report in chronological order four different recipes for preparation of graphite oxide reported in the literature, three older methods and one the most recent method after graphene.

- Brodie Method
- Staudenmaier Method
- Hummers Method
- Tour Method

1.3.1 Brodie Method

Graphite oxide was reported more than one and half centuries ago by B.C. Brodie, a British chemist, who prepared the first batch of graphite oxide when he was investigating the chemistry of graphite in 1859. Brodie's method consists in the addition of potassium chlorate ($KClO_3$) into slurry of graphite in fuming nitric acid (HNO_3) at 60 °C for three to four days. He found that after this treatment the product had an augmented global mass. He washed the batch free from the salts produced in the reaction, dried it at 100 °C and again put it under oxidation, and finally it resulted in a substance with a "light yellow color" which would not change with any additional oxidation treatment. [21] He emphasized that *the product could not be produced by one prolonged treatment*, and one had to promote the oxidation process with the restoration of the original conditions each time. According to his elemental analysis, the product showed that it was composed of

carbon, hydrogen, and oxygen, (C:H:O; 61.04:1.85:37.11) with a molecular formula for the final product $C_{2.19}H_{0.80}O_{1.00}$. After heating to a temperature of 220 °C, the chemical composition of this material changed to $C_{5.51}H_{0.48}O_{1.00}$, coupled with a loss of carbonic acid and carbonic oxide. Weak acidity and mild dispersibility in basic solution was observed, however, the reflective goniometry characterization failed due to the small size, limited thickness and imperfect structure. He also reacted the final product with "protochloride of copper and protochloride of tin" to get GO salts, and followed up with detailed analysis in composition and thermal decomposition. Nonetheless, his observations and conclusions were limited by the theories and characterization techniques. Brodie found the material to be dispersible in pure or basic water, but not in acidic media, which prompted him to term the material ''graphic acid.'' [1, 21, 28].

1.3.2 Staudenmaier Method

In 1898, some years after the report of Brodie, L. Staudenmaier improved the Brodie's method adding concentrated sulfuric acid (H_2SO_4) to increase the acidity of the mixture, and multiple aliquots of potassium chlorate solution ($KClO_3$) into the reaction mixture over the course of reaction [29]. This slight change in the procedure lead to a highly oxidized product (its composition is the same as Brodie's final product) in a single reaction container. However, the method of Staudenmaier was both time expensive and hazardous: the addition of potassium chlorate typically lasted over a week, and the chlorine dioxide evolved needed to be removed by an inert gas, while explosion was a constant hazard [1, 24].

1.3.3 Hummers Method

Almost 60 years after Staudenmaier, the chemists Hummers and Offeman in the Mellon Institute of Industrial Research developed an alternative oxidation to obtain graphite oxide, by reacting graphite with a mixture of potassium permanganate ($KMnO_4$) and sulfuric acid concentrated [22]. The procedure of Hummers to prepare graphite oxide

was by mixing ultrapure graphite powder and sodium nitrate ($NaNO_3$) in H_2SO_4. Then $KMnO_4$ was added to catalyze the reaction and finally a brownish grey gel was obtained. After water dilution and application of hydrogen peroxide (H_2O_2) treatment, a yellow-brown graphite oxide residue was obtained.

Table 1.1 Methods of oxidation of graphite in 100 years of evolution. The Hummers-Offeman method was the most successful oxidation.

GRAPHITE OXIDE EVOLUTION			
YEAR	**AUTHOR**	**TYPE OF GRAPHITE**	**REAGENTS NAME**
1859	B. C. Brodie	Flakes	$KClO_3$
			HNO_3
1898	L. Staudenmaier	Flakes	$KClO_3$
			«fuming» HNO_3
			H_2SO_4
1957	Hummers-Offeman	Powdered flake	**$NaNO_3$**
			H_2SO_4
			$KMnO_4$
			H_2O_2

In Table 1.1 can see that the Brodie and Staudenmaier methods generate ClO_2 gas, which must be moved with caution due to its high toxicity and tendency to decompose in air to produce explosions. Fortunately, this disadvantage was eliminated by the Hummers method, which has a relatively shorter reaction time and hazardous ClO_2 is absent. In the last years, the Hummers method has been widely used, but some modification has been introduced to improve the receipt and reduce toxic gases produced [24, 30, 31]. It should be noted that all three methods involve the generation of toxic gases (NO_2, N_2O_4, and/or ClO_2).

Only in 1999 Kovtyukhova introduced a pretreatment of graphite with an mixture of concentrated H_2SO_4, $K_2S_2O_8$, and P_2O_5 for several hours [32]. The pretreated mixture was diluted, filtered, washed and dried like Hummers oxidation.

Other reported modifications also include the increase of the potassium permanganate amount and elimination of sodium nitrate [1, 27, 28, 30, 33–35].

1.3.4 Tour Method

A new recipe was introduced in 2010 by Professor Tour's group in Rice University [23], adding phosphoric acid (H_3PO_4), increasing the amount of potassium permanganate, and also avoiding sodium nitrate. Figure 1.3 shows the schema presented by Marcano et al. about procedure and final products of three method for oxidation of graphite. Tour and coworkers reported a GO product with higher degree of oxidation by reacting graphite with $KMnO_4$ in a (9:1) mixture of H_2SO_4:H_3PO_4. The biggest advantage of this procedure is the absence of $NaNO_3$, consequently no generation of toxic gases such as NO_2, N_2O_4 or ClO_2 in the reaction, thus making it more eco-friendly. Furthermore, phosphoric acid is believed to offer more intact graphitic basal planes and the final yield is much higher than Hummers method.

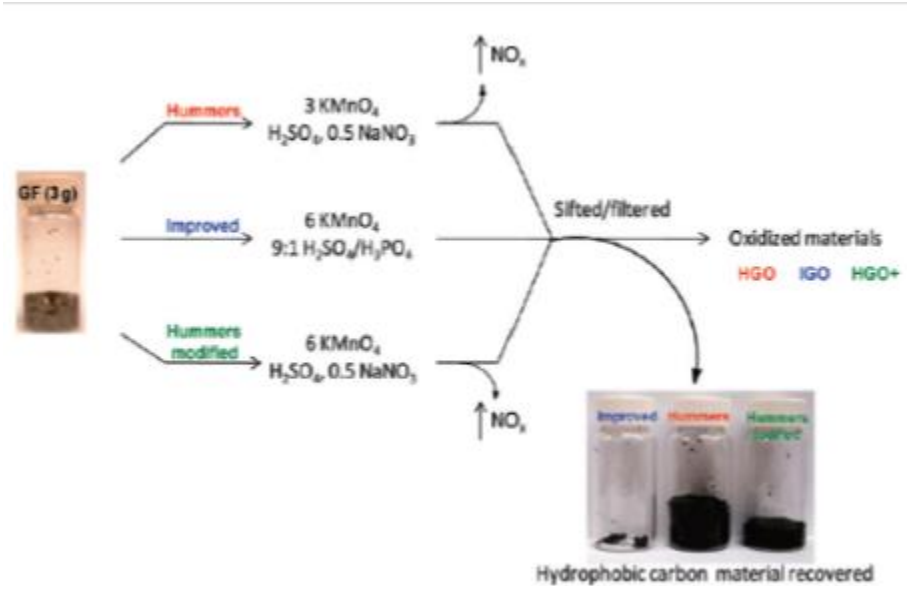

Figure 1.3 Schema of three procedure to oxidizing graphite, evaluation of reagents used and the final product amount. [23]

1.4 Exfoliation: from Graphite Oxide to Sonicated Graphite Oxide

During the oxidation of graphite, the resulting material features disordered graphitic stacking with the *d*-spacing increased from 3.4 Å to around 7.0 Å, which significantly facilitates exfoliation. Mechanical exfoliation after oxidizing is the way to convert graphite oxide to graphene oxide in the liquid media. The more widely used solvent is water. Graphite oxide can be exfoliated in water by sonication, due to the presence of polar functional groups and the increased d-spacing of the material, to obtain flakes of graphene oxide as shown in Figure 1.4 [33, 35, 36]. Sonication and mechanical stirring can be combined together to exfoliate graphite oxide with a better efficiency than using any individual method [16, 30, 35, 37].

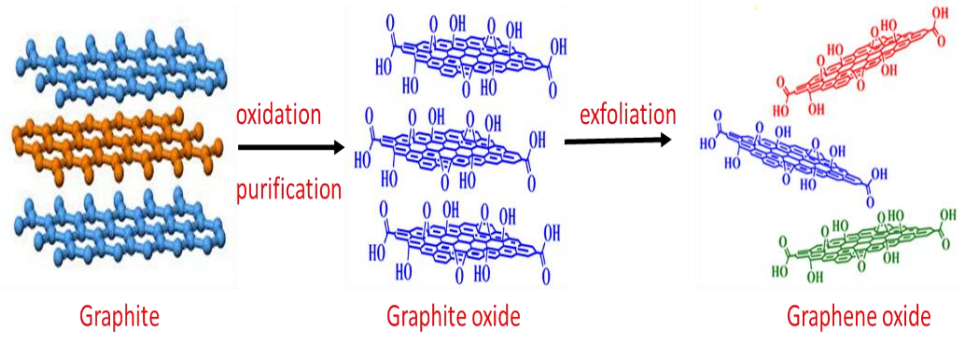

Figure 1.4 Schema of procedure used to obtain graphene oxide from graphite by oxidation purification and exfoliation process.

The graphene oxide structure is complicated and dependent on many parameters in the process under which it is made. Figure 1.5 shows the structures based on different characterizations studied mainly by SSNMR (Solid State ^{13}C Nuclear Magnetic Resonance) and DRIFT (Diffuse Reflectance Infrared Fourier Transform) spectroscopy. Anton Lerf and Jacek Klinowski [25] have published several papers on the

structure and hydration behavior of GO, and these are the most widely cited in the literature about GO.

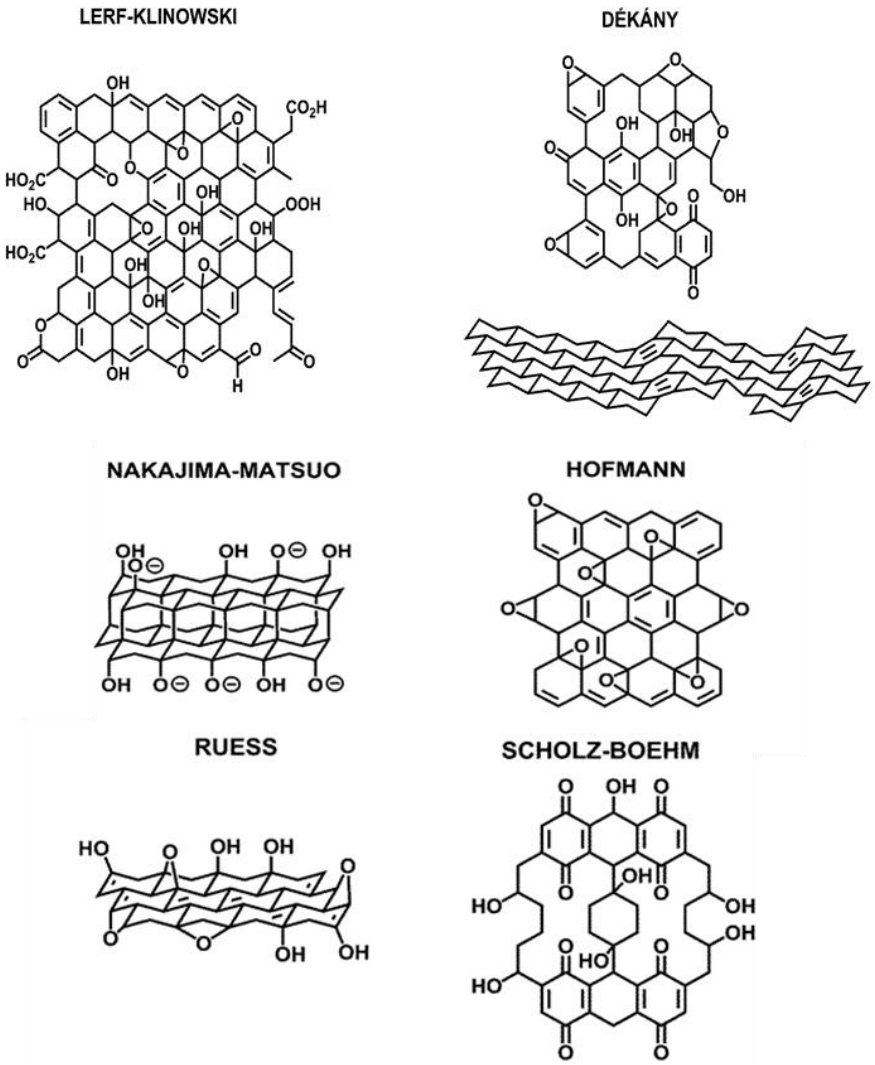

Figure 1.5 Sketching models of GO. Six different structure models proposed for GO suggested by groups since 1939 (Hofmann) until the most recent models of Lerf.

In base to the above methods, we conducted experimental synthesis to obtain Sonicated Graphite Oxide (sGO) material by chemical approach. In the next items are present the synthesis and characterization of GO.

1.5 Experimental Synthesis

1.5.1 Method

We present the experimental procedure used to obtain Graphite Oxide by chemical treatment of graphite. Graphite is naturally abundant and relatively easy to obtain as a source material in graphene production routes. It reacts with a range of chemical compounds to form both covalent and ionic graphite intercalated compound (GICs). The intercalant compounds can be categorized as electron acceptor or donor species. Sulfuric acid, nitric acid and phosphoric acid are some examples of electron acceptors.

The experimental approach to produce sGO with structural and morphological characterizations are detailed in the next sections.

1.5.2 Materials and reagents

Natural graphite flakes were obtained from Pingdu Huadong Graphite Co., Ltd (+50 mesh, 4.69% ash content).

All reagents were purchased from Sigma Aldrich:

- Potassium Permanganate ($KMnO_4$); CAS Number: 7722-64-7
- Phosphoric acid (H_3PO_4) (85 w %) CAS Number: 7664-38-2
- Sulfuric acid (H_2SO_4) (95-98 w %); CAS Number: 7664-93-9
- Hydrogen peroxide (H_2O_2) (30 w %); CAS Number: 7722-84-1
- Diethyl Ether >99%; CAS Number: 60-29-7
- Ethanol (95 w %); CAS Number: 64-17-5
- Distilled water

1.5.3 Synthesis of Graphene Oxide

Graphite oxide was obtained using Tour method [23] with modifications on the purification process. The detailed experimental procedures for the preparation of graphene oxide is the following:

6 g of $KMnO_4$ and 1 g of graphite were placed in a vessel, then a solution (9:1) of H_2SO_4:H_3PO_4 was added slowly under magnetic agitation, producing a slight exothermic reaction and ensuring that the temperature does not increase by more than 60°C with an ice bath. The mixture was stirred for 12 h at 50 °C, and was then slowly cooled down at room temperature (RT). Change during the reaction can be visible by the naked eye or be measured with an instrument. The reaction mixture turned from a brown color to a grey color. At the same time, the viscosity of the solution increased, and the power of stirring had to be increased. Afterwards, a solution (133:1) of ice and H_2O_2 was slowly added controlling the temperature under 30°C.

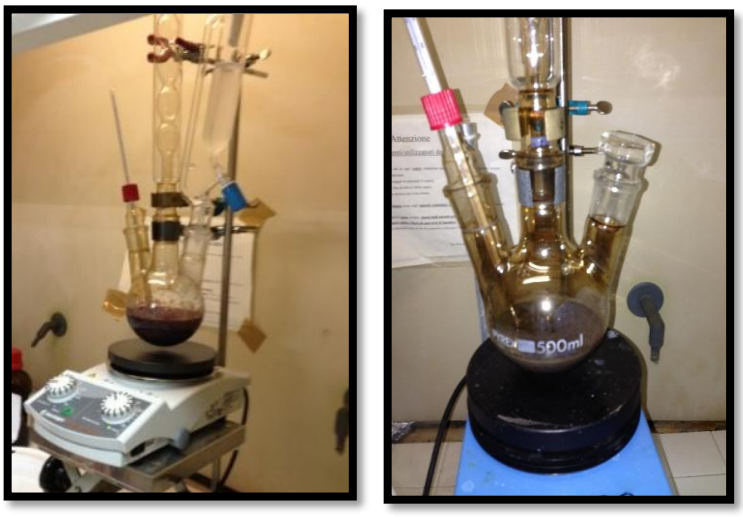

Figure 1.6 Pictures of the oxidation of graphite by chemical process. Left mixture of reagents whit graphite and addition of peroxide water and on the right mixture after heating at 50°C.

After the oxidation of graphite, a mixture of reacted and unreacted graphite additionally contain ions produced from the potassium permanganate treatment, therefore a purification process is necessary in order to analyze the results of oxidation. For the purification process, graphite oxide first was diluted with distilled water and a buffer 3 t 5. Some hours later, the mixture precipitated and the liquid supernatant was decanted. The graphite oxide deposit was collected by centrifugation at 4000 rpm for about 10 min and the supernatant containing unwanted material such as ions and acidic solution was withdrawn. The pellet was then dissolved in distilled water and was thus washed in many steps (Figure 1.7). This solution was subjected to alternate washing and centrifugation cycles with distilled water and ethanol.

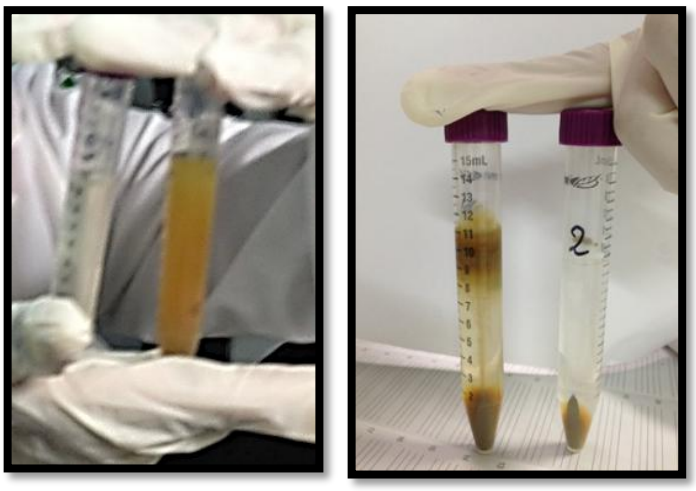

Figure 1.7 Purification process. The mixture was subjected to centrifugation to separate the supernatant solution containing unwanted material of graphite oxide

The first solvent used for washing process was distilled water followed by another ethanol step. Then this washing finished with a water washing step. This process diminished the acidity and some ions formed during the reaction. We used only 2 substances (water and ethanol) to purify the graphite oxide, while the Tour method and others procedures in literature have also reported the use of chloridic acid in the washing process. [23, 24]

The material resulting after purification was exfoliated. This step was performed by exposure to 135 min of sonication, in three cycles of 45 min, using an Ultrasonic processor (UP100H-Hielscher) to separate the layers of graphite containing functional groups, obtaining a colloidal homogeneous solution of sonicated graphite oxide as shown in Figure 1.8 (left). The final solutions were collected in the vessel and dried at RT as shown in Figure 1.8 (right).

a b

Figure 1.8 Pictures of final steps to obtain graphene oxide: (a) sonication process of the mixturel after oxidation and (b) dry graphite oxide after exfoliation (eGO).

1.6 Results and discussions

The sGO samples obtained were studied from a morphological and a structural point of view. Raman spectra were recorded with a Horiba-Jobin-Ivon Labram Raman spectrometer with He-Ne laser (632.8 nm) as excitation source and by a Renishaw Spectrometer using a 100x objective with an incident red laser. UV–visible spectra were obtained by the use of a UV-160A Shimadzu spectrophotometer. Scanning electron micrographs were obtained by a field-emission scanning electron microscope (FEI Quanta FEG 400 F7) (SEM) equipped with analytical system. Transmission electron micrographs (TEM) were performed in a JEOL Jem-2100 microscope. Fourier-transform infrared

spectroscopy-attenuated total reflectance (FTIR-ATR) spectra were recorded on a Fourier transform infrared spectrometer (Perkin Elmer Spectrum 100).

SPECTROSCOPY STUDIES

1.6.1 Raman Spectroscopy

In literature Raman spectra of natural graphite exhibit a relatively simple structure characterized by two principle bands designated as the G and 2D bands. While Raman spectra obtained on graphite oxide evidence the two principal bands (D and G). The G band is an in-plane vibrational mode involving the sp^2 hybridized carbon atoms [38, 39], and the D band is known as the disorder band or the defect band and it is due to a ring breathing mode from sp^2 carbon rings [40, 41].

In Figure 1.9(a) display the spectra of graphite and sGO. Graphite spectrum exhibits a relatively simple structure characterized by two principal bands designated as the G and 2D bands, located at 1575 and 2714 cm^{-1} respectively. In the sGO spectrum, the D band appear, which is activated once the defects are introduced into sp^2 hybridized carbon network. There are two strong active Raman peaks in sGO located at 1332 and 1585 cm^{-1} corresponding to D and G bands, which confirm that the lattice is distorted due to chemical treatment. The second order of D, called 2D peak, consists in a wide weak bump extended 2500 to 3055 cm^{-1}, and originates from a phonon double resonance in the Raman process [38].

Lorentzian curve fitting of graphite and sGO spectra performed in the range after 2500 cm^{-1} as seen in Figure 1.9(b), it evidences that graphite 2D peak is fitted with 2 curves and in 2D peak of GO the fit is with only one curve. The D + G band can also be seen and evidences a combination band which reflects the concentration of defects.

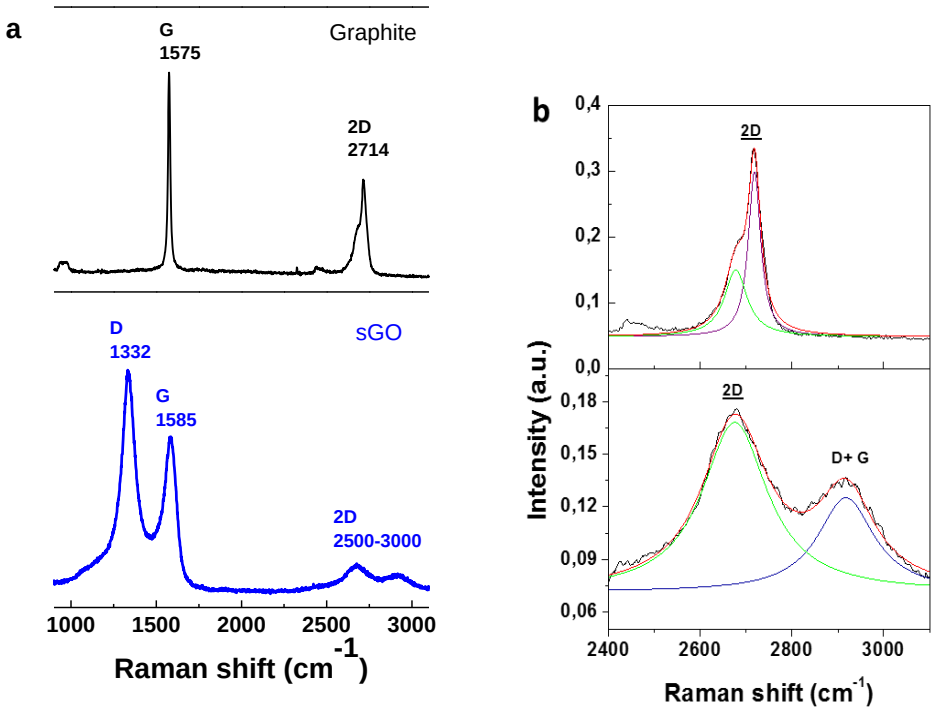

Figure 1.9 (a) Raman spectra of graphite and sonicated graphite oxide obtained with a 633 nm laser in total region. (b) The enlarged region of 2400–3100cm^{-1}, two deconvoluted Raman peaks.

Raman spectra analysis in range from 1000 to 1800 (Figure 1.10), reveals decrease of intensity in G peak and appear D band. Intensity of D band is significant in all spectra, this band is typically very weak in graphite and is typically weak in high quality graphene [40]. The intensity of the D band is directly proportional to the level of defects in the sample. The intensity ratio of spectrum sGO I_G/ I_D is 0,72 which corresponds to a higher level of oxidation [39, 42]. Can see the fit with four individual Raman bands in D and G bands merged together. It is worth noting that, for the highly destroyed sp^2-structure, only D (orange), G (blue) and D□ (green) bands are not satisfactory to fit all the Raman signals; consequently, additional bands between D and G bands (red) are considered for assisting the fitting result.

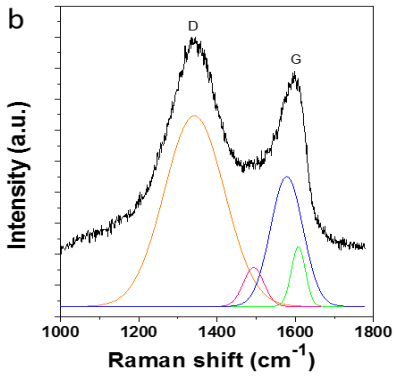

Figure 1.10 Fitting of D and G band of Raman spectrum of sGO.

1.6.2 FTIR-ATR Spectroscopy

FTIR-ATR spectra were measured in the wavelength range from 6500 to 4000 cm^{-1}, as shown in Figure 1.11 to investigate the structure and functional groups of the our material. The sGO sheets showed apparent adsorption bands for different functional groups such as: hydroxyl in the broad band from 2800 to 3600 cm^{-1} that is characteristic of the stretching modes of structural OH bonds, carboxyl C=O at 1724 cm^{-1}

1628 cm^{-1} 1250 cm^{-1} for epoxy group C–O, while the peaks at 986 and 1045 cm^{-1} are due respectively to the stretching mode of C-H and C-O alkoxy groups. Oxygen-containing functional groups in FTIR spectra such as C=O and C–O, confirmed that the graphite was oxidized to obtain sGO [15, 43].

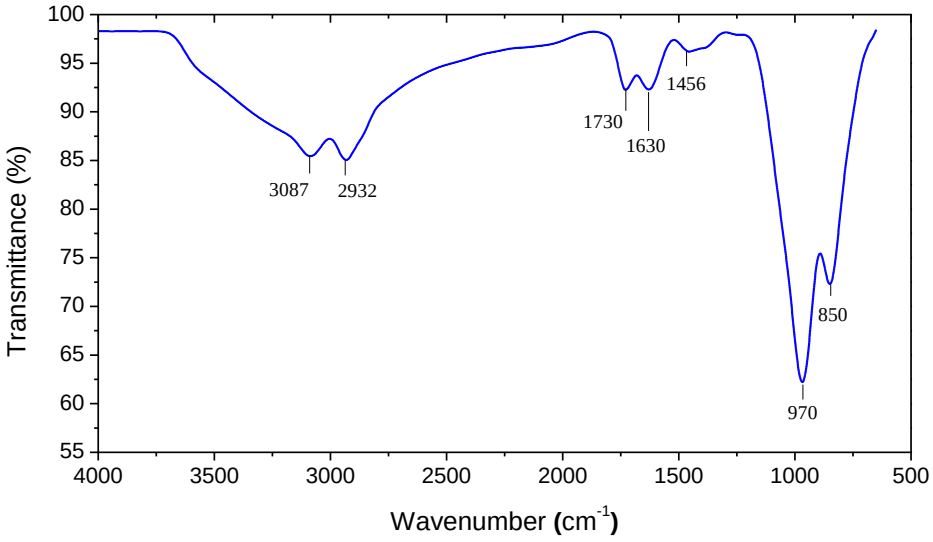

Figure 1.11 FTIR-ATR spectrum recorded of flakes of sGO.

The presence of C=C groups shows that the main structure of the graphite layer was still reserved. The peak from epoxy groups in sGO becomes strong after purification with H_2O which can decompose the epoxy (-O-) groups into hydroxyl (-OH) groups, while the peak from hydroxyl groups grows bigger, revealing that more hydroxyl groups were produced, that can be seen in Figure 1.11.

1.6.3 UV-Visible Spectroscopy

UV-Vis spectra were obtained on aqueous GO dispersions at 0.1 mg/mL, obtained by mixing dry samples of sGO with distilled water (picture inset in Figure 1.12). The spectrum in Figure 1.12 shows the characteristic structure to identify sGO, the peak at 223 nm, corresponding to a π-π* plasmon peak, and to C=C bonds. Another peak is a shoulder at ~260 nm, corresponding to an n-π* plasmon peak, which corresponds to C=O bonds in the domain of carbonyl groups, reported using Tour method [23, 44].

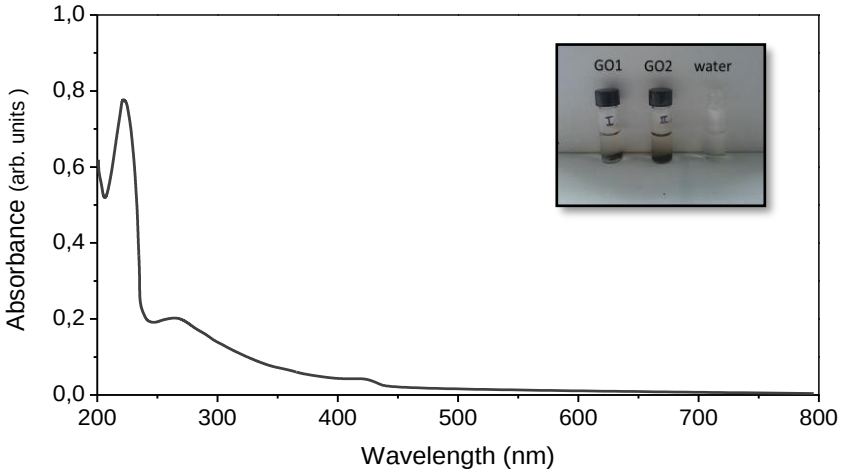

Figure 1.12 UV–Vis spectrum of a 0.1 mg mL^{-1} sGO aqueous dispersion, inset is a photograph of aqueous sGO in water.

1.6.4 XPS Characterization

In advance from UV-vis spectroscopic studies, it was inferred that the optical absorption of sGO is dominated by the π-π* plasmon peak near 230 nm. The π-π* plasmon peak depends on two kinds of conjugative effect, one is related sp^2 bands, and other arises from concerning C=C, C=O and C–O bonds analyzed by XPS spectroscopy [10, 43, 45].

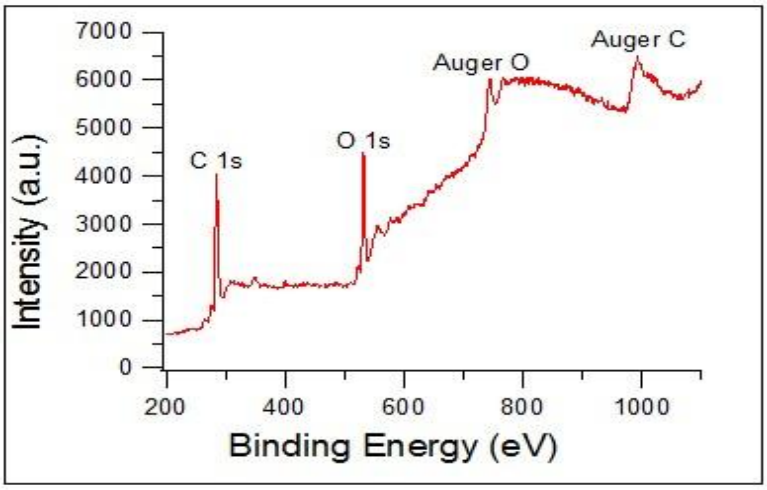

Figure 1.13 XPS spectrum of sGO performed in Ultra High Vacuum Chamber with emission of photons from a magnesium slab, expanded energy range.

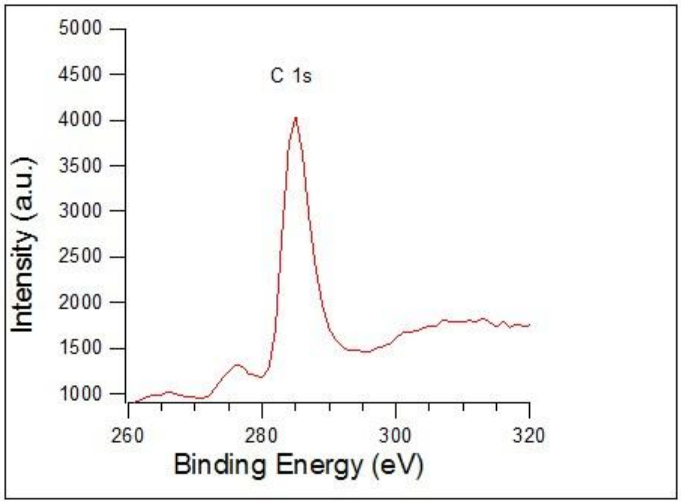

Figure 1.14 C1s XPS spectrum of sGO.

The XPS spectrum of sGO in the 200 - 1100 eV range is shown in Figure 1.13, indicating the presence of photoemission carbon (C1s) and oxygen (O1s) peaks, together with the corresponding Auger peaks. The shape of the C1s peak is shown in detail in Fig. 1.14. The intensity of the C1s and O1s peaks, together with the sensitivity factors for C and O, allowed us to calculate the atomic concentrations of C and O through the formula:

$$Cx = (Ix/Sx)/ \sum (Ix_i/Sx_i),$$

where, Cx is the concentration of element x, Ix and Sx are respectively the intensity of the XPS peak of element x and its sensitivity factor.

Using the intensities measured in the spectrum in Fig. 1.13, we calculate Cc=70% and Co=30%. O atoms of course are contained in the functional groups bonded to the two-dimensional network of carbon atoms, as a consequence of the oxidation process.

MICROSCOPY STUDIES

1.6.5 SEM Characterization

The SEM images in Figure 1.15 show the morphology of the natural graphite [2, 46] we used as a starting material. The mean diameter of the graphite flakes was measured in a range 200 - 500 μm.

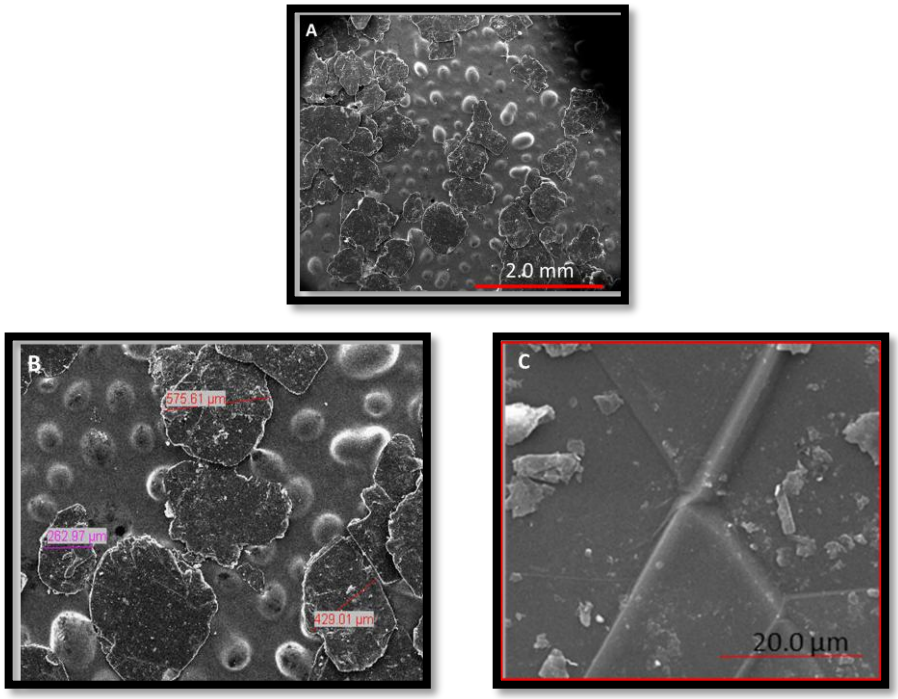

Figure 1.15 SEM images of graphite purchase of Pingdu Huadong Graphite Co., Ltd. (A) Flakes of graphite, (B) measures of some flakes and (C) Hexagonal geometry.

Several samples were taken during procedure to obtain sGO, to study the morphological influence of the processes used. The SEM images of sGO evidence that the surface of graphite was dramatically modified after the chemical treatment (Figure 1.16), showing homogenous aggregates in all images. The aggregates are made of particles with 100 nm, much smaller with respect to the pristine graphite flakes [1, 18, 28, 47].

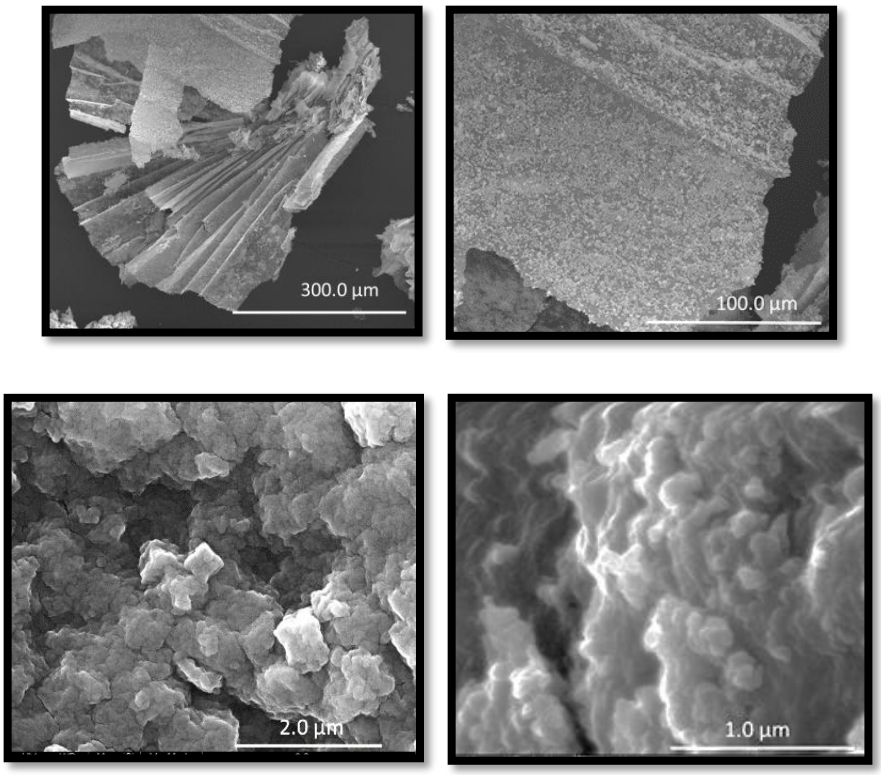

Figure 1.16 SEM images of sGO samples at different magnifications to know the morphology of our material.

We recorded the elemental composition of sGO by Energy Dispersive X-ray Analyzer (EDX). EDX analyses were conducted on several samples before and after the washing process and after the exfoliation process. The results in terms of elemental compositions are shown in Table 1.2. The EDX spectra in Figure 1.17 show two large peaks, due to carbon and oxygen, and weak peaks related to species coming from the reagents used in the oxidizing process. The intensity of the peaks is influenced by the purification of the material to remove ions or acidic. It is possible to note that Mn and P ion peaks diminish in intensity and the C peak increases as a consequence of purification.

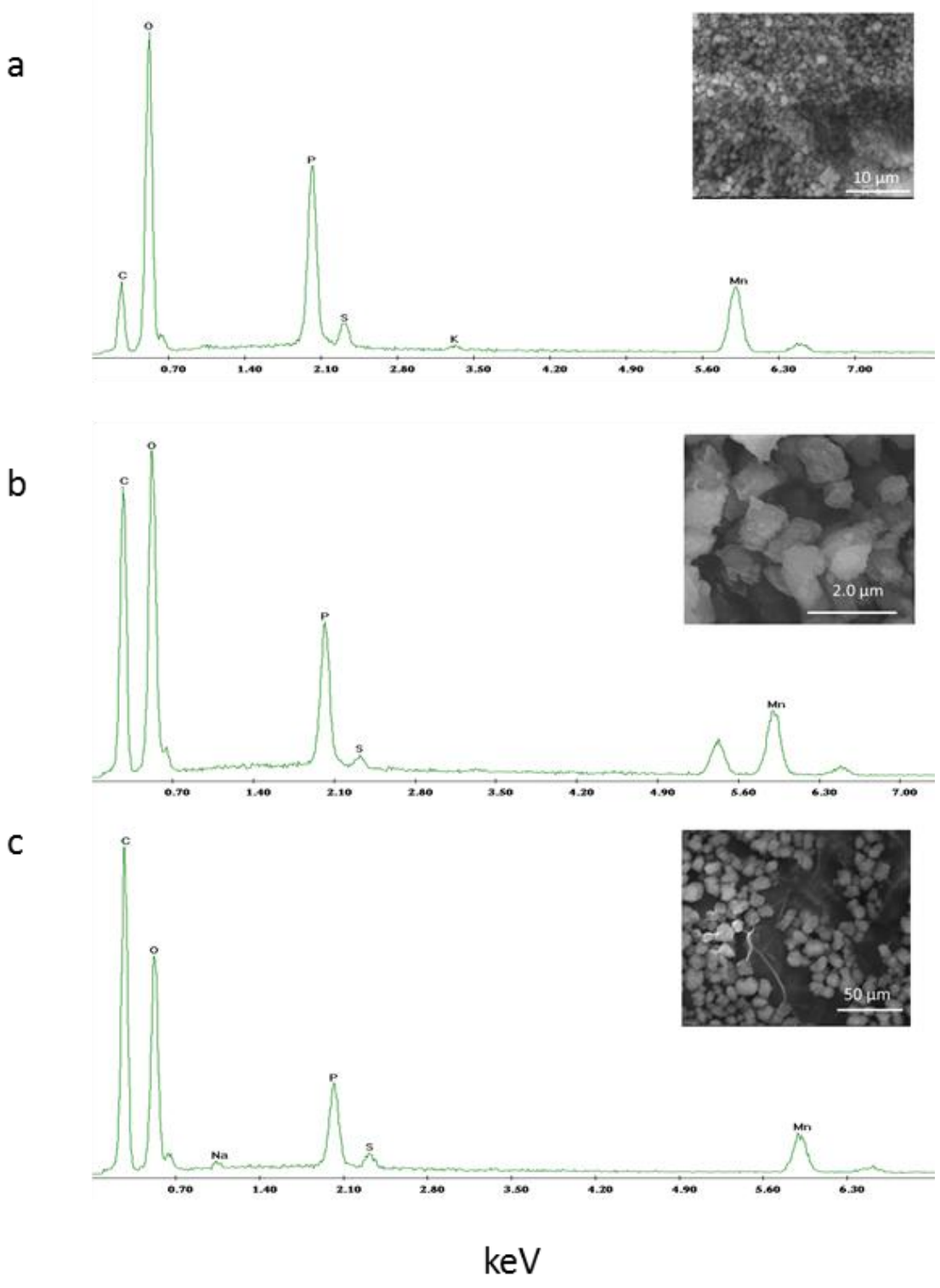

Figure 1.17 EDX spectra performed on the surface with respective SEM images. (a) Graphite oxide, (b) GO after purification process, sonicated one time and (c) sGO.

Table 1.2 The elemental compositions of the samples were identified by energy dispersive X-ray (EDX) analysis.

	Elements (weight %)						
SAMPLES	**C**	**Mn**	**O**	**P**	**S**	**others**	**Totale**
Graphite oxide	28,84	14,46	43,42	11,13	1,79	0,36	100,00
	25,67	13,35	49,74	9,49	1,44	0,30	99,99
Washed and Sonicated Graphite Oxide	66,12	3,09	27,83	1,79	0,66	0,52	100,01
	85,96	0,33	11,24	0,40	1,10	0,97	100,00
	57,32	6,35	31,49	3,65	0,68	0,50	99,99

1.6.6 TEM Characterization

A thin specimen of sGO was irradiated with an electron beam of uniform current density (80 kV) to record TEM images. These TEM observations show that the particles observed in the SEM images are made of aggregates of particles with smaller diameters (on the order of tens nanometers (Figure 1.18)). Figure 1.19 shows a TEM image of sonicated GO with higher magnification, together with the diffraction pattern, which shows some degree of cristallinity with rotational disorder.

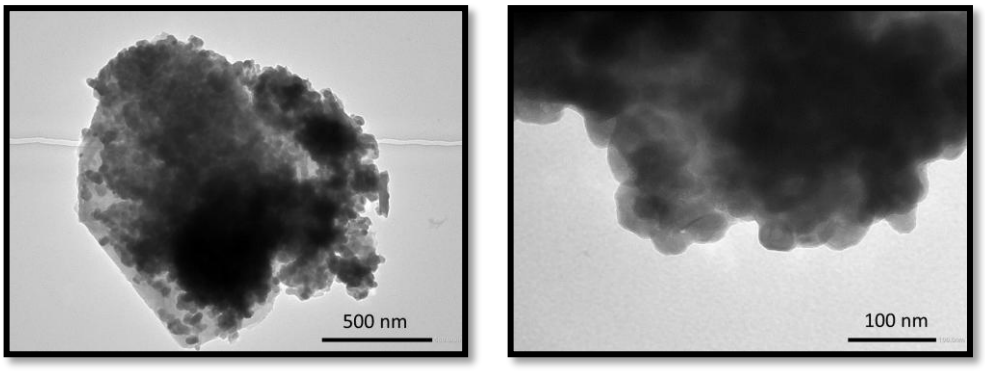

a b

Figure 1.18 (a) TEM image of sGO, (b) high magnification of image that evidence the aggregate of circular particles.

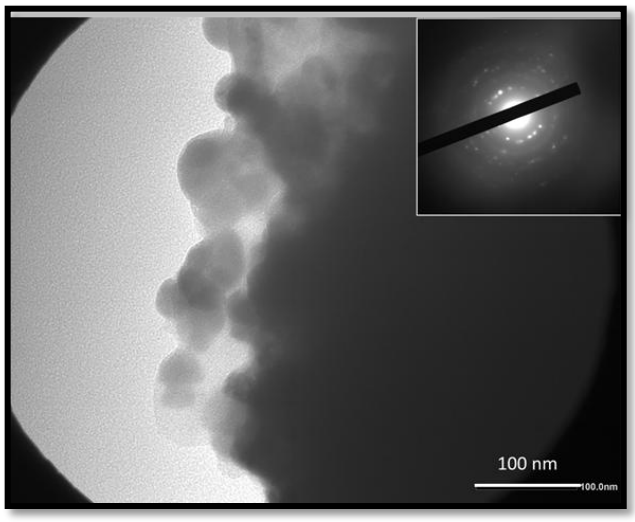

Figure 1.19 (a) TEM image of sonicated graphite oxide and in upper section its diffraction pattern.

1.7 Conclusions:

The Tour's method allowed us to obtain a nanomaterial based on graphite oxide whose properties were studied by spectroscopy and microscopy techniques. The final product obtained with our procedure is not very dangerous because toxic gases are not produced during oxidation, and the purification process is not performed using hydrochloric acid, as in other reported procedures. The sGO can be easily suspended in an aqueous medium because of the presence of functional groups such as hydroxyl, carboxyl, ether and epoxides evidenced by FTIR studies. Surface morphology studies showed a material made of nanoparticles with mean diameter in the range of tens of nanometers. Raman spectroscopy gives evidence of the structural disorder in the two-dimensional network of carbon atoms. To make the process simple and eco-friendly, and to avoid a decrease of the amount of the nanomaterial, we did not use any selection procedure like filtration or centrifugation, and the material was not subjected to reduction processes.

1.8 References

[1] D. R. Dreyer, S. Park, C. W. Bielawski, and R. S. Rouff, R. Soc. Chem. 39, 228 (2010).

[2] A. K. Geim and A. H. MacDonald, Phys. Today 60, 35 (2007).

[3] K. S. Novoselov, A. K. Geim, S. V. Morozov, D. Jiang, Y. Zhang, S. V. Dubonos, Grigorieva I., and A. A. Firsov, Science, 306, 666 (2004).

[4] I. P. Chen, C. Huang, S. Saint Jhou, and Y. Zhang, Sci. Rep. 4, 1 (2014).

[5] C. Lee, X. Wei, J. W. Kysar and J. Hone, Science, 321, 385 (2008).

[6] A. Peigney, C. Laurent, E. Flahaut, R. R. Bacsa and A. Rousset, Carbon, 39, 507 (2001).

[7] A. A. Balandin, S. Ghosh, W. Bao, I. Calizo, D. Teweldebrhan, F. Miao and C. N. Lau, Nano Lett., 8, 902 (2008).

[8] S. Stankovich, D. A. Dikin, G. H. B. Dommett, K. M. Kohlhaas, E. J. Zimney, E. A. Stach, R. D. Piner, S. B. T. Nguyen and R. S. Ruoff, Nature, 442, 282 (2006).

[9] T. Ramanathan, A. A. Abdala, S. Stankovich, D. A. Dikin, M. Herrera-Alonso, R. D. Piner, D. H. Adamson, H. C. Schniepp, X. Chen and R. S. Ruoff, Nat. Nanotechnol., 3, 327 (2008).

[10] B. Ozbas, C. D. O'Neill, R. A. Register, I. A. Aksay, R. K. Prud'homme and D. H. Adamson, J. Polym. Sci., Part B: Polym. Phys., 50, 910 (2012).

[11] B. Seger and P. V. Kamat, J. Phys. Chem. C, 113, 7990 (2009).

[12] Q. Yan, B. Huang, J. Yu, F. Zheng, J. Zang, J. Wu, B. L. Gu, F. Liu and W. Duan, Nano Lett., 7, 1469 (2007).

[13] E. J. Yoo, J. Kim, E. Hosono, H. Zhou, T. Kudo and I. Honma, Nano Lett., 8, 2277 (2008).

[14] M. D. Stoller, S. Park, Y. Zhu, J. An and R. S. Ruoff, Nano Lett., 8, 3498 (2008).

[15] K. P. Loh, Q. Bao, P. K. Ang, and J. Yang, J. Mater. Chem. 20, 2277 (2010).

[16] S. Gilje, S. Han, M. Wang, K. L. Wang, and R. B. Kaner, Nano Lett. 7, 3394 (2007).

[17] Y. Zhu, S. Murali, M. D. Stoller, A. Velamakanni, R. D. Piner, and R. S. Ruoff, Carbon N. Y. 48, 2118 (2010).

[18] W. Gao, 6 (2012).

[19] K. Bramhaiah and N. S. John, Adv. Nat. Sci. Nanosci. Nanotechnol. 3, 45002 (2012).

[20] B. A. Castro and G. S. Sepúlveda, Ingenierías 14, 34 (2011).

[21] B. C. Brodie, *Philos. Trans. R. Soc. London* 149, 249 (1859).

[22] W. S. Hummers and R. E. Offeman, Hummer_1958_oxide graphite by Hummer Method.pdf, (1958).

[23] D. Marcano, D. Kosynkin, J. M. Berlin, A. Sinitskii, Z. Sun, A Slesarev, L. B. Alemany, W. Lu, and J. M. Tour, Acs Nano (2010 Am. Chem. Soc. 4, 4806 (2010).

[24] J. Chen, B. Yao, C. Li, and G. Shi, Carbon N. Y. 64, 225 (2013).

[25] A. Lerf, H. He, M. Forster, and J. Klinowski, Am. Chem. Soc. 102, 4477 (1998).

[26] J. Zhao, W. Ren, and H.-M. Cheng, J. Mater. Chem. 22, 20197 (2012).

[27] Y. Chen, L. Chen, H. Bai, and L. Li, J. Mater. Chem. A 1, 1992 (2013).

[28] S. Park and R. S. Ruoff, Nat. Nanotechnol. 4, 217 (2009).

[29] L. Staudenmaier, D. Substanz, I. Zeit, D. Salze, D. Doppel-, and D. Reaction, Ber. Dtsch. Chem. Ges. 31, 1481 (1898).

[30] J. P. Zhao, S. F. Pei, W. C. Ren, L. B. Gao, and H. M. Cheng, ACS Nano 4, 5245 (2010).

[31] W. Gao, L. B. Alemany, L. Ci, and P. M. Ajayan, Nat. Chem. 1, 403 (2009).

[32] N. I. Kovtyukhova, P. J. Ollivier, B. R. Martin, T. E. Mallouk, S. a. Chizhik, E. V. Buzaneva, and A. D. Gorchinskiy, Chem. Mater. 11, 771 (1999).

[33] W. Lv, D. M. Tang, Y. B. He, C. H. You, Z. Q. Shi, X. C. Chen, C. M. Chen, P. X. Hou, C. Liu, and Q. H. Yang, ACS Nano 3, 3730 (2009).

[34] W. Chen and L. Yan, Nanoscale 2, 559 (2010).

[35] J. Kim, L. J. Cote, F. Kim, W. Yuan, K. Shull, and J. J. Huang, J. Am. Chem. Soc. 132, 8180 (2010).

[36] Y. Zhu, M. D. Stoller, W. Cai, A. Velamakanni, R. D. Piner, D. Chen, and R. S. Ruoff, Am. Chem. Soc. XXX (2010).

[37] M. Cai, D. Thorpe, D. H. Adamson, and H. C. Schniepp, *J. Mater. Chem.* 24992 (2012).

[38] L. Xu and L. Cheng, *J. Nanomater.* 2013, 1 (2013).

[39] A. C. Ferrari, *Solid State Commun.* 143, 47 (2007).

[40] M. Wall, *Thermo Sci.* 5 (2011).

[41] J. H. Warner, F. Schäffel, A. Bachmatiuk, and M. H. Rümmeli, *Characterisation Techniques*, (2013).

[42] C. Casiraghi, A. C. Ferrari, and J. Robertson, *Phys. Rev. B - Condens. Matter Mater. Phys.* 72, 1 (2005).

[43] D. W. Lee, L. De Los Santos V., J. W. Seo, L. L. Felix, a. Bustamante D., J. M. Cole, and C. H. W. Barnes, *J. Phys. Chem. B* 114, 5723 (2010).

[44] D. Coello-Fiallos, C. V. Gómez, G. T. Usca, D. C. Pérez, P. Tavolaro, G. Martino, L. S. Caputi, and A. Tavolaro, *Americ. Inter. Conf. Proc.* 1646, 38 (2015).

[45] J. Song, X. Wang, C.-T. Chang, J. Song, X. Wang, and C.-T. Chang, *J. Nanomater.* 2014, 1 (2014).

[46] A. K. Geim, *Science (80-.).* 324, 1530 (2009).

[47] T. Hartono, S. Wang, Q. Ma, and Z. Zhu, *J. Colloid Interface Sci.* 333, 114 (2009)

CHAPTER 2

Environmental Applications:

Removal of Pollutants from Aqueous solution on Graphite Oxide

2 Removal of Pollutants from Aqueous Solution on Graphite Oxide

MOTIVATION

The intensification of agricultural and industrial activities in developing and developed countries have resulted in a dramatic increase in the number and quantity of contaminants released into the environment. The wastes discharged from the textile, printing and tanning industries contain many dye stuffs, consequently is necessary improve materials, protocols and techniques for the removal of contaminants from wastewater. Among the technologies widely used, adsorption is a fast, inexpensive, and effective method for removal of contaminants.

Adsorption is a process for decontamination where the contaminant (**adsorbate**) is captured by the nanomaterial (**adsorbent**) via physicochemical interactions. A kind of harmful water pollutants are organic dyes, which has been widely used in various industrial fields, such as coating, papermaking and textiles.

Decontamination of water containing dyes is the environmental application focused in this chapter. This application was developed to delineate key adsorption mechanisms and the advantages and disadvantages of using sonicated graphite oxide as adsorbent for decontamination. There are numerous reports in the literature suggesting applications of graphene and graphene oxide.

2.1 Introduction

The pollution due to residual dyes from different industrial sources affects rivers and waterways and has adverse effects on humans, animals and plants [1]. Moreover, under environmental conditions, dyes undergo chemical changes and the resulting products may be more dangerous than the parent molecules. Therefore, the removal of the hazardous dyes from industrial effluents and household wastewater is a challenging topic that has generated a lot of scientific interest in recent years [2]. Most of the dyes are stable with respect to oxidizing agents, bio- and photo-degradation, thus the conventional physico-chemical and biological methods do not give satisfactory results for environmental remediation. For such reasons, the best approach to reduce the concentration of dyes in wastewater is adsorption on the surface of suitable materials [3,4]. The most common adsorbent for the removal of organic contaminants is activated carbon, however the procedure is very expensive, limiting its application [5].

Recently, it has been shown that another carbon-based material can be used as an effective adsorbent of contaminants. Graphene, the two-dimensional honeycomb layer of carbon atoms [6–8], is the basic constituent of all graphitic materials (graphite, fullerenes, carbon nanotubes), and is one of the most exciting new materials since its first isolation by Novoselov et al. in 2004 [9]. The remarkable mechanical, electrical and thermal properties make graphene an ideal candidate to be used in many fields of applied science. Graphene-based materials have been investigated as photocatalytic or sorbent materials to develop next generation decontamination strategies [10–13]. In this respect, particularly important is graphite oxide, obtained by a chemical treatment of graphite [13–15], which presents high water solubility and different functional groups (epoxies, hydroxyls and carboxylic groups) which facilitate the interaction with chemical species solubilized in water [11,16]. Different investigations have been made to test graphite oxide-derived materials as adsorbents of dyes [17–30].

We present a study of adsorption of cresyl violet (CV), methylene Blue (MB) and acridine orange (AO) dyes on sGO. CV, MB and AO are basic dyes which exhibit cationic

properties when dissolved in water and react on their basic sides. MB is normally used for textile dyeing [31], and furthermore for paper and hair colouring. If inhaled, MB may cause tachycardia, cyanosis, convulsions and dyspnea, and it may also cause irritation to the gastrointestinal tract, nausea, diarrhea and vomiting if swallowed [32,33]. MB is also used to stain tissues in biology. AO is a heterocyclic dye used in the printing and leather industries, and also to study DNA interactions with proteins and drugs [34]. CV is a dye used mainly in optical microscopic studies of tissues in medicine and biology [35].

Basché et al. investigated CV adsorption on g/alumina and on silica gel by high-resolution optical techniques, showing that at low coverages CV is predominantly adsorbed monomeric [36]. To our knowledge, this is the first quantitative investigation of the adsorption properties of Cresyl Violet on a solid adsorbent. On the contrary, MB and AO have been different studies [4,11,13,27,28,37–42]. Graphite oxide, obtained by oxidation of graphite without any further exfoliation, exhibited an adsorption capacity of 350 and 248 mg/g for MB and malachite green respectively, much higher than activated carbon, and the adsorption was attributed to electrostatic attraction [43]. A graphene sponge made of graphene oxide was tested as adsorbent for MB, rhodamine B and methyl orange, showing adsorption capacities of 184, 72.5 and 11.5 mg/g respectively, with pseudo-second order kinetics [29]. Lv et al. studied the adsorption of AO on swelling clays [40]. Photocatalytic degradation was applied on AO using semiconductor TiO2 [38]. AO was also recently adsorbed on rye straw, obtaining a maximum adsorption capacity of 208.3 mg/g [37].

2.2 Materials and Method

The adsorbent used in this work was sonicated Graphite Oxide (sGO), the procedure to obtain the adsorbent was detailed in Chapter 1. The dyes were purchased from Sigma Aldrich and used without further modification.

- Methylene blue
- Acridine orange
- Cresyl violet

Analog VORTEX mixed (VWR, 58816-123) was used for shaking.

The stock solutions of MB, CV and AO were prepared in distilled water at concentration of 100 g mL^{-1}. All working solutions were prepared by diluting the stock solution with distilled water to obtain desired concentration (Figure 2.1). These solutions were kept in the dark.

Figure 2.1 Picture of dye solutions prepared in distilled water, cresyl violet (1), acridine orange (2) and methylene blue (3), which were reserved in glass bottles.

We used spectrophotometric quantitative analyses to evaluate the capacity of sGO material to adsorb dyes. Analysis was performed by UV-Visible spectrophotometer UV-160A Shimadzu.

2.3 Adsorption method

Adsorption experiments were carried out at room temperature (RT) using the depletion method in vials containing 1 mg of dry sGO and 2.5 mL of dye solution at 50 mg/L initial concentration. The vials containing the sGO/dye mixtures were placed in Vortex in constant shaking (100 rpm) at room temperature for predefined time intervals. All adsorption experiments were performed in equilibrium conditions. The adsorption capacity was determined by the quantitative analysis of the remaining concentration. Figure 2.2 shows pictures of dye solution during the adsorption process: (a) shows four vials containing sGO/AO mixture for shaking process, while (b) and (c) show cuvettes

with supernatant solution of MB and CV respectively, after different contact times with sGO, which were used for quantitative analysis.

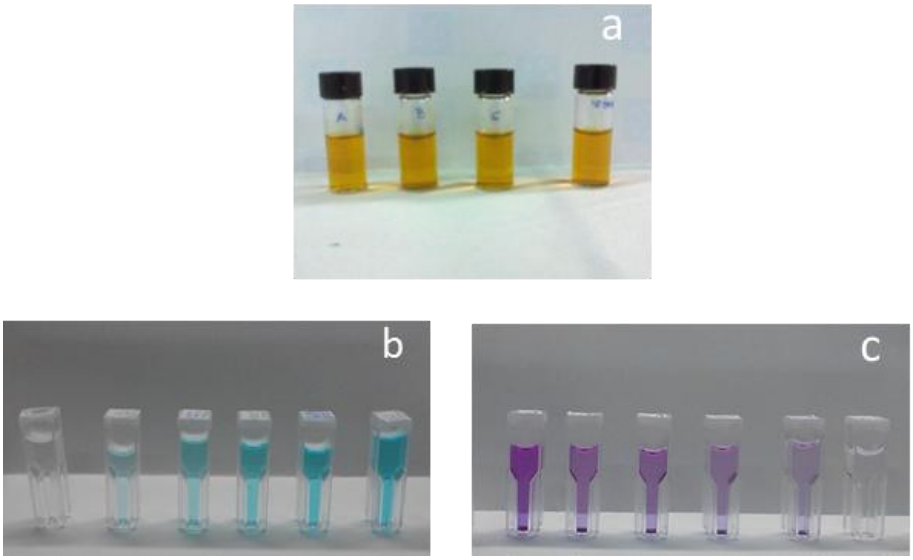

Figure 2.2 Picture of adsorption processes: (a) Vials containing sGO/AO mixture, (b) supernatant solution of MB and (c) supernatant solution of CV.

For the quantitative analysis, a series of dye solutions at determined concentrations were prepared and their UV-Vis absorbance was measured to build the calibration curve using a characteristic maximum wavelength (λ_{max}) for each dye. The wavelengths of maximum adsorption used in this study are 664, 492 and 584 nm for MB, AO and CV respectively. The calibration curve permits to obtain the concentration of the dye after defined time and the amount of adsorption was calculated by equation I:

where,

q_t is the amount of dye adsorbed at time t (mg g^{-1}),

V is the volume of the solution (mL),

m is the mass of the adsorbent (g),

C_0 and C_t are the concentrations of the dye at initial time (t = 0) and at time t,

respectively.

2.3.1 Adsorption Kinetics

The effect of adsorption time on the removal of the three cationic dyes CV, MB and AO at room temperature was studied by following the intensity of the main absorption peak in the UV-Vis spectrum for each dye (Figure 2.3). Figure 2.4 shows the adsorbed quantity as a function of time for the three dyes, with an initial concentration of 50 mg/L in the three cases. The results indicate that adsorption proceeds with different rates for the three dyes: CV reaches the saturation value much more rapidly with respect to MB and AO. The adsorption of MB seems to proceed in two phases: the first phase ends with a plateau which starts at about 10 h, and with increasing time a slow increase of the adsorption quantity leads to another plateau. AO adsorption proceeds so slowly that it is very difficult to determine an equilibrium time in the time range of our experiments.

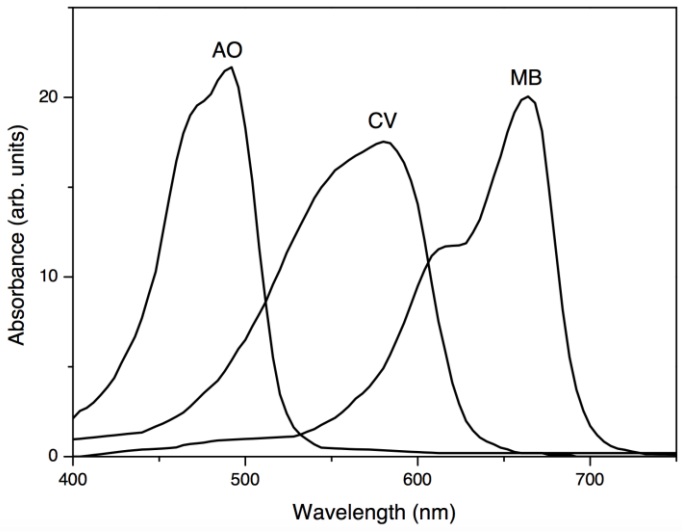

Figure 2.3 Typical absorption peaks of the three dyes in their UV-Vis spectra.

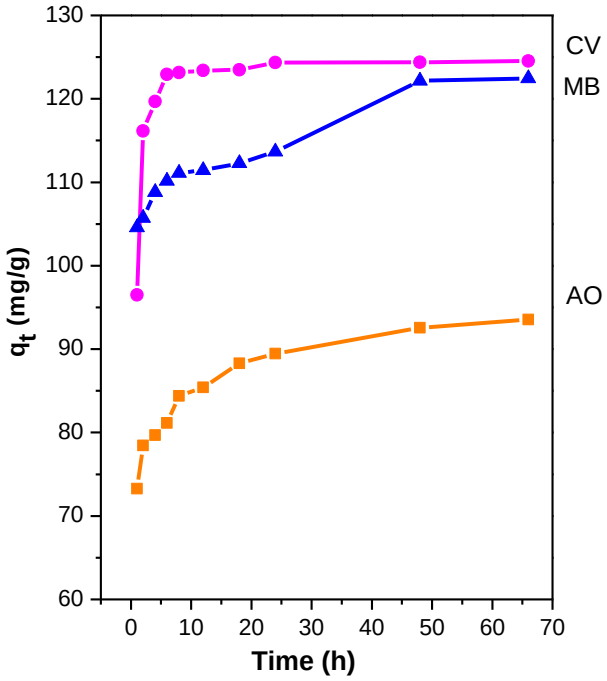

Figure 2.4 Kinetic adsorption of CV, MB and AO on GO adsorbent. Influence of adsorption time from 1 to 66h.

In the attempt to investigate the nature of kinetic processes, the most popular models are the so-called pseudo-first order (or Lagergren) model, and the pseudo-second order model. Both models are based on the assumption that adsorption is driven by the difference between the actual and the equilibrium concentration of adsorbed species on the surface of the adsorbent. We have also considered the Elovich model, which is one of the most used models in case of chemical adsorption on solid surfaces without desorption of products.

2.3.1.1 Elovich Model

The Elovich model, reported by Aharoni and Tompkins in 1970 [44], assumes that the rate of adsorption decreases with the time due to the decreasing number of available adsorption sites, represented with the equation (II)

where,

is the initial adsorption rate (mg g^{-1} h^{-1}) and is the desorption constant (mg g^{-1}).

With the approximation , and by applying the boundary condition at , then equation (II) becomes equation (III):

The two constants can be obtained by the slope and intercept of a straight line plot of vs . However, the correlation coefficient (Table 2.1) demonstrates that our CV adsorption data do not fit with the Elvoich model.

2.3.1.2 Pseudo-first order model

The pseudo-first order or the Lagergren model is one of the most used models to study adsorption in wastewaters, and can be expressed as:

,

where,

($mg\ g^{-1}$) is the quantity of dye adsorbed at equilibrium,

($mg\ g^{-1}$) is the quantity of dye adsorbed at time t,

is the first order rate constant (h^{-1}).

The eventual linearity of the vs. plot would confirm the applicability of the pseudo-first order model. The coefficients of determination are shown in Table 2.1, and show a remarkable difference between the value of CV and those of MB and AO. In fact, CV adsorption seems quite far from the fitting conditions with respect to MB and AO, as it appears evident at the plots in Figure 2.5.

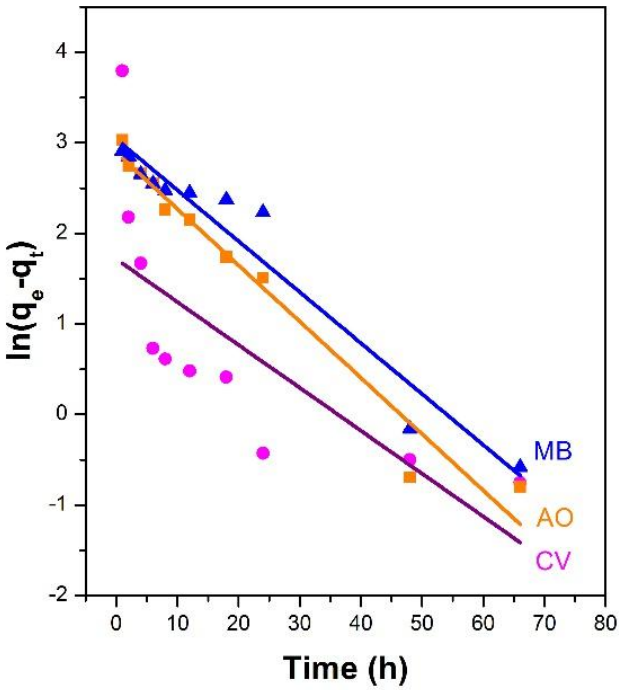

Figure 2.5 Pseudo-first-order models for adsorption of three dyes on sGO. Color line of respective dye.

2.3.1.3 Pseudo-second order model

The integrated linear form of the pseudo-second order model is the following:

— ——— —

where,

and (mg/g) h are the adsorbed amount in equilibrium and in time t

is the rate constant of pseudo-second order (g mg^{-1} h^{-1}).

The model has the advantage that, if the plot of vs. exhibits a linear behaviour, the slope and the intercept allow determination of the adsorption capacity and the rate constant, without the need to measure the equilibrium capacity in separated experiments, which is particularly important in cases of very slow adsorption processes. Figure 2.6 shows the vs. plots for the three dyes investigated, together with best fit linear regressions.

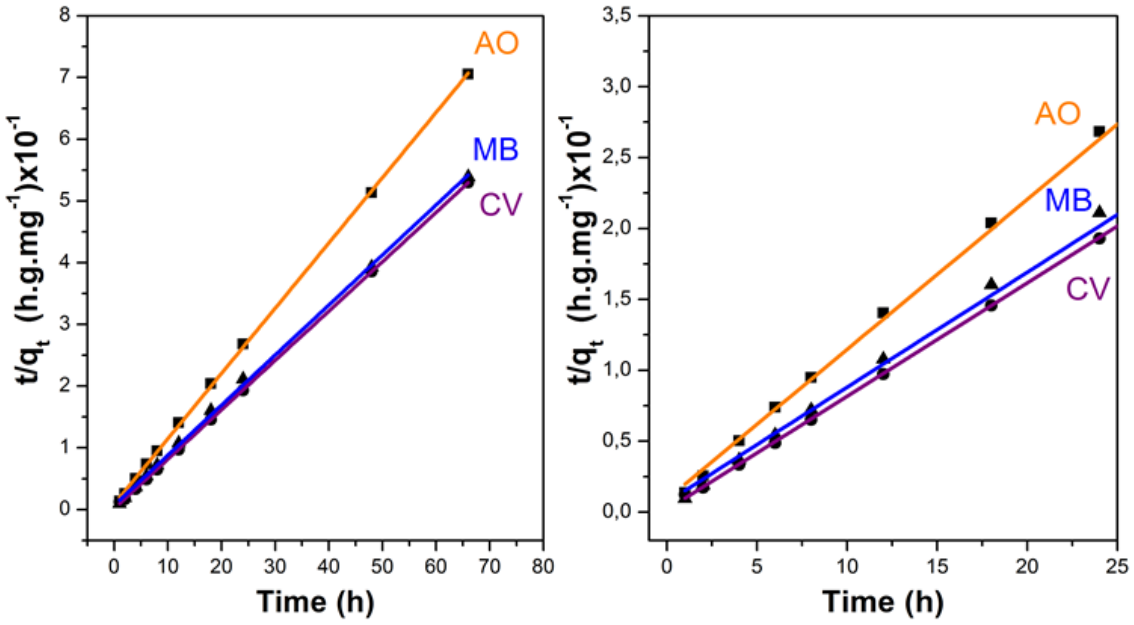

Figure 2.6 (a) Pseudo-second order adsorption kinetics of CV, MB and AO on sGO. In (b) zoom in the time range from 1 to 25 h.

The three coefficients of determination, shown in Table 2.1, seem to demonstrate that the adsorption data of MB, AO and CV on our sonicated graphite oxide fit well with the pseudo-second order kinetic model. The presence of the first plateau in the plot of MB determines a slight deviation from the linear behaviour, but such a deviation does not cause a relevant decrement of the value of R^2 with respect to the values of CV and AO. Table 2.1 also shows the values of the equilibrium adsorption capacity and of the pseudo-second order rate constant. For additional representation we calculated the non-linear fit of experimental data using the parameters obtained by pseudo-second order model (Figure 2.7)

Table 2.1 Correlation coefficients for the three kinetic models tested to CV, MB and AO, together with the values of equilibrium adsorption quantity and rate constant to pseudo-second order model.

Dye	Elvoich	Pseudo-first order	Pseudo-second order		
	R^2	R^2	R^2	q_e	k_2
CV	0.447	0.488	1.000	125.0	0.038
MB	0.883	0.940	0.999	123.3	0.009
AO	0.982	0.960	1.000	94.6	0.012

In literature are presented studies of the impact of several influential parameters such as contact time, initial dye concentrations, using different kinetic models [38,45–47]. The comparison between the results obtained for CV and those obtained for MB and AO presents some interesting points. Ho and McKay systematically examined more than 70 previous investigations regarding adsorption of various types of pollutants (dyes/organics and metal ions) in aqueous solutions.[48] In 43 of these studies, regarding different adsorbent/adsorbate systems, the proposed kinetic mechanism was the pseudo-first order kinetic mechanism. The analysis of the data allowed Ho and McKay to demonstrate that

for 11 of the literature data reported as first order kinetics, the highest correlation coefficients were obtained for the pseudo-second order kinetic model. Rudzinski and Plazinski discussed deeply the applicability of the pseudo-first order model,[49] and called for theoretical studies to understand if the better applicability of the linear regression versus of the pseudo-second order model is due to the adsorption process, or to the mathematical feature of such representation. Moreover, they showed that the pseudo-first order model applies better for the longer adsorption times, not far from equilibrium.

The analysis of adsorption data by pseudo-second order linear regressions has to be taken with caution. As pointed out by Ho et al. [50], Ho [51] and by Rudinsky and Plazinsky [49], transformation of non-linear pseudo-second order kinetic models into one of their possible linear forms, may alter the error structure and may also violate the error variance and normality assumptions of standard fitting methods. The consequence is that high values of the coefficient of determination, obtained from linearized forms of the pseudo-second order equation, may be sometimes misleading. Our results are a clear example of this problem.

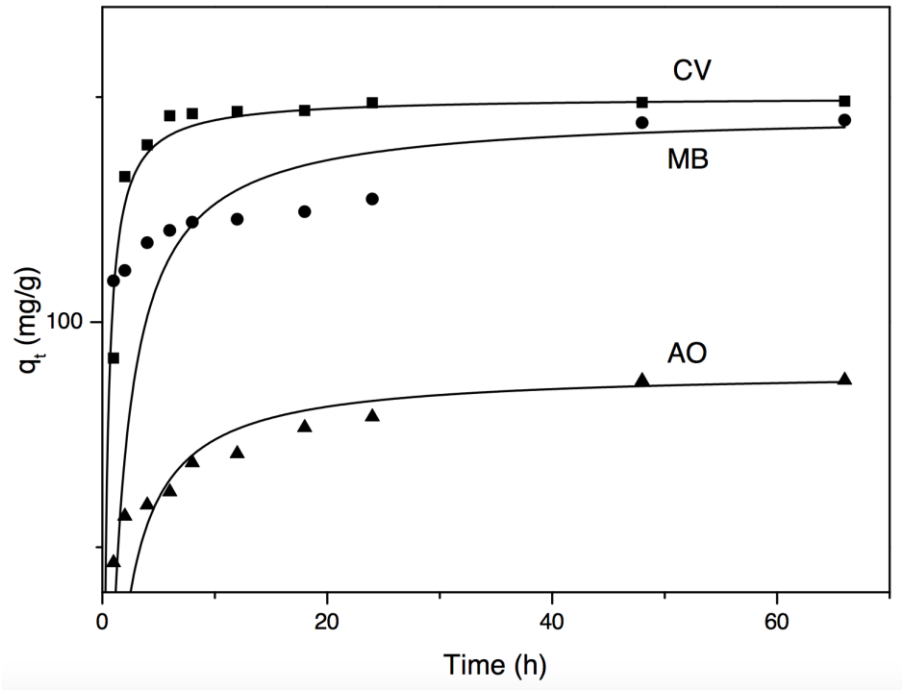

Figure 2.7 Experimental adsorption quantity of the three dyes as a function of time, represent by ■ for CV, ● for MB and ▲ for AO. The full lines represent the non-linear fit by pseudo-second order kinetic model.

From the values of R^2 obtained for CV, MB and AO (Table 2.1), one would expect q_t as a function of time to follow almost perfectly the pseudo-second order kinetics. In fact, when the non-linearized expression for q_t is compared with the experimental points (Figure 2.7), it appears that the correspondence between the model and the experiment is much better for CV than for MB and AO. The applicability of the pseudo-second order model to the adsorption of MB and AO on sGO is then in some extent questionable, while there is an effective correspondence between that model and the experimental adsorption kinetics of CV.

Thus, we can conclude that, based on the assumptions of the pseudo-second order model, the adsorption of CV on sGO is mainly due to chemical adsorption.

2.3.2 Acridine orange studies

Additionally, we performed a study of adsorption of acridine orange dye to analyze parameters that can influence the process, such as: initial concentration (from 20 mg/L to 100 mg/L with an increment of 20 mg/L), contact time (from 10 min to 66 h), temperature (2, 18 and 50 °C) and the adsorbent mass (from 1 to 20 mg). The adsorption capacity for each concentration was determined by the quantitative analysis of the remaining AO concentration, through the analysis of the absorption peak in the UV-Vis spectrum at λ_{max} = 496 nm.

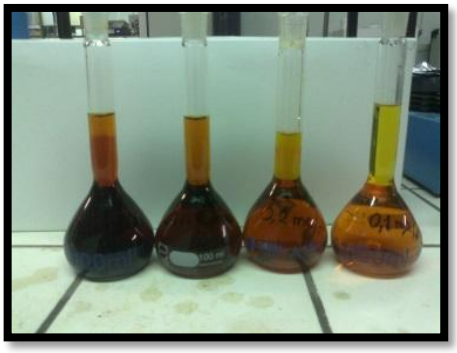

Figure 2.8 Picture of acridine orange dye solution in distilled water at different concentrations.

In the first batch of experiments, we studied the influence of the initial concentration of AO. Adsorption experiments were performed following the depletion method described above at same equilibrium conditions for each one AO concentrations.

In the second batch of experiments, the parameter studied was the GO mass. In a set of vials containing 1, 2, 5, 10, 15 and 20 mg of GO we added 2.5 mL of AO solution at concentration 100 mg/L in each one; the vials were then shaken for 24 h at room temperature.

2.3.2.1 Influence of initial concentration

Figure 2.9 evidences the effect of contact time using five different initial concentrations of AO.

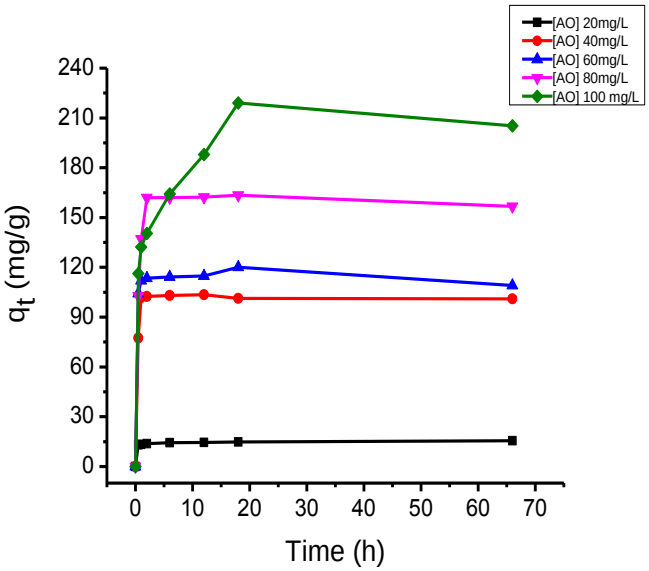

(a)

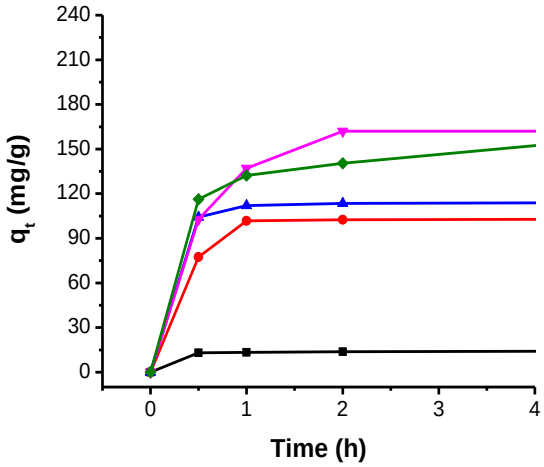

(b)

Figure 2.9 (a) Effect of contact time in the adsorption process for five initial concentration of AO solution on sGO. (b)Zoom of adsorption curve in the range from 1 to 4 h.

The amount of AO adsorbed depends directly of the initial concentration of AO. The adsorption achieves the plateau in 24 h for the highest concentration (100 mg/L) with an amount adsorbed of 219 mg/g, while for other concentrations, under 100 mg/L, the equilibrium is reached 2 h.

Figure 2.10 shows the percentage of dye adsorbed as a function of time. The removal percentage exhibits optimal values between 70 and 95 % for the higher initial concentrations (from 40 to 100 mg/L). Only for the lowest concentration (20 mg/L) the removal percentage is noticeably lower (less 30%) compared to other concentrations.

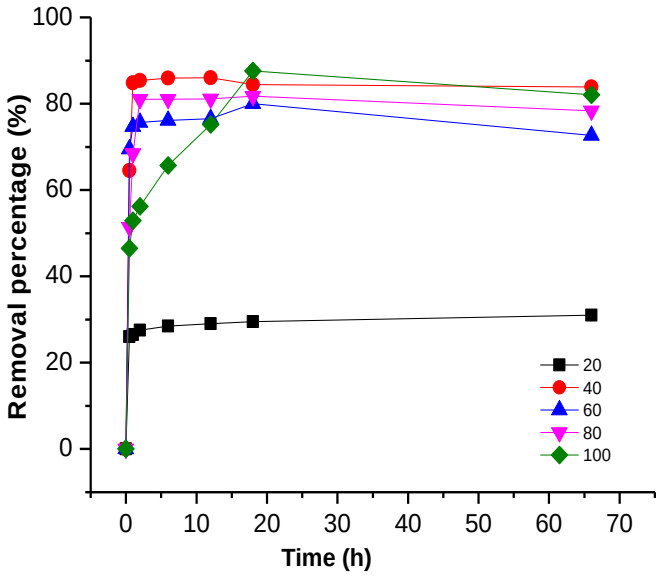

Figure 2.10 Graphic of removal percentage vs. time.

2.3.2.2 Influence of temperature and adsorbent mass

The influence of sGO mass is displayed in Figure 2.11. In the graphical representation of adsorbed quantity *vs* adsorbent mass, q_t exhibits the highest value at 1 mg of sGO, for an initial concentration of 100 mg/L. In fact, the amount of removed AO

remains almost the same with increasing the mass of adsorbent sGO (see Table 2.2), and this results in a much higher adsorbed quantity q_t (defined as the adsorbed quantity per unit mass of the adsorbent) when small amounts of sGO are used. This behavior can be ascribed to a slow mass transfer between adsorbate and adsorbent.

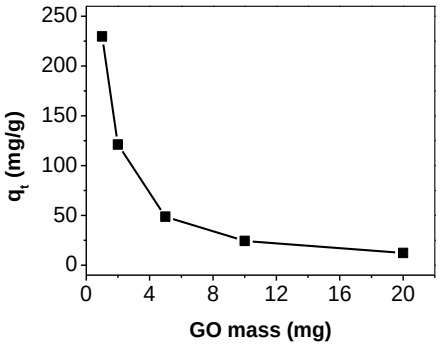

Figure 2.11 Adsorption influences of mass of adsorbent during adsorption process of AO on sGO.

Table 2.2 Calculation of removal percentage using different mass of sGO.

GO mass (mg)	[AO] initial (mg/mL)	AO Volume (mL)	Time (h)	[AO] Final (mg/mL)	AO removal amount (mg)	AO removal Percentage
1	0.1	2.5	24	0.0081	0.2298	91.9
2	0.1	25	24	0.0031	0.2423	96.9
5	0.1	2.5	24	0.0027	0.2433	97.3
10	0.1	2.5	24	0.0026	0.2435	97.4
20	0.1	2.5	24	0.0025	0.2438	97.5

2.3.2.3 FTIR analysis

FTIR spectra were recorded on a Perkin Elmer Spectrum 100 FTIR spectrophotometer using the "Attenuated Total Reflection" (ATR) technique. The spectra were recorded from 4000 to 600 cm^{-1} with baseline correction. Spectra of sGO/AO were recorded to obtain information about the interaction of AO with functional groups of sGO.

The FTIR spectra of GO, AO and AO/GO are plotted in Figure 2.12. In the spectra of GO/AO an increase in the intensity of carboxyl group at 1736 cm^{-1} and of hydroxyl group at 3095 cm^{-1} was observed, and new bands appear around 1630 cm^{-1}, related to –C C– and –C N– stretching modes of AO, and around 1360 cm-1, due to and–C–N–stretching

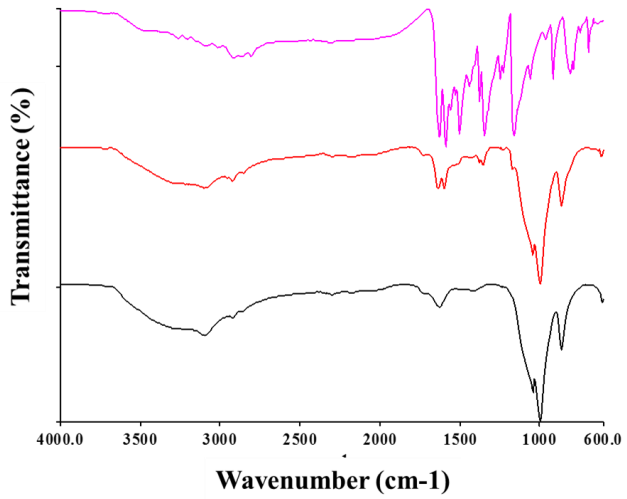

Figure 2.12 Plot of FTIR spectra: AO spectrum in violet line, sGO represented by red line, and the spectrum of conjugate GO/AO after 24 h of contact in black line.

2.4 Conclusions

In summary, we have shown a study of adsorption of the Cresyl Violet dye on a nanomaterial obtained by oxidation of graphite followed by sonication, without any other treatment. We wanted to use the raw sonicated nanomaterial without the application of selection procedures like centrifugation or filtration, to simplify the production procedure and to avoid the inevitable decrease in the available amount of the nanomaterial, in view of possible applications. For comparison, adsorption studies in the same experimental conditions were conducted on two other cationic dyes. Our results show that the adsorption quantity is higher for CV with respect to MB and AO, and also that for CV equilibrium is reached more rapidly with respect to MB and AO. For MB and AO we do not find a very good agreement with the pseudo-second order model. For CV, on the contrary, the data fit

well with the pseudo-second order model, both in the linearized and in non-linearized forms. The results show that sGO can be used for an efficient and rapid removal of Cresyl Violet from aqueous solutions, based on a chemisorption process.

We have also studied in more details the adsorption of AO in sGO, with particular attention to the influence of important parameters like the initial concentration of AO and the amount of adsorbent.

2.5 References

[1] Ratna and B. Padhi, *Int. J. Environ. Sci*. 3, 940 (2012)

[2] A. Ghaly, R. Ananthashankar, M. Alhattab, and V. Ramakrishnan, J. Chem. Eng. Process Technol. 5, 1 (2013)

[3] Y. S. Ho and C. C. Chiang, Adsorption 7, 139 (2001)

[4] A. A. Nazari Moghaddam, G. D. Najafpour, A. A. Ghoreyshi and M. Mohammadi, World Appl. Sci. J. 8, 229 (2010)

[5] C. Y. Yin, M. K. Aroua, and A. W. Daud, Sep. Purif. Technol. 52, 403 (2007).

[6] A. K. Geim and A. H. MacDonald, Phys. Today 60, 35 (2007)

[7] K. S. Novoselov, A K. Geim, S. V Morozov, D. Jiang, M. I. Katsnelson, I. V Grigorieva, S. V Dubonos, and A. A. Firsov, Nature 438, 197 (2005)

[8] A. K. Geim and K. S. Novoselov, Nat. Mater. 6, 183 (2007)

[9] K. S. Novoselov, A. K. Geim, S. V. Morozov, D. Jiang, Y. Zhang, S. V. Dubonos, I. Grigorieva, and A. A. Firsov, Science 306, 666 (2004)

[10] F. Perreault, A. Fonseca de Maria, M. Elimelech, Chem. Soc. Rev 44, 5861 (2015)

[11] W. Zhao, Y. Tang, J. Xi, and J. Kong, Appl. Surf. Sci. 326, 276 (2015).

[12] X. Zhang, D. Liu, L. Yang, L. Zhou, and T. You, J. Mater. Chem. A 3, 10031 (2015)

[13] D. Coello Fiallos, C. Vacacela Gómez, G. Tubon Usca, D. C. Pérez, P. Tavolaro, G. Martino, L. S. Caputi, and A. Tavolaro, Int. Conf. Exhib. 1646, 38 (2015)

[14] W. S. Hummers and R. E. Offeman, J. Am. Chem. Soc. 80, 1339 (1958)

[15] D. Marcano, D. V. Kosynkin, J. M. Berlin, a Sinitskii, Z. Sun, A. Slesarev, L. B. Alemany, W. Lu, and J. M. Tour, Acs Nano 4, 4806 (2010)

[16] D. R. Dreyer, S. Park, C. W. Bielawski, and R. S. Rouff, R. Soc. Chem. 39, 228 (2010)

[17] H. Guo, T. Jiao, Q. Zhang, W. Guo, Q. Peng, and X. Yan, Nanoscale Res. Lett. 10, 931 (2015)

[18] P. Bradder, S. K. Ling, S. Wang, and S. Liu, J. Chem. Eng. Data 56, 138 (2011)

[19] T. Hartono, S. Wang, Q. Ma, and Z. Zhu, J. Colloid Interface Sci. 333, 114 (2009)

[20] T. Liu, Y. Li, Q. Du, J. Sun, Y. Jiao, G. Yang, Z. Wang, Y. Xia, W. Zhang, K. Wang, H. Zhu, and D. Wu, Colloids Surfaces B: Biointerfaces 90, 197 (2012)

[21] G. K. Ramesha, A. Vijaya Kumara, H. B. Muralidhara, and S. Sampath, J. Colloid Interface Sci. 361, 270 (2011)

[22] L. Sun and B. Fugetsu, Chem. Eng. J. 240, 565 (2014)

[23] J. Z. Sun, Z. H. Liao, R. W. Si, G. P. Kingori, F. X. Chang, L. Gao, Y. Shen, X. Xiao, X. Y. Wu, and Y. C. Yong, Water Sci. Technol. 70, 1663 (2014)

[24] L. Sun, H. Yu, and B. Fugetsu, Hazardous Materials, 203-204, 101 (2012)

[25] N. A. Travlou, G. Z. Kyzas, N. K. Lazaridis, and E. A. Deliyanni, Langmuir 29, 1657 (2013)

[26] C. Wang, C. Feng, Y. Gao, X. Ma, Q. Wu, and Z. Wang, Chem. Eng. J. 173, 92 (2011)

[27] S. T. Yang, S. Chen, Y. Chang, A. Cao, Y. Liu, and H. Wang, J. Colloid Interface Sci. 359, 24 (2011)

[28] M. Zhao and P. Liu, Desalination 249, 331 (2009)

[29] J. Zhao, W. Ren, and H. M. Cheng, J. Mater. Chem. 22, 20197 (2012)

[30] M. Yusuf, F. M. Elfghi, S. A. Zaidi, E. C. Abdullah, and M. A. Khan, RSC Adv. 5, 50392 (2015)

[31] P. Bhatt and A. Rani, Asian Dye. 10, 51 (2013)

[32] M. Vanaja, K. Paulkumar, M. Baburaja, S. Rajeshkumar, G. Gnanajobitha, C. Malarkodi, M. Sivakavinesan, and G. Annadurai, Bioinorg. Chem. Appl. 2014, 1 (2014)

[33] K. Hunger, Industrial Dyes: Chemistry, Properties, Applications pp. 5-6-540 (2007)

[34] S. Nafisi, A. A. Saboury, N. Keramat, J. F. Neault, and H. A. Tajmir-Riahi, J. Mol. Struct. 827, 35 (2007)

[35] A. Alvarez-Buylla, C. Y. Ling, and J. R. Kirn, J. Neurosci. Methods 33, 129 (1990)

[36] T. Basché and C. Brauche, J. Phys. Chem. 92, 5069 (1988)

[37] E. Baldikova, M. Safarikova, and I. Safarik, J. Magn. Magn. Mater. 380, 181 (2015)

[38] D. Swami and P. Pandit, Nat. Environ. Pollut. Technol. 12, 517 (2013)

[39] P. Sharma, D. J. Botah, M. R. Das, Chem. Phys. Chem. 15, 4019 (2013)

[40] G. Lv, Z. Li, W. T. Jiang, P. H. Chang, J. S. Jean, and K. H. Lin, Chem. Eng. J. 174, 603 (2011).

[41] S. Senthilkumaar, P. R. Varadarajan, K. Porkodi, and C. V. Subbhuraam, J. Colloid Interface Sci. 284, 78 (2005)

[42] H. Shi, W. Li, L. Zhong, and C. Xu, Ind. Eng. Chem. Res. 53, 1108 (2014)

[43] P. Bradder, S. K. Ling, S. Wang, and S. Liu, J. Chem. Eng. Data 56, 138 (2011)

[44] C. Aharoni, and F.C. Tompkins, Academic Press, New York, vol. 21, pp. 1-49 (1970)

[45] D. Robati, B. Mirza, M. Rajabi, O. Moradi, I. Tyagi, S. Agarwal, and V. K. Gupta, Chem. Eng. J. 284, 687 (2016)

[46] E. Kuisma, C. F. Hansson, T. B. Lindberg, C. A. Gillberg, S. Idh, and E. Schröder, J. Chem. Phys. 144 (2016)

[47] E. Khosla, Chem. Applied Biochem. 2, 1 (2016)

[48] Y. S. Ho and G. McKay, Process Biochem. 34, 451 (1999)

[49] W. Rudzinski and W. Plazinski, J. Phys. Chem. C 111, 15100 (2007)

[50] Y. S. Ho, W. T. Chiu, C. S. Hsu, and C. T. Huang, Hydrometallurgy 73, 55 (2004)

[51] Y. S. Ho, Water Res. 40, 119 (2006)

CHAPTER 3

Carbon material:

Synthesis of Carbon nano-onions by arc discharge

3 Carbon Nano-Onions (CNOs)

3.1 Introduction

Carbon is found abundantly in nature as coal or as natural graphite, and much less abundantly as diamond. Carbon has six electrons, two electrons are found in the 1s orbital close to the nucleus, and four valence electrons. When carbon atoms come together to form a crystal, one of the 2s electrons is excited to the $2p_z$ orbitals from energy gained from neighboring nuclei, which has the net effect of lowering the overall energy of the system. Interactions or bonding subsequently follow between the 2s and 2p orbitals of neighboring carbon atoms [1].

Elemental carbon in sp^2 hybridization can form a variety of amazing structures, such as graphite (3D), graphene (2D) [2], carbon nanotubes (1D) [3-6] and fullerene (0D) [7]. Since the discovery of the fullerene C60 in 1985 by Curl, Kroto and Smalley and most recently graphene, the carbon nanomaterials have been the focus of research in different fields. Several other carbon based nanomaterials were discovered; one of them is multi-shell fullerenes, also known as carbon nano-onions (CNOs).

CNOs, which were discovered by Ugarte in 1992 [8], consist of spherical or plyhedral closed carbon shells and their name comes from to the concentric layered structure resembling that of an onion. In the last years, different methods for their synthesis have been developed [96] and their properties have been widely studied.

Between methods for CNOs synthesis reported we can mention detonation soot [10], heat treatment of nanodiamonds [11], electron radiation nanodiamonds [12], arc discharge of graphite in liquid nitrogen or water [13, 15], pyrolization of wood wool [16]. The large scale production was first realized by vacuum annealing of a nanodiamond precursor [10, 11]. The particle size of CNOs produced via nanodiamond annealing is dependent on the nanodiamond precursor, which is generally about 5 nm in diameter, producing onions in the 5-10 nm size range.

The technique of arc discharge between two graphite electrodes in water, basically consist in applying a dc current between two graphite electrodes in water, which causes the

carbon to evaporate at the location of the arc due to the extreme heat generated [13,14, 17]. Arc discharge can be performed at ambient temperature and pressure, avoiding the use of expensive equipment or catalysts. However, the yield is low and samples contain CNOs together with nanotubes and amorphous carbon.

The characteristic properties of CNOs render them of great interest for a large number of applications. The diameter of the CNOs depends on the synthetic protocol, but nevertheless, CNOs exhibit in general a high surface area to volume ratio and distances between the carbon layers of 0.34 nm, which is in good accordance to the distance of the layers in bulk graphite [8]. In a report of 1995, Daniel Ugarte refers to CNOs as onion-like graphitic particles, which display a wide range of structures, explicitly including polyhedral to nearly spherical morphologies in his definition of CNOs [18].

Transmission electron microscopy (TEM) has been widely employed to visualize CNOs and to study the mechanisms of CNO formation and their structural properties. Raman spectroscopy is a useful technique for the structural characterization of CNOs and corroborates the basic graphitic structure of carbon nano-onions. Typically, two broad Raman bands can be readily observed in the range between 1300 and 1600 cm^{-1} [19]. The D-band at around 1350 cm−1 resembles structural disorder due to the presence of sp^3 carbons, while the G-band at around 1580 cm^{-1} corresponds to the E_{2g} mode of sp^2-hybridized carbon frameworks. Covalent CNO functionalization usually leads to an increase of the D-band intensity, due to the increase of sp^3-hybridized carbon atoms.

The method of arc discharge in water has the advantage of the relative simplicity, but the disadvantage of the quantity of CNOs produced, which is quite low. We have applied such method to investigate deeper the mechanism and the possibility to obtain higher CNOs quantities with higher purity.

3.2 Experimental Apparatus

3.2.1 Chassis:

We created a metallic structure, consisting of 2 stainless steel flanges held together by 3 threaded columns to obtain a chassis (Figure 3.1). The upper plate was drilled in the center to allow assembly of the micrometer that would allow a good accuracy of advancement of the anode towards the cathode. Therefore, the micrometer allows the translation towards the cathode during discharge, which is indispensable in maintaining the *gap* constant [13, 14, 20-24]. The lower plate, instead, is characterized by a ceramic zone which isolates it electrically from the rest of the chassis; the cathode stand, made of copper, was precisely mounted on this area.

Figure 3.1 Apparatus assembled to synthesis of CNOs by arc discharge in water.

3.2.2 Power supply

A power supply was used, that allowed the achievement of current values between 0 and 70 A, with a difference of potential between 0V and 24V; this is controlled by a toroidal VARIAC variable power transformer.

The AC exiting the power supply and regulated by the transformer, is then converted into DC power by a rectifier bridge.

Through the use of a tester and of a current clamp, we measured the potential difference before starting the discharge, as well as the value of the current once discharge has started. These readings result as being of fundamental importance in order to maintain a constant arc during the experiment, by acting on the micrometer regulating the translation of the anode. A thermocouple thermometer was fixed in the synthesis chamber to constantly monitor the temperature.

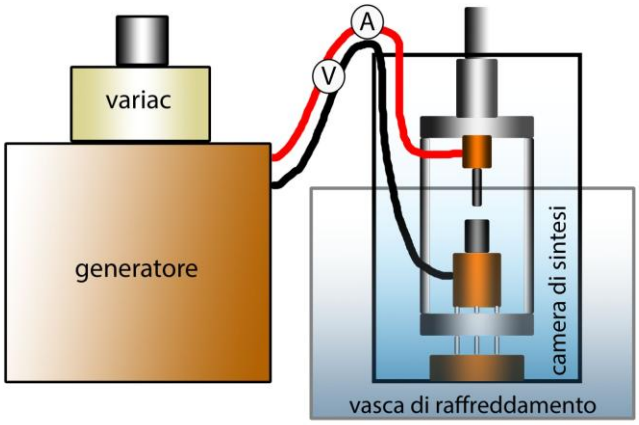

Figure 3.2 Diagram of apparatus for synthesis of CNOs by arc discharge in water.

3.3 Synthesis procedure:

Two graphite electrodes of similar purity (anode and cathode) cut to measure (5 and 10 mm of diameter), and were mounted on the chassis. We then proceeded with the insertion in deionized water with a specific resistivity of 1.4 MΩ with a gap of 1 mm. The arc discharge was initiated by contacting the anode with the cathode (Figure 3.3), the discharge voltage was 15V.

The arc discharge in water was stable maintained anode-cathode gap of about 1 mm. The discharge can be characterized as an anodic arc as the smaller anode electrode is consumed.

The discharge proceeds until the almost total consumption of the anode, maintaining the synthesis chamber temperature under control: in our case, starting from a temperature equal to the ambient temperature (T=25°C) after approximately 70 seconds, a temperature of 83°C was reached, which was kept constant until the end of the discharge.

Figure 3.3 Digital image of the experimental process during arc discharge between anode and cathode of graphite.

3.4 Results and characterization

During the discharge, in the plasmatic zone area on the cathode, a gradual deposition of material occurred, thus forming a small disk-shaped tablet as shown in Figure 3.4. In fact, it grew in correspondence of the center of the arc, and was in the maximum temperature zone. This assessment is essential to compare our results with those reported in the literature [13-15, 25].

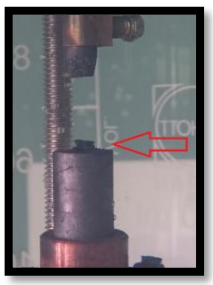

Figure 3.4 Discoid formed on the cathode during arc discharge.

After the discharge, the synthesis chamber presented carbon nanoparticle (CNP) clusters scattered on the bottom and on the surface of the reaction water (Figure 3.5).

- An intense grey powder is present on the surface, formed by floating *clusters* of carbon nanomaterials. The reason is not due to a lower specific weight, which by reported calculations was detected as being 1.64 g/cm^3, but is, instead, due to their hydrophobic surface.
- Instead, on the bottom, there are darker agglomerations.
- The discoid presents a black colour, of a diameter of approximately 4 mm, which was detached through the application of a weak force, leaving the cathode surface perfectly smooth.

Figure 3.5 Material gendered by arc discharge in the synthesis chamber.

Three sample groups were individuated from the synthesis chamber: powder floating on the water surface (S), the material precipitated on the bottom of water (B), and Discoid formed on cathode (D).

The S and B samples were sonicated for 3.5 h, in order to obtain a better dispersion of the carbonaceous material (Figure 3.6). After sonication, 2 phases of the material are

presented: supernatant (s) and precipitate (p); the precipitate material was heated to 80°C to evaporate water, thus the Sp and Bp samples were obtained. The discoid was sonicated in deionized water (Figure 3.6 (c)), and the resulting suspended material (Ds) was collected.

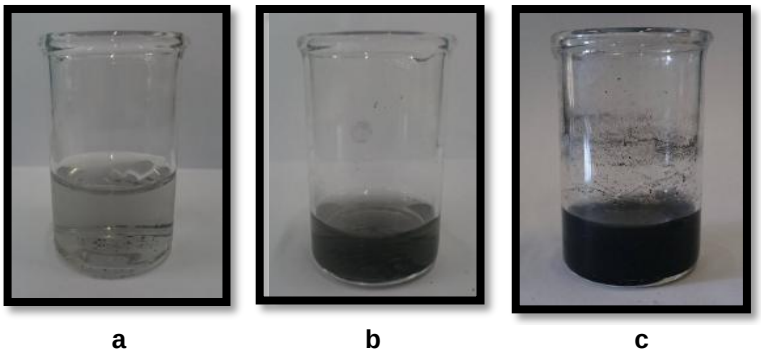

Figure 3.6 Suspensions obtained after sonication of the three groups of material collected in reaction chamber: (a) from surface the reaction water, (b) collected on bottom of reaction water and (c) agglomerate formed on the cathode.

The samples (Sp), (Bp) and (Ds) were characterised by microscopic and spectroscopic techniques. Scanning electron micrographs (SEM) were taken on a field-emission scanning electron microscope (FEI Quanta FEG 400 F7) and Transmission electron micrographs (TEM) were performed in JEOL Jem-2100). Raman spectroscopy were made by using a Horiba-Jobin-Ivon Labram Raman spectrometer with a He Ne laser (632.8 nm) as excitation source.

3.4.1 SEM characterization:

The sample powder Ds, Sp and Bp were characterized first by SEM microscopy technique. The SEM images allowed to distinguish different carbon nanoparticles that present several structures. Figure 3.7 shows relevant SEM image obtained in Ds that evidence particles in spherical forms and polyhedral particles (CNOs). In sample Bp we don't observe structure comparable to CNOs, in fact, Figure 3.8 shows zones of lamellar

structures with some agglomerate of carbon structures of smaller dimensions that hiding some parts of the lamellar structures. In the images obtained from Sp can distinguish zones containing extended planar structure with some smaller spherical particles on the top of them (Figure 3.9 (a)) and lamellar structures of high dimension with thin thickness (Figure 3.9 (b)).

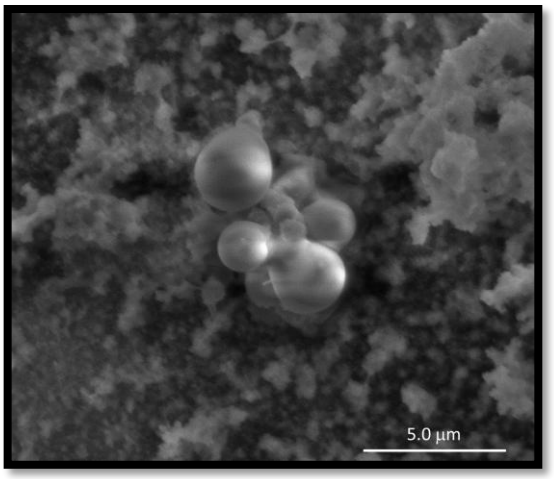

Figure 3.7 SEM image obtained from Ds sample.

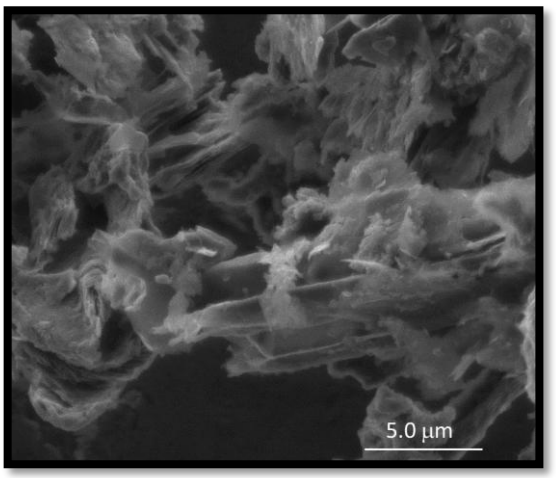

Figure 3.8 SEM image of structures presents in Bp sample

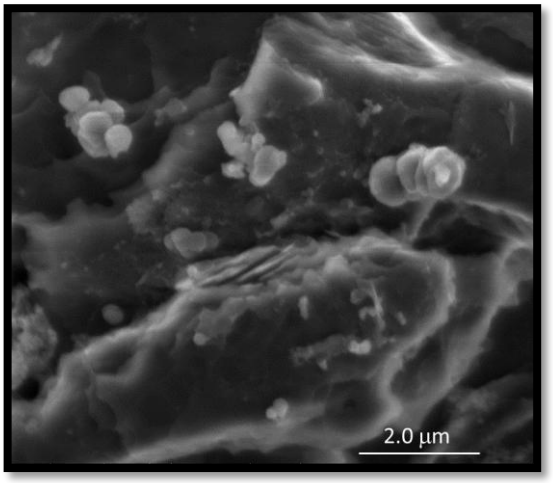

a

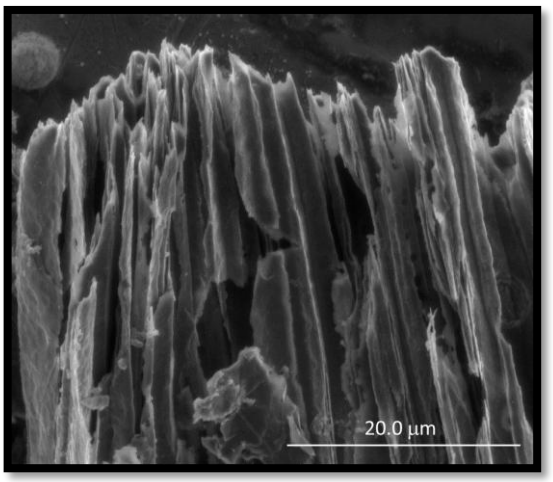

b

Figure 3.9 SEM images of sample Sp (a) defined structures of lamellar form and polyhedral particle, (b) image of lamellar structures.

3.4.2 TEM characterization

TEM images reveal that the samples Sp and Bp are conformed by same CNPs, although were obtained from different zones of synthesis chamber clearly showing the presence of carbon nano-onions (CNOs) and carbon nanotubes (CNTs) of various dimensions, and also some thin structures.

3.4.2.1 Image analysis of Sp sample

Figure 3.10 shows agglomerates of CNTs with CNOs surrounding. The CNOs present dimensions of the order of tens of nanometers and CNTs with diameters of the order of some nanometers.

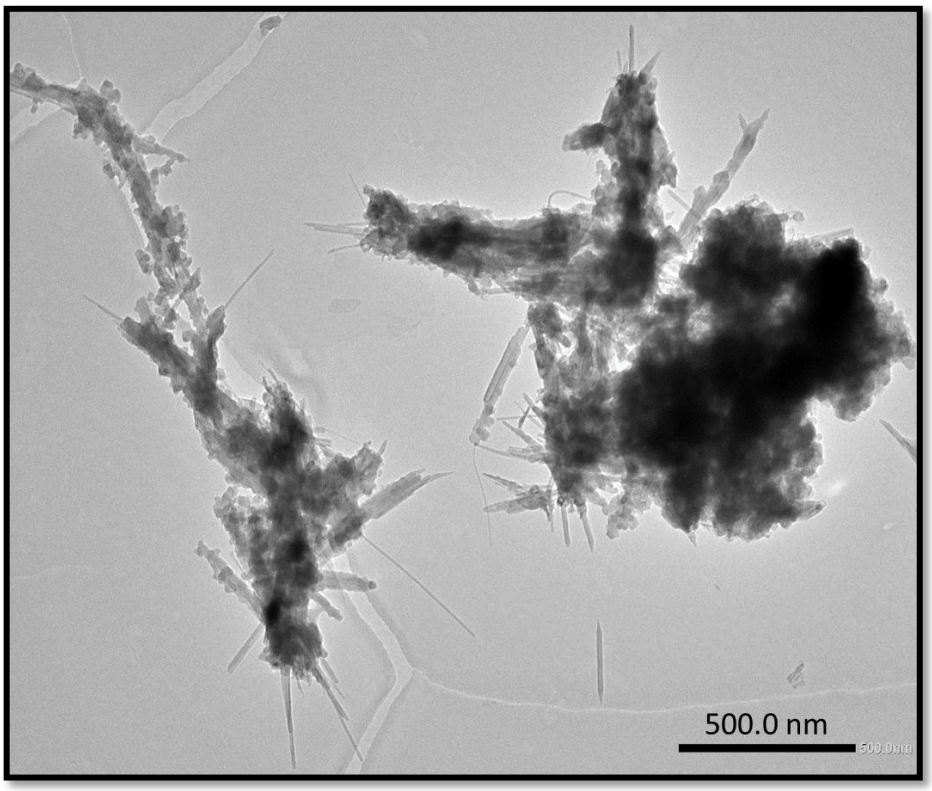

a

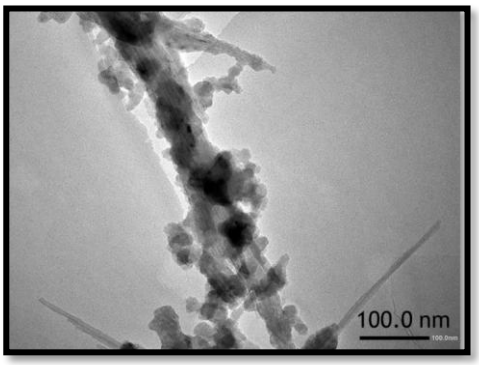

a

Figure 3.10 (a) TEM image shows agglomerates of different CNPs (CNT, CNO, lamellar structures). (b)Zoom image shows clearly agglomerates formed only of CNOs and CNTs

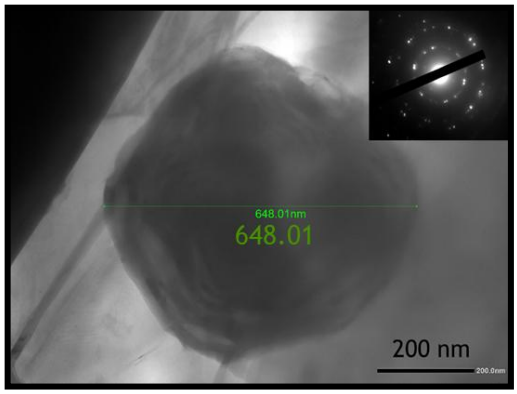

Figure 3.11 TEM image of a carbon-onion of high dimension and inset SEAD image.

Moreover, other image reveal also the presence of some larger particles with dimensions of the order of hundreds of nanometers. Figure 3.11 evidences a CNO of high 640 nm, and its diffraction image, acquired by select-area electron diffraction (SAED). It shows a pattern that can be attributed to a hexagonal structure with rotational disorder.

Thin layered structures of extended dimensions also were found in the Sp samples. Figure 3.12 (a) shows structures with planar geometry that can be attributed to multilayer graphene. We observe also some structures in which graphene layer has lost the typical planarity showing a corrugated geometry (Figure 3.12 (b)), this fact also was observed in other work about synthesis of graphene oxide.

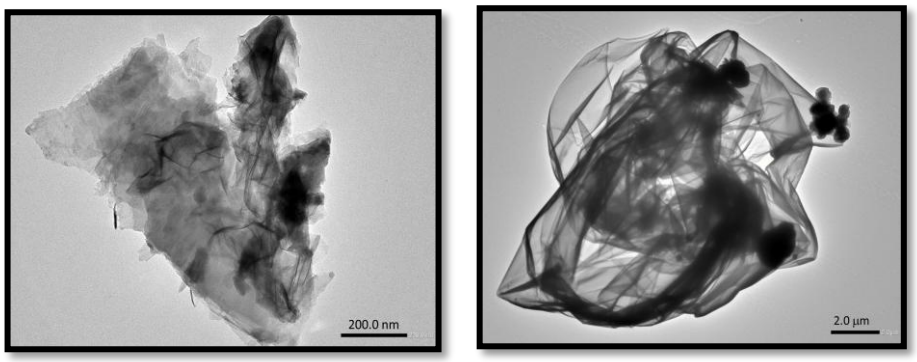

a b

Figure 3.12 TEM images of (a) planar and corrugated fragments without evidence of CNOs and (b) clear corrugate structure of high dimension with low presence of CNOs.

3.4.2.2 Image analysis of Bp sample

Figure 3.13 shows a typical zones contenting CNPs, distinguish structures attributable to nano-onions and nanotubes together with lamellar zones with a multilayer graphene aspect. While in Figure 3.14, CNOs with high dimensions (100 nm) are present in isolated form, and finally in (d) we observe CNO surrounded of smaller CNOs with a diameter dimension around 10 nm.

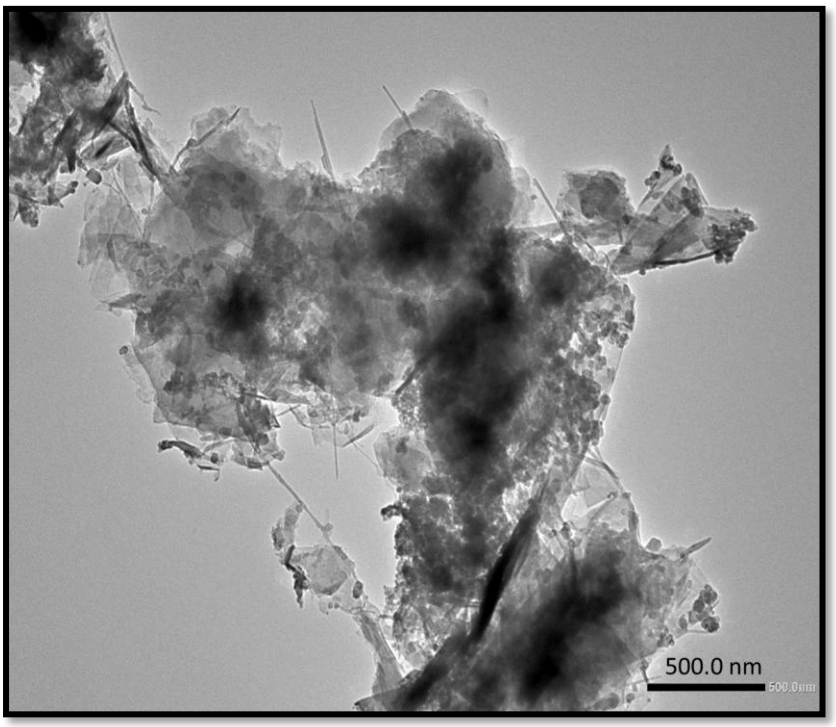

Figure 3.13 TEM images of carbon nanomaterials observed in Bp sample.

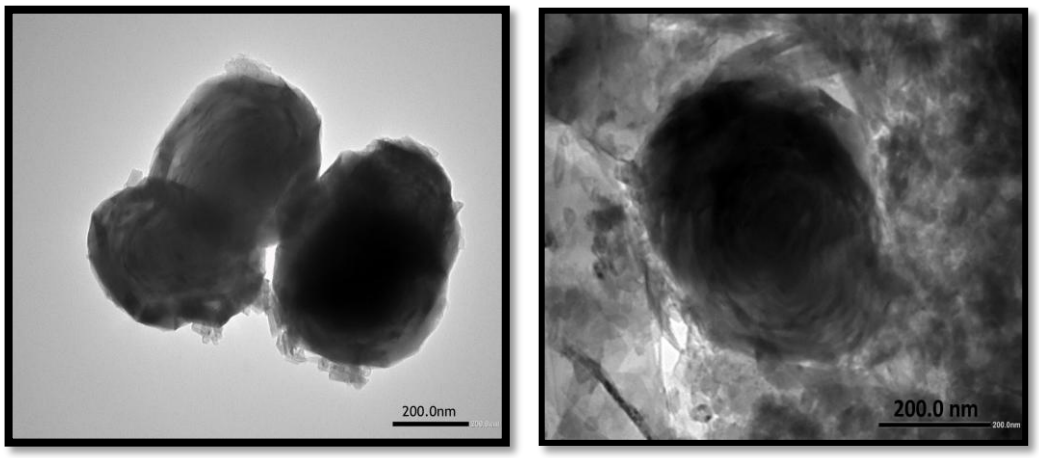

a **b**

Figure 3.14 (a) image conteneting only CNOs of extended diameter observed in Bp sample. (b) CNO of extended diameter and sorrundimg of smaller CNOs.

The presence of CNTs with different diameters is evident in our nanomaterial. In Figure 3.15 both sample Sp (a) and sample Bp (b) show TEM images of CNTs always with CNO agglomerates, which present different dimensions and diameters.

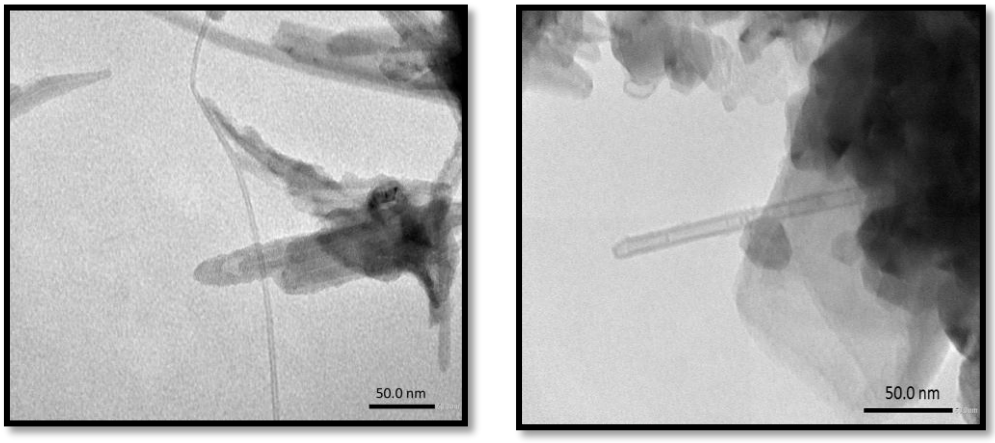

a **b**

Figure 3.15 SEM images of CNTs produced during synthesis of CNOs by arc discharge in water. (a) Sp sample and (b) Bp sample.

3.4.2.3 Image analysis of Ds sample

Different results respect to Sp and Bp are observed on samples obtained by fragmentation of the solid discoid formed in the plasmatic zone. The TEM characterization of Ds sample (Figure 3.16), shows the presence of fragments consisting exclusively of nano-onions with dimensions of the order of tens of nanometers. This is a completely new finding, showing that the discoid formed in the plasmatic zone only needs to be fragmented to obtain a nanomaterial made only of CNOs, without the need of purification methods, as it would be necessary to obtain CNOs from the nanoparticles found on the surface or at the bottom of the vessel.

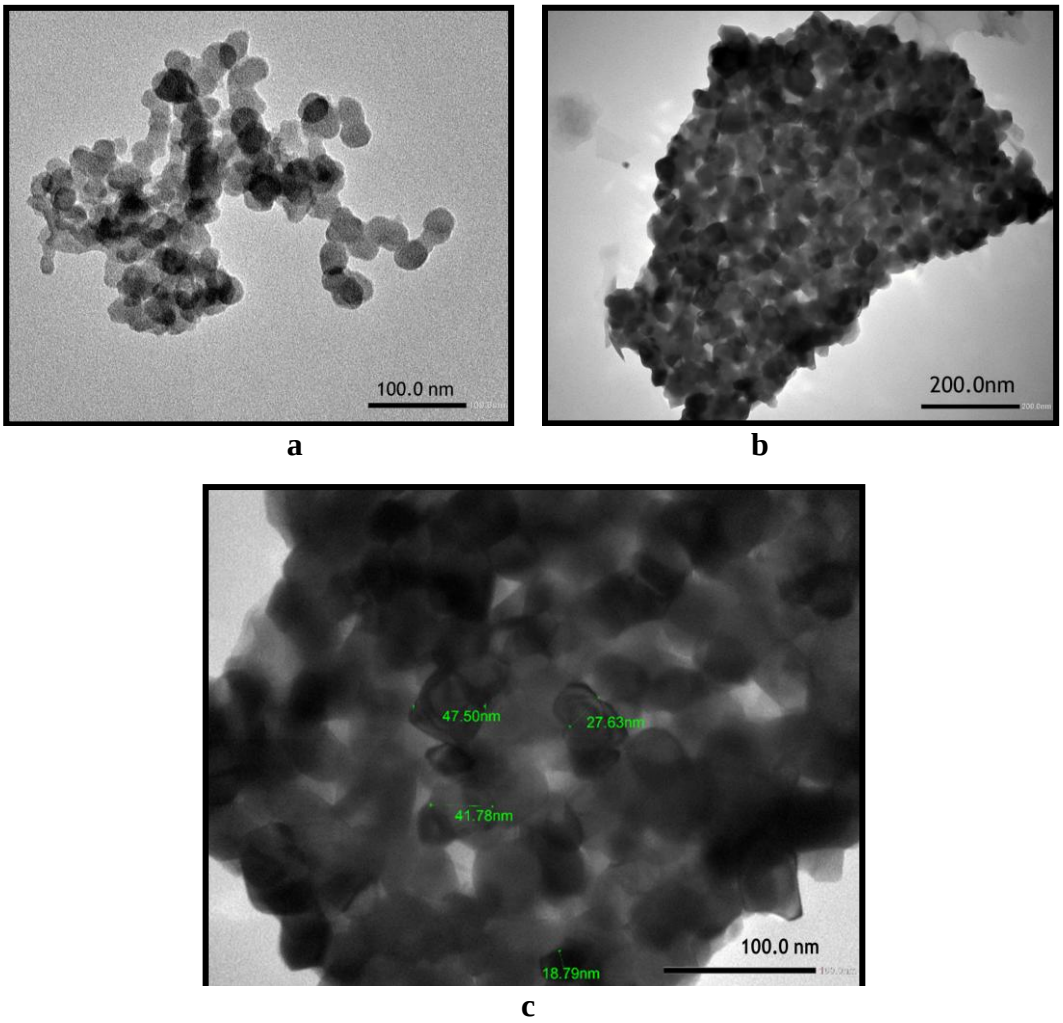

Figure 3.16 TEM images of Ds sample. (a) Fragment consisting of only CNO clearly distinguish each one, (b) a big agglomerate of CNOs, (c) high magnification of CNO whit dimensions under 50 nm.

3.4.3 Raman characterization

Raman spectroscopy is known to be the better method to distinguish between different forms of carbon agglomerates. Materials like graphite, graphene, CNTs and CNOs show well-defined Raman spectra, thus allowing to get important information about the structure of new carbonaceous materials.

The Raman spectrum from Sp samples is indistinguishable of the spectrum from Bp sample, and this is indicative of the fact that they are constituted by very similar carbon structures; therefore, we analyzed one Raman spectrum as representative for both samples.

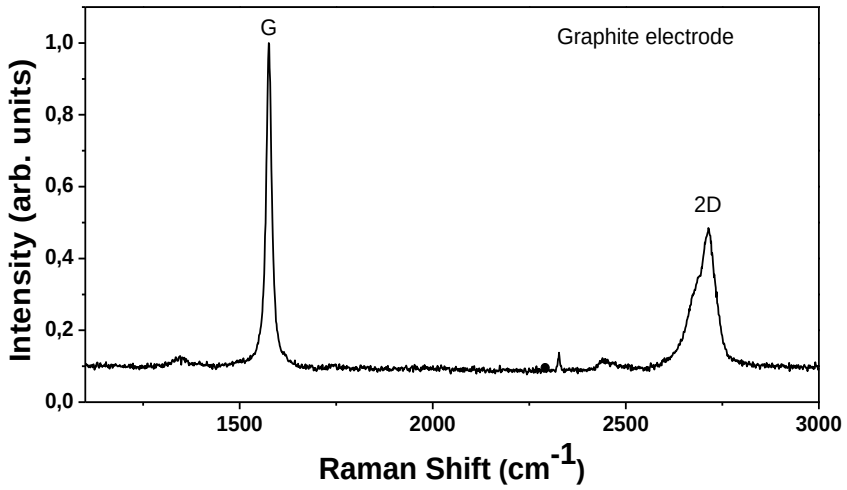

a

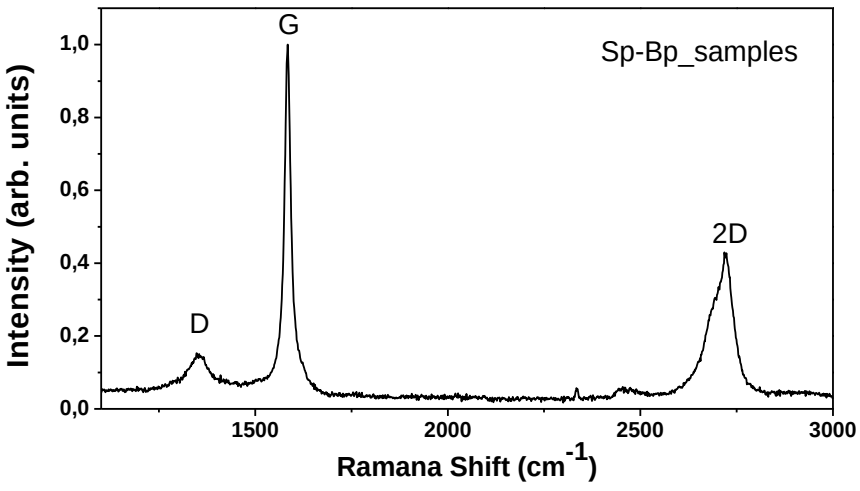

b

Figure 3.17 Raman spectra of graphite (a) and floating CNPs formed on surface (b).

The similarity between Raman spectra of Sp and graphite shown in Figure 3.17 suggests that the anode fragments play a decisive role in determining the shape of Raman spectra of Sp. Furthermore, such fragments show a structural disorder (defects, reduced flake dimensions) that is increased compared to the original material, as shown by the increased intensity of the D peak.

In Figure 3.18 we show the Raman spectra of Sp and Ds. The degree of structural disorder on graphitic planes present in the two samples is similar, as shown by the similar intensity of the D peaks. The most significant difference is found in the form of the 2D peak. Unlike the 2D peak of Sp sample, which presents the typical bimodal shape as in graphite, the spectrum obtained on Ds sample is essentially *monomodal*.

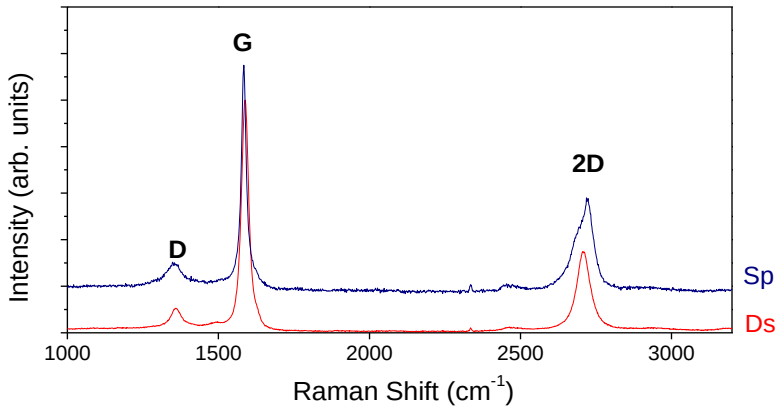

Figure 3.18 Plot of Raman spectra of material floating on surface of water (Sp) and of material of discoid formed on the cathode (Ds).

A monomodal 2D peak can be attributed to turbostratic graphite, namely graphite in which there is rotational disorder in the "stacking" between adjacent graphene sheets. As for the CNOs, it can be hypothesized that the planar areas are formed by turbostratic graphite, and that the curved parts, if present, do not significantly contribute to the 2D peak [8] [20]. Figure 3.19 shows the fit of the 2D band evidence in Raman spectra (a) fit of 2D

band of Ds sample with composition of polyhedral CNOs, and (b) the form of the 2D band reported by D. Codorniu Pujals et al. [25], obtained on polyhedral nano-onions in the presence of curved zones (such as fullerene). It has to be noted that the difference in the 2D peak location compared to our spectrum is due to the use of a laser with a different wavelength (632 nm instead of 514 nm).

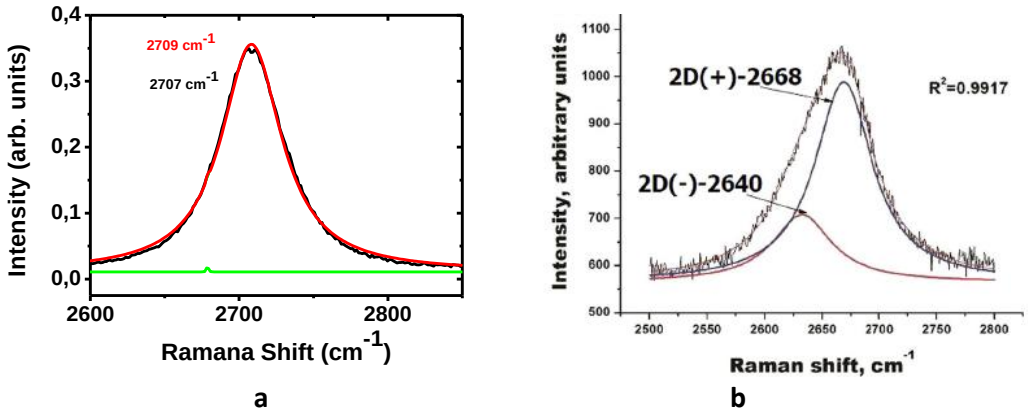

Figure 3.19 (a) Fit of 2D band Raman spectra Ds sample formed exclusively of CNOs fragments. (b) Fit of the 2D band of polyhedral CNOs [25].

3.5 CONCLUSIONS :

The results obtained show that the discharge procedure in deionized water between two graphite electrodes generated carbonaceous nanostructures with different geometry. There are, in fact, polyhedral CNOs with diameters ranging from tens to hundreds of nanometers, MWCNTs with a variable diameter between approximately 10 and 20 nm, and planar structures also extended up to a few micrometers, attributable to multi-layer graphene, which in some cases show typical graphite oxide undulations. In the samples collected at the bottom and on the surface of the reaction vessel, there are also carbonaceous structures that do not have a particular symmetry, probably due to a

fragmentation of the anode not followed by a rearrangement process in the plasmatic environment.

Our results showed that, under our experimental conditions, there is a similar percentage of CNOs and CNTs in samples taken on the water surface and on the bottom of the reaction vessel. In these samples, the CNOs have variable dimensions in a very high range, the presence of a considerable quantity of CNOs with a diameter of the order of tens of nanometers is noted, as well as the presence of a numerically lower quantity of CNOs with dimensions of up to 400 nanometers.

The presence of thin undulated nanostructures along with thin planar nanostructures is very important. This last can be interpreted as multi-layer graphene, and their presence is compatible with an exfoliation process of the anode fragments guided by the pressure conditions present in the vicinity of the plasmatic zone. The undulated structures are rather similar to those observed on the graphene oxide samples of our previous work, obtained by chemical synthesis. A comparison of SEM images of graphene oxide Figure 3.20 and TEM image of thin undulated nanostructures (Figure 3.12 (b)) has considerable importance. In fact, the formation of graphene oxide in experiments of arc discharge between graphite electrodes has never been observed before.

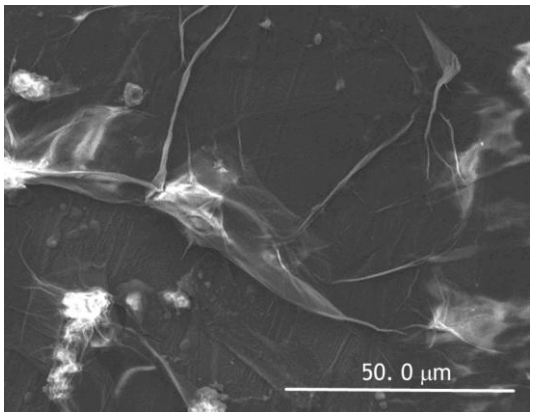

Figure 3.20 SEM image of thin undulated nanostructure (GO-4A).

Perhaps the more important observation in our experiments is the formation of a solid agglomerate in the zone of the plasma, which remains on the cathode but is not

bonded to it. In fact, the cathode surface remains unchanged after having removed such agglomerate. Raman and TEM studies revealed that the agglomerate is made exclusively of CNOs, and this is a particularly important finding, in view of the fact that complex purification procedures are usually necessary to obtain small CNOs quantities from the carbonaceous particles which are found in the discharge water.

Our results lead us to make some hypotheses on the way in which, following the sublimation of carbon atoms, crystallization takes place to form the detected nanostructures. In our experiments, the formation of the agglomerate of CNOs, formed on the cathode surface in full plasmatic zone, contradicts the mechanism proposed in the literature [13-15].

Sano and coworkers reported [13] that from a gaseous state reached at the center of the plasmatic zone (sublimation), the carbon atoms, pushed outwards by the pressure of gases generated, crystallize by means of an epitaxial temperature gradient, assuming the allotropic forms typical of carbon nanostructures:

- The CNTs are formed in the area immediately adjacent to the plasmatic zone, favored by the presence of an epitaxial current of C^+ ions.
- The CNOs formed immediately in the immediately successive zone, where there is an absence of an epitaxial current, promote an increase of isotropic structures.

In our work, the presence of an agglomerate of discoidal form adhering to the cathode surface in correspondence of the axial position of the anode during the electrical discharge, but in reality easily withdrawable from the cathode surface without leaving macroscopic signs of damage, is incompatible with the model reported by Sano et al.

Figure 3.21 shows the mechanism we propose for the formation of the discoidal agglomerate made of CNOs. Such formation can only be explained if we assume that the

synthesis of the nanostructures occurs in the plasmatic zone because of the temperature gradient very close to the cathode surface, and that such nanostructures are deposited on the cathode, forming the discoid of CNOs.

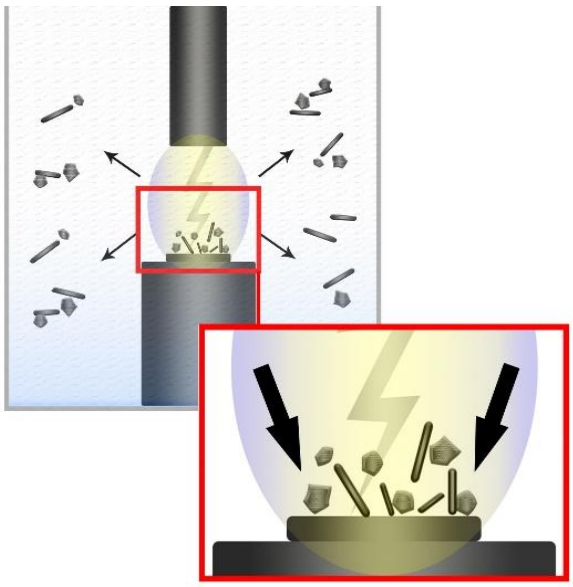

Figure 3.21 Schema of the mechanism of formation of CNPs in our synthesis.

Furthermore, the TEM and Raman results show that there are notable differences between the particles deposited on the cathode forming the discoid and those present in suspension. The TEM images show that the CNOs present in the discoid all have dimensions of the order of tens of nanometers, and they are not observed with much larger dimensions (up to 600 nanometers) as in the case of the samples in suspension. In some fragments, they result as being linked to nanotubes of various diameters, but there are also fragments consisting only of CNOs.

It should also be noted that the images of the fragments which constitute the discoid show no apparent areas of "disorder", as in the case of the fragments in suspension. The

discoid is mainly made of CNOs, and this observation is in agreement with the Raman spectrum obtained on the agglomeration area.

3.6 References

[1] R. Saito, G. Dresselhaus, M. S. Dresselhaus, Imperial College Press, London WC2H 9HE, (1999).

[2] K. S. Novoselov, et al., Science, 306, 666 (2004).

[3] S. Iijima, Nature, 354, 56 (1991).

[4] S. Ijima and T. Ichihashi, Nature London 363, 603 (1993).

[5] Y. L. Hsin, K. C. Hwang, F. R. Chen, and J. J. Kai, Adv. Mater. 13, 830 (2001).

[6] S. J. Lee, H. K. Baik, J. Yoo, J. H. Han, Diamond and Related Materials 11, 914 (2002).

[7] H. W. Kroto, J. R. Heath, S. C. O'Brien, R. F. Curl, R. E. Smalley, Nature, 318, 162 (1985).

[8] D. Ugarte,. Nature, 359, 707 (1992).

[9] L. Echegoyen, A. Ortiz, M. N. Chaur, A. J. Palkar, Carbon Nano Onions. In Chemistry of Nanocarbons; Akasaka, T.; Wudl, F.; Nagase, S., Eds.; John Wiley & Sons: Chichester, UK, pp 463–483 (2010).

[10] N. L. Kuznetsov, A. L. Chuvilin, E. M. Moroz, V. N. Kolomiichuk, S. K. Shaikhudtdinov, Y. V. Butenko, I. Y. Mal'kov, Carbon 32, 873 (1994).

[11] N. L. Kuznetsov, A. L. Chuvilin, Y. V. Butenko, I. Y. Mal'kov, V. M. Titov, Chem. Phys. Lett., 222, 343 (1994).

[12] L.-C. Qin, S. Iijima, Chem. Phys. Lett., 262, 252 (1996).

[13] N. Sano, H. Wang, M. Chowalla, I. Alexandrou, and G. A. J. Amaratunga, Nature London 414, 506 (2001).

[14] N. Sano, H. Wang, I. Alexandrou, M. Chhowalla, K. B. K. Teo, G. A. J. Amaratunga, J. Appl. Phys., 92, 2783 (2002).

[15] I. Alexandrou, H. Wang, N. Sano, G. A. J. Amaratunga, J. Chem. Phys., 120, 1055 (2004).

[16] M. Ghosh, S. K. Sonkar, M. Saxena, S. Sarkar, Small, 7, 3170 (2011).

[17] J. K. McDonough and Y. Gogotsi, Electrochem. Soc. Interface • Fall, 61 (2013).

[18] D. Ugarte, Carbon, 33, 989 (1995).

[19] S. Tomita, T. Sakurai, H. Ohta, M. Fujii, S. Hayashi, J. Chem. Phys., 114, 7477 (2001).

[20] N. Sano, T. Charinpanitkul, T. Kanki, W. Tanthapanichakoon, J. Appl. Phys. 96 (2004).

[21] N. Sano, M. Naito, M. Chhowalla, T. Kikuchi, D. Matsuda, K Iimura, H. Wang, T. Kanki, G. A. J. Amaratunga, Chem. Phys. Lett. 378, 29 (2003).

[22] Y. I. Kim, E. Nishikawa, T. Kioka, J. Plasma Fusiom Res. 8, 612 (2009).

[23] S. Jong Lee, H. Koo Baik, J. Yoo, J. Hoon Han, Diamond an Related Material, 11, 914 (2002).

[24] F. Han, B. Yao, Y. Bai, J. Phys. Chem. C, 8923 (2011).

[25] D. C. Pujals, O. Arias de Fuentes, L. F. Desdin Garcia, E. Cazzanelli, Lorenzo S. Caputi, Appl. Phys. A, 120,1339 (2015).

[26] E.F. Antunes, A.O. Lobo, E.J. Corat, V.J. Trava-Airoldi, 45, 913 (2007).

[27] E.F. Antunes, A.O. Lobo, E.J. Corat, V.J. Trava-Airoldi, A. A Martin C. Verissimo, Carbon, 44, 2202 (2006).

CHAPTER 4

SURFACE NANOSCIENCE SPECTROSCOPY:

Experimental study of Indio Selenium compound

4 Surface Nanoscience Spectroscopy

4.1 Introduction of the Apparatus

In this chapter will be presented measurements performed during my PhD thesis, in the Nanoscience laboratory of department of physics to study material of high interest in different fields. The experimental data information was acquired in an Ultra-High Vacuum (UHV) chamber (Figure 4.1), operating at a conventional pressure of about 2×10^{-10} mbar.

UHV is a necessary condition for many surface analytic techniques to reduce surface contamination, by reducing the number of molecules reaching the sample over a given time period. Typically, UHV requires high pumping speed, possibly multiple vacuum pumps in series and/or parallel.

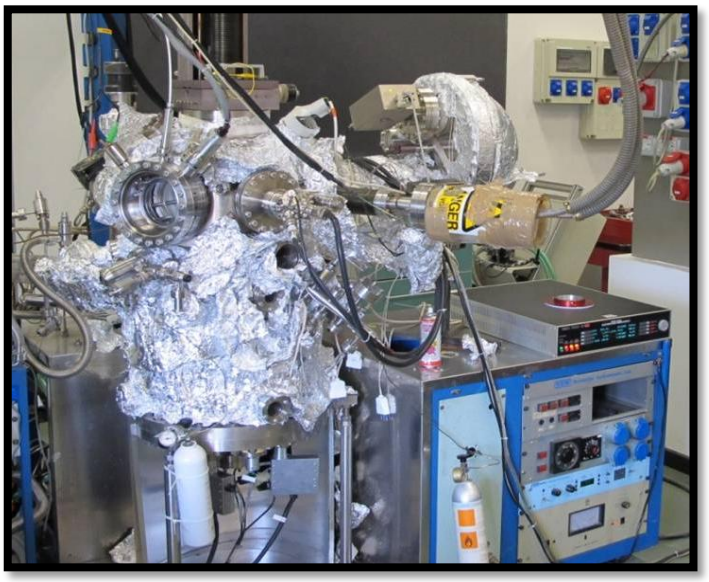

Figure 4.1 Ultra High Vacuum Chamber in Nanoscience Laboratory

The UHV chamber is divided into two communicant sections:

In the upper section we perform technique as well as Electron Energy Loss Spectroscopy (EELS), Low Electron Energy Diffraction (LEED), Auger Electron Spectroscopy (AES) and X-Ray Photoelectron Spectroscopy (XPS). For this techniques is present a conventional electron gun that generates a directional electron beam at different energy (20-1200 eV), an X-Ray source and a hemispherical electron energy analyzer that can collect the electrons emitted (or scattered) by the sample. In the upper section are also present three gas-lines for the release of gas in the analysis chamber, and an ion gun that generates a beam of argon ions with a well-defined energy distribution.

The lower part of the UHV chamber contains an apparatus for High Resolution Electron Energy Loss Spectroscopy (HREELS) made of a fixed monochromator and a rotating analyzer, both 50mm electrostatic hemispherical. The angular acceptance of the analyzer is 2°.

4.2 Low Energy Electron Diffraction (LEED):

LEED is a technique that allows to have information about the order and symmetry of atoms at the surface of a crystal through the diffraction of electrons with low energy. LEED spectroscopy admit the determination of the surface structure of single-crystalline materials by bombardment with low energy electrons (20–200 eV) and observation of diffracted electrons as spots on a fluorescent screen (Figure 4.2).

Figure 4.2 Picture of low energy electron difraction apparatus.

The LEED detector usually contains an electron gun, three or four hemispherical concentric grids and a phosphor screen. Electron gun can produce electrons with energy from 20 to 200 eV, the electrons are emitted by a cathode filament which is at a negative potential, with respect to the sample. The electrons are accelerated and focused into a beam, with a typical width that extends from 0.1 to 0.5 mm, some of the electrons incident on the sample surface are backscattered elastically, and diffraction can be detected when the sample has an order surface. The grids are used for screening out the inelastic scattered electrons (Figure 4.3); therefore the first grid screens the space above the sample from the retarding field, the next grid is at a potential to block low energy electrons, it is called the suppressor and is a retarding field analyzer to block inelastically scattered electrons.

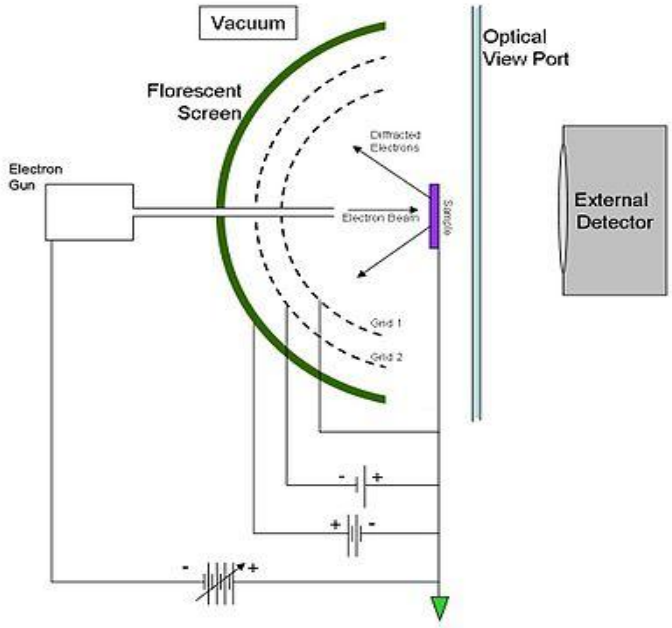

Figure 4.3 Diagram of Low Energy Electron Diffraction apparatus.

Only the elastically scattered electrons are accelerated and hit a fluorescent screen producing the projecting of the reciprocal lattice of the sample (diffraction LEED pattern).

4.2.1 Theoretical fundaments

In the theory the electron beam is represented by a plane wave with a wavelength in accordance to the de Broglie hypothesis:

$$\lambda = \frac{}{}, \qquad \lambda\,[\text{nm}] \approx \frac{}{}$$

The interaction between the scattering centers present in the surface and the incident electrons is most conveniently described in reciprocal space. In three dimensions the

primitive reciprocal lattice vectors {**a*, b*, c***} are related to the real space lattice {**a, b, c**} in the following way:

$$\mathbf{a}^* = \frac{\quad}{\quad} \qquad \mathbf{b}^* = \frac{\quad}{\quad} \qquad \mathbf{c}^* = \frac{\quad}{\quad}$$

For an incident electron with wave vector $k_0=2\pi/\lambda_0$ and scattered wave vector $k=2\pi/\lambda$, the condition for constructive interference and hence diffraction of scattered electron waves is given by the Laue condition:

$$\mathbf{k}-\mathbf{k}_0 = \mathbf{G}_{hkl},$$

where, (h,k,l) is a set of integers and $\mathbf{G}_{hkl}=h\mathbf{a}^*+k\mathbf{b}^*+l\mathbf{c}^*$ is a vector of the reciprocal lattice (Figure 4.4). The magnitudes of the wave vectors are unchanged, i.e. $|\mathbf{k}_0| = |\mathbf{k}|$, since only elastic scattering is considered. Since the mean free path of low energy electrons in a crystal is only a few angstroms, only the first few atomic layers contribute to the diffraction. This means that there are no diffraction conditions in the direction perpendicular to the sample surface. As a consequence the reciprocal lattice of a surface is a 2D lattice with rods extending perpendicular from each lattice point.

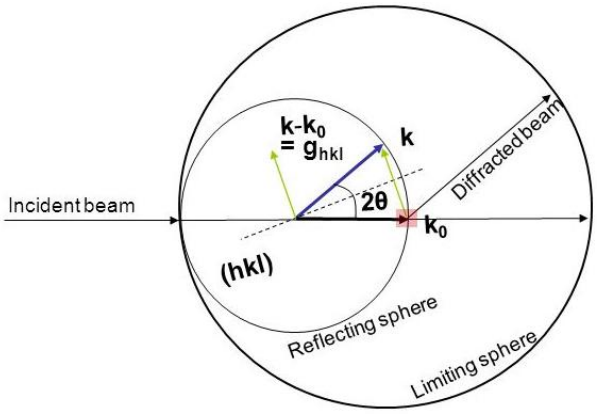

Figure 4.4 Ewald's sphere construction for the case of diffraction from a 2D-lattice.

4.3 X-ray Photoelectron Spectroscopy (XPS)

The main component of a XPS system include a source of X-rays, based on the fluorescent emission of photons from a magnesium or aluminum slab caused by high energetic electrons emitted by a filament and accelerated towards the anode by a voltage of the order of some KeV.

Non-monochromatic magnesium X-rays have a wavelength of 9.89 angstroms which corresponds to a photon energy of 1253 eV. The energy width of the non-monochromatic X-ray is roughly 0.70 eV, which is the ultimate energy resolution of a system using non-monochromatic X-rays.

The mean free path of electrons in solids is very small, the detected electrons originate from only the top few atomic layers, making XPS a unique surface-sensitive technique for chemical analysis. Quantitative data can be obtained from peak heights or peak areas and identification of chemical states often can be made from exact measurements of peak positions and separations. Each element has a unique set of binding

energies, XPS can be used to identify and determine the concentration of the elements in the surface. Variations in the elemental binding energies (chemical shifts) arise from differences in the chemical potential and polarizability of compounds. These chemical shifts can be used to identify the chemical state of the materials being analyzed.

The Auger electrons come from the homonymous process and, as well known, their energies are independent from the photon incident energy, so each peak of the auger spectra is characteristic of a specific element.

Instead, the photo-electrons energy depends on the photon incident energy according to the following equation:

where,

is the kinetic energy of the detected electron,

is the energy of the incident photon,

is the binding energy of the atomic orbital from which the electron originates

is the analyzer work function.

The binding energy is a characteristic of a specific element, in fact, usually, intensity of peaks (I) in the XPS spectra are represented as function of the binding energy (BE).

4.4 Electron Energy Loss Spectroscopy (EELS)

4.4.1 Introduction:

EELS is one of the most common surface analysis techniques used to investigate the excitations in a crystal, caused by an incident electrons beam called primary beam, by analyzing the energy spectrum of electrons backscattered from it. An electron passing through material can interact with electron clouds of the atoms present and transfer some of its kinetic energy to them. There are two modes of operating for EELS:

1. Electron Energy Loss Spectroscopy in transmission mode
2. Electron Energy Loss Spectroscopy in reflection mode

EELS in transmission mode uses electrons from 0.1 to 10 keV. At high energies, the incident electrons beam passes through a thin foil of the material of interest and the transmitted one contains inelastically scattered electrons whose energy has been decreased by amounts corresponding to characteristic absorption frequencies in the solid. At lower energies, (from few to hundreds of eV) the Energy Loss Spectroscopy is used in reflection mode, in this approach the reflected beam is monitored for the electronic excitations occurred in the surface. Bulk and surface plasmons are the principal features of these spectra.

High Resolution EELS employs a monochromatic incident electron beam of quite low energy (a few eV). The primary focus of this technique is the study of vibrational structure of the surface and especially of adsorbates on that surface. The energy of the primary beam has fundamental importance to understand how deep the sample is probed,

in fact the Figure 4.5 represents the mean free path (counted in monolayers) versus the energy of the incident electron beam.

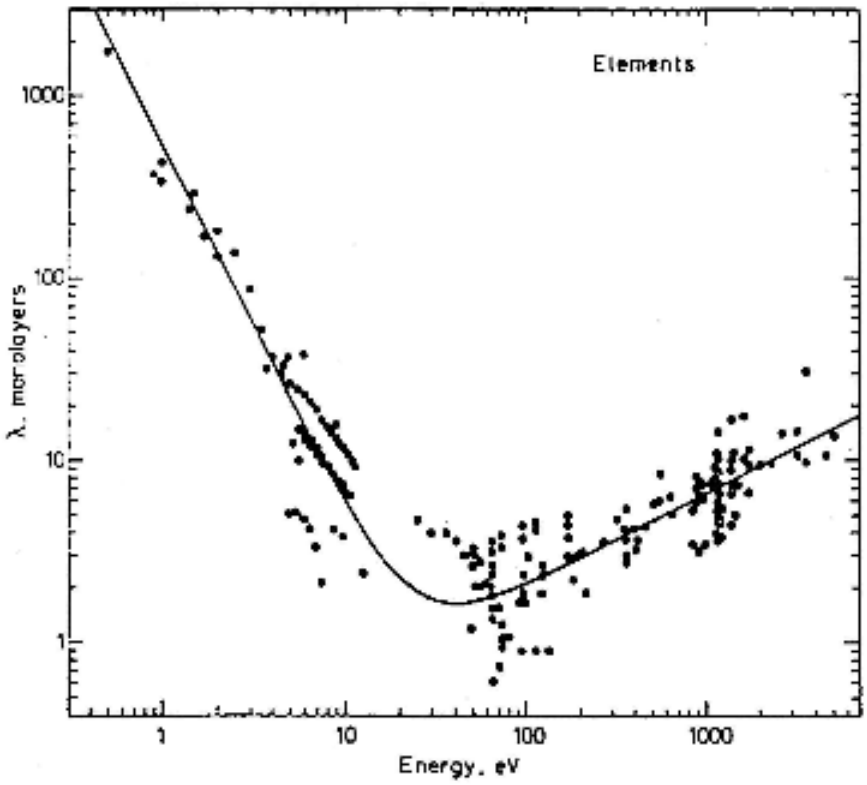

Figure 4.5 Electrons mean free path as function of their energies.

The mean free path, that is the mean distance covered by an electron in a medium before to undergo an inelastic collision, shows a minimum around 50 eV, and after this minimum, increasing primary energy implies the increasing of the mean free path. This graph is universal, it means that it's a good estimate of electrons mean free path in all medium, and also shows that for probe more than 10 monolayers (10-20 Å) of materials it's necessary to use electrons of more than 1000 eV of energy; therefore, all our measurements, carried out at a primary energy of about 100 eV, characterized mainly the surface properties of the sample. Similarly, also measurements obtained by X-Ray

excitation source are surface sensitive, in fact, as assumed above, *although the photons* can penetrate more and more than the electron probe, the analyzer scans only the electrons coming from the outer layers very near to the surface of the sample.

4.4.2 Electron Energy-Loss Spectrum:

In electron energy-loss spectroscopy, we deal directly with the *primary* process of electron excitation, which results in the fast electron losing a characteristic amount of energy. The electron beam scattered by the sample is directed into a high-resolution electron spectrometer that separates the electrons according to their kinetic energy and produces an *electron energy-loss spectrum* showing the number of electrons (scattered intensity) as a function of their decrease in kinetic energy.

The scattered electrons have principally the same energy of the incident electron beam (elastic peak) and only few electrons are emitted with lower energy respect to the primary energy. These latter are inelastic electrons and the energy they lost (E_{loss}) is the same energy that the crystal absorbed to produce an excitation.

The sample excitations induced by an electronic perturbation, are mainly divided into three groups, each for a specific energy range:

1. Core electron excitations (E_{loss} of the order of hundreds of eV)
2. Valence band excitations (single particle interband or intraband transitions), surface and bulk collective excitations (plasmons) (E_{loss} of the order of tens of eV).

3. Vibrational excitations of the sample (acoustic and optic phonon) and vibrational excitations of atoms or molecules adsorbed on the surface (E_{loss} of the order of meV).

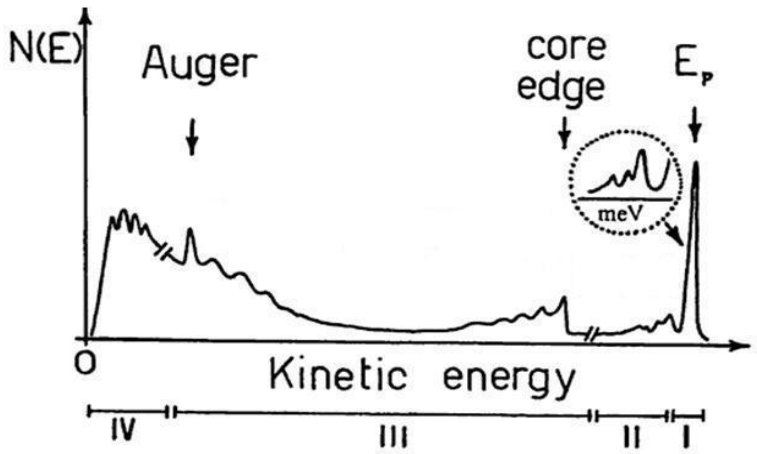

Figure 4.6 Energy of the electrons emitted after the interaction with a beam of primary electrons of energy Ep.

In Figure 4.6 is plotted the typical energy distribution *N(E)* of the electrons emitted by the crystal after the interaction with a beam of primary electrons of energy E_p. The previous figure can be divided in four sections, each of which represents different range of E_{loss} with different sample information:

The region **I** includes the highest peak of the energy distribution with energy E_p that is the elastic peak and allows finding information about the structure of the sample. It contains all electrons that have passed the specimen without any interaction or with an elastic interaction only. In the vicinity of the elastic peak, in the same energy range, there are vibrational excitations which can be determined only by the high resolution EELS (HREELS). By means of these losses it is possible to obtain information about the

vibrational modes of the crystal (phonons) and the vibrational excitations of atoms and molecules adsorbed on the surface.

In the second region (**II)** it is possible to distinguish all the electrons that had inelastic interaction with the solid. The EELS spectroscopy is used, in this energy range, to have information about surface and bulk collective excitations and therefore about its dielectric function. Here, the plasmon peaks are the predominant features.

The third region (**III**) contains electrons which suffered higher energy losses and secondary electrons at high energy. At an energy loss of ca.100 eV, the signal intensity drops rapidly. In this energy range Auger electrons and core electron excitations are present. As in an X-ray spectrum there are additional peaks at well-defined sites in the EELS above the background. These ionization edges appear at electron energy losses that are again typical for a specific element and thus qualitative analysis of a material is possible by EELS. The onset of such an ionization edge corresponds to the threshold energy that is necessary to promote an inner shell electron from its energetically favored ground state to the lowest unoccupied level. This energy is specific for a certain shell and for a certain element. Above this threshold energy, all energy losses are possible since an electron transferred to the vacuum might carry any amount of additional energy. If the atom has a well-structured density of states (DOS) around the Fermi level, not all transitions are equally likely. This gives rise to a fine structure of the area close to the edge that reflects the DOS and gives information about the bonding state. This method is called electron energy loss near edge structure (ELNES). From a careful evaluation of the fine structure farther away from the edge, until hundreds eV above the core excitations,

information about coordination and interatomic distances are obtainable (extended energy loss fine structure, EXELFS).

In the last region (**IV**) is an high and wide peak caused by the secondary electrons, also this peak has a fine structure that can be analyzed by the angle-resolved Secondary Electron Emission (SEE). This analysis provides information about the density and the dispersion of empty states just above the Fermi level.

There are several basic flavors of EELS, primarily classified by the geometry and by the kinetic energy of the incident electrons. Probably the most common today is transmission EELS, in which the kinetic energies are typically 100 to 300 keV and the incident electrons pass entirely through the material sample. Usually this occurs in a transmission electron microscope (TEM), although some dedicated systems exist which enable extreme resolution in terms of energy and momentum transfer at the expense of spatial resolution.

Instead, the reflection geometry is particularly sensitive to surface properties but is limited to very small energy losses such as those associated with surface plasmons or direct interband transitions. Lucas e Sunjc[1] made the first publications about this, followed by Evans e Mills[2-4].

The EELS spectroscopy has several analogies with the optic one, in fact both techniques allow information about the density of electronic bands in the examined solid. EELS, however, makes it possible to change easily the energy of the incident beam, in order to probe a larger energy range. Furthermore, the low mean free path of electrons in the

reflection geometry makes this technique more sensible to the surface proprieties with respect to optical spectroscopy.

4.4.3 Theoretical fundaments

In a continuous and homogeneous medium, the response to an electric external perturbation can be described by the dielectric theory. When an electron approaches a dielectric material, the electron density inside the solid changes to shield the long range electric field produced by the incoming perturbation. The density fluctuations generated inside the medium are related to the wave vector and the frequency of the external field, so the transferred energy depends on the field density energy variation inside the solid.

An electron inside the solid can acquire energy and impulse , because of inelastic interaction with an incident electron, if it lost the same amount of energy

.

The incident electron can be described by the electronic distribution:

The interaction potential produced inside the solid, follows the Poisson equation:

If we pass in the Fourier space, the transform function of is:

The energy loss of the electron in length unit inside the medium is , where is the component of the electric field along the x axis, perpendicular to the surface. Whereas

Replacing in this equation, the expression found for we obtain the loss energy probability in length unit as function of the exchanged moment and of the frequency :

Where —— ——— is the bulk loss function.

So the bulk loss function describes the inelastic interaction of high energy electrons that pass through the sample.

A maximum in the loss function occurs when and . One can see that the condition under which corresponds to the excitation of a plasma wave in the medium.

The most used models to describe a solid material are the Drude and Lorentz models [5]. The first one deals the conduction electrons as a free electrons gas not subject to atomic potential, and in this case the dielectric function, in the limit of , is:

where is the plasma frequency —— and is the relaxing time that takes into account the interactions between the electrons.

In the following figure is represented the real and the imaginary part of and

.

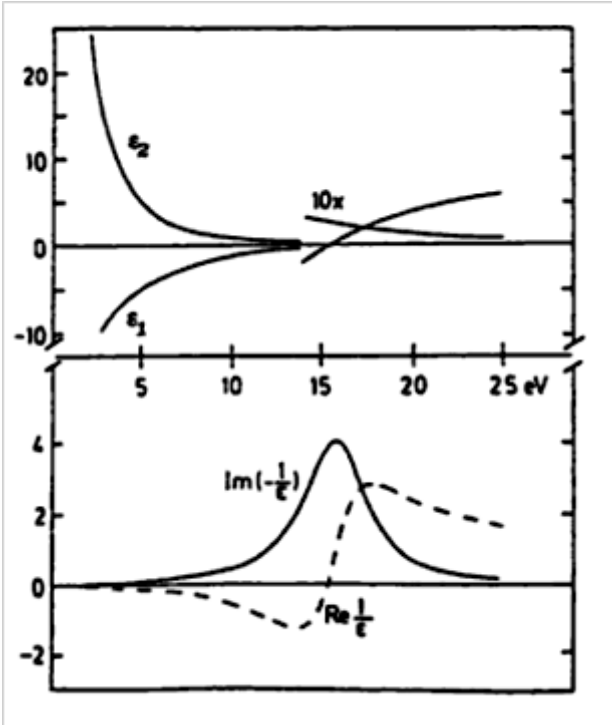

Figure 4.7 Real and imaginary part of the dielectric function ε (upper side) and real and imaginary part of 1/ ε (bottom side) for the Drude model.

The imaginary part of the dielectric function (Figure 4.7), is monotonically decreasing and does not exhibit any structure, so a free electron gas does not generate any optical absorption. The loss function, instead, exhibits a maximum at the plasma frequency , corresponding to the excitation energy of a bulk plasmon in a free electron gas (from several eV to few tens of eV).

Lorentz model is based on treating electrons as damped harmonically bound particles subject to external electric fields. This model describes successfully bound electrons in a solid interacting with an electric field **E** and affected by an elastic-like restoring force with a own resonance frequency . Furthermore, to adapt, this ideal model to the experimental reality, the existence of a viscous term is assumed that can explain the linewidths experimentally observed and avoid annoying divergences. The real materials have different resonances with different intensities, so it is associated at the resonance frequency , an empirical parameter called oscillator strength factor through which it possible to weigh the different intensities, so it satisfies the relation:

To obtain the Lorentz oscillator relation, in the single resonance frequency case, we start from the second law of dynamics:

Where is the electron mass, is the electron charge and is the electron external field applied to the material. Solving the equation for and replacing the external field by , it is obtained:

Using the equations for the microscopic dipole and for macroscopic polarization

it is extracted:

Knowing that polarization and electric field are related through the equation

the dielectric function, for just one type of transition is

where is the plasma frequency and is the oscillator strength factor. So for different resonances the real and imaginary part of the dielectric function, respectively and , are:

Generally this is a good approximation for semiconductor, insulators and for all metals which possess bound electrons (*d* or *p* valence electrons).

The following figure reports , and calculated for the Lorentz model

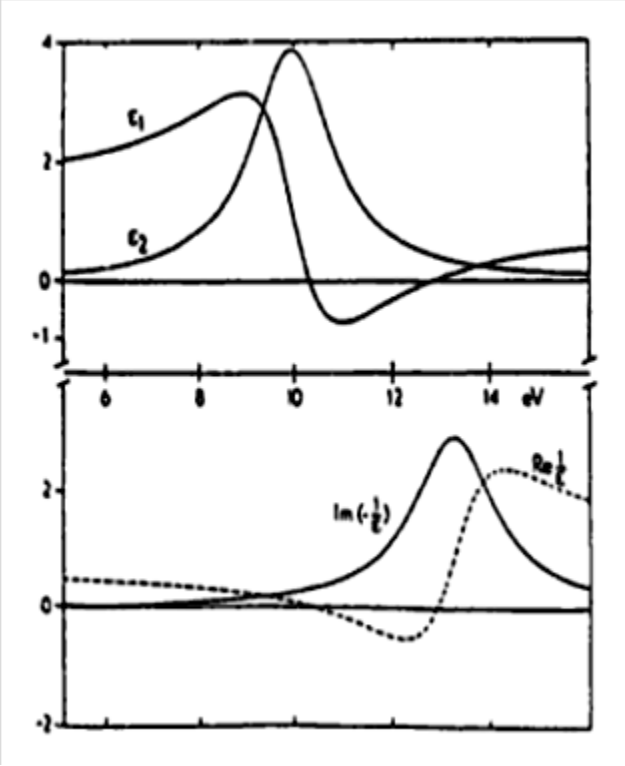

Figure 4.8 Real and imaginary part of the dielectric function ε (upper side) and real and imaginary part of 1/ ε (bottom side) for the Lorentz model.

In Figure 4.7, the peak in function represents an optical absorption at , while the loss function exhibits a maximum at a frequency > where and The occurrence of these conditions corresponds to a collective excitation in the solid known as "interband plasmon" in analogy to the free electron model.

More generally the behavior of metals is described by a dielectric function that is the sum of the intraband type (Drude model) and the interband type (Lorentz model). So the dielectric function is described by:

Observing trends of and for metals and semiconductors, it's clear that the maximum of these two function are never in the same energy position, on the contrary we can assume that the maximum of matches with the minimum of , like if

.

In conclusion this is the evidence that the single particle excitations and the collective excitations are generally in competition, making the EEL probability, in the range of 1-20 eV, inversely proportional to the optical absorption.

4.4.4 EELS in reflection geometry:

The schematic representation of the EELS in reflection geometry is shown in the following figure:

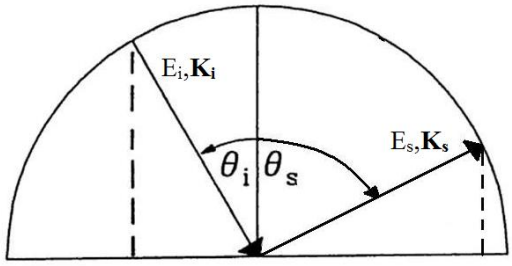

Figure 4.9 EELS reflection geometry representation

We assume that an electron with energy and wave vector hits the sample at an angle of incidence with respect to the surface normal and it scatters off the crystal with energy and wave vector at an angle .

We are describing an inelastic process, so the incident electron can transfer energy ( ) and momentum ( ) to the sample. From the conservation rule of energy we know that:

The conservation of the component parallel to the surface of the momentum is more restrictive, in fact just the component parallel to the surface must be preserved. So, we have:

Therefore, the component parallel to the surface of the momentum transfer is calculated as:

Taking into account the relation between the energy and the momentum for a free electron — we can calculate :

Thus, using monochromatic electron beam with a rotating analyzer it is possible, for each loss energy, calculate the component parallel to the surface of the momentum transfer obtaining the energy dispersion curve of the observed loss .

4.5 Experimental study of InSe compound

4.5.1 Introduction

Graphene has opened up prospects for a number of emerging technologies in areas of flexible electronics, photonics, and energy storage. A recent surge of interest in two dimensional (2D) crystals beyond graphene, is justified given their newly found remarkable properties that establish them as a distinct class of materials with unique technological potential. Particular attention is paid to the materials containing a metal of group III (Al, Ga, In or Tl) and an element of group VI (chalcogen). Due to their interesting optical properties, III–VI materials are considered as promising candidates for many technological applications and have shown their potential in optoelectronic and photo-electrochemical domains [6]. Four requisites are crucial for a suitable use of 2D materials in nanotechnology: (*i*) high mobility of charge carriers; (*ii*) the possibility to achieve highly crystalline samples via mechanical/liquid exfoliation; (*iii*) ambient stability; (*iv*) high flexibility together with a sufficiently high fracture toughness.

Among the chalcogenides of III–VI elements, we focus in this chapter on indium-selenide (InSe) compound. Contrary to III–V and II–VI semiconductors, InSe compound was not in the main stream of semiconductor literature and only a few experimental studies have been reported regarding their electrical conductivity [7], optical absorption [8],

reflectivity infrared spectrum [9] photoluminescence spectrum at low-temperature [10], and photon-electric and carrier properties [11], while experimental investigations no have been reported on their electronic excitations.

The proper selection of promising materials for a wide range of applications will require basic understanding of the electronic properties, as well as structural information so as to allow the concrete prospects to produce reliable devices for high-volume manufacturing.

The present study is aimed at investigate the collective excitations of InSe semiconductor, and to explore its chemical inertness.

4.5.2 Electronic properties of InSe: State of the art

Finite and direct band gaps are desirable for a wealth of applications, including transparent optoelectronics, photovoltaics, and photodetection. As an example, the performance of graphene detectors in the visible is strongly limited by the large dark currents that dominate under non-zero bias operation [12, 13]. Transition-metal dichalcogenides (TMDCs) as well as MoS_2 $MoSe_2$, WS_2, WSe_2, etc have recently emerged as a valuable alternative [14]. Two dimensional TMDCs can be obtained from bulk crystals by employing the micromechanical exfoliation method [15], like for the case of graphene, but they show **a direct band gap (0.4–2.3 eV)**, which enables applications that well complement graphene capabilities [16]. In particular, 2D TMDCs are suitable for photovoltaic applications [17] and for devising robust ultrathin-body field-effect transistor (FET) architectures [18] which can easily provide subthreshold swings of ≈60 mV dec^{-1}

and I_{on}/I_{off} ratios up to 10^8. On the other hand, their relatively low mobility ($\leq$200 $cm^2\ V^{-1}\ s^{-1}$) remains a major constraint for high frequency electronic applications.

A good trade-off between graphene and TMDCs is represented by a novel class of atomically thin 2D elemental materials: silicene [19], germanene [20], and phosphorene [21].

Both, silicene and germanene, bond easily with other materials and may oxidize rapidly in air. Therefore they are more challenging to fabricate than graphene because these require techniques such as epitaxial growth under ultra-high vacuum. [22]

Unlike silicon and germanium, black phosphorus (BP), the most stable allotrope of the phosphorus element in standard conditions, shows a layered graphite-like structure, where atomic planes are held together by weak Van der Waals forces of attraction, thus allowing the application of standard micro-mechanical exfoliation techniques.

As in graphene, each BP atom is connected to three neighbors, forming a stable layered honeycomb structure with an interlayer spacing of ≈5.3 Å. Bulk BP has a small direct band gap of ≈0.3 eV; the reduction of the flake thickness leads to quantum confinement which further enhances the gap up to $E_g \approx 1.0$ eV in the limit case of phosphorene (a single layer of BP). As a result, the I_{on}/I_{off} ratio of a BP-based FET can be improved by employing thinner flakes: an I_{on}/I_{off} ratio of $\approx 10^5$ has been recently reported in back-gated FET structures [16]. On the other hand, thickness reduction is detrimental for carrier mobility: thinner flakes are more vulnerable to scattering by interface impurities [23] and the effective mass of charge carriers increases when the number of atomic layers is reduced. [24] Despite this, BP thin films are endowed with hole mobilities exceeding

650 $cm^2 V^{-1} s^{-1}$ at room temperature and well above 1000 $cm^2 V^{-1} s^{-1}$ at 120 K, [25] thus overtaking the limiting factor of large-gap TMDCs and allowing to reach high-frequency operation up to 20 GHz. [26] For all the reasons above, BP represents a good material for infrared optoelectronic applications [27] and high-speed thin film electronics, [26] but its reactivity to contaminants creates many problem to applications in not controlled environments.

The next goal would be to find a material with similar characteristics of BP (mechanical exfoliation, not zero energy gap and high electrons mobility) and also chemically inert with respect to the external environment.

A suitable candidate for nanoelectronics is represented by InSe, which is a layered semiconductor made of stacked layers of Se-In-In-Se atoms with van der Waals bonding between quadruple layers [28, 29]. Recently, many works reported the superb performance of InSe-based optoelectronic devices [21, 30, 31].

Field effect transistors with an active channel of InSe are characterized by an electron mobility near 10^3 $cm^2/(V\ s)$ [30] and, moreover, excellent flexibility [32, 33] and ambient stability [34], in spite of the presence of a *p*-type doping arising from water decomposition at Se vacancies [34]. Furthermore, InSe is also a promising material for strain engineering [35], nonlinear optics [36], and photovoltaics [32]. Also the applications in polymer Schottky diodes, microbatteries, capacitors, infrared devices [37-40], have demonstrated the potential of InSe for future technologies. Different methods are employed

to synthesize InSe namely vapor deposition, spray pyrolysis, chemical vapor deposition, molecular beam epitaxy, chemical bath deposition [41-45].

Depending on the stacking characteristics, three different polytypes (β, ε, γ) of bulk InSe exist [46, 47]. The β (space group symmetry) and ε (space group symmetry) polytypes are characterized by a hexagonal lattice consisting of eight atoms in the unit cell and extending over two layers [48], whereas rhombohedral γ-polytype (space group symmetry) contains two cations and two anions distributed on four adjacent layers [46, 49].

While ε-InSe has an indirect band gap of 1.4 eV [47], both β-InSe and γ-InSe have a direct band gap [47] with nearly identical values of the band gap (1.28 [48] and 1.29 [50] eV, respectively). Thus, only β and γ phases of InSe can be, in principle, used for optoelectronic devices, for which finite and direct band gaps are highly desired [51,52].

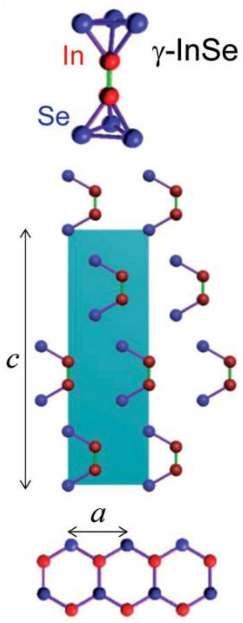

Figure 4.10 Crystal structure of γ -rhombohedral InSe.

The simplest and most frequently described polytypes are β and γ. The primitive unit cell of γ-InSe shown in Figure 4.10, has a lattice parameter c = 24.961 Å (along the c -axis) and contains three layers, each consisting of four closely-packed, covalently bonded, monoatomic sheets in the sequence Se-In-In-Se. Within each plane, atoms form hexagons with lattice parameter a = 4.002 Å.

From Hall effect measurements on bulk γ-InSe at T = 300 K, was obtained an electron density $n\approx$, an electron mobility μ = 0.1 , and a Fermi energy ≈ 0.21 eV below the conduction band minimum.[53]

Instead the primitive unite cell of β-InSe has c = 16.88 Å and contains only two hexagonal layers (Se-In-In-Se) with lattice parameter a = 4.00 Å [54]. There are eight atoms in the unit cell of β-InSe which belong to two translationally non-equivalent layers with Se–In–In–Se structure. The crystal structure of the most symmetric, β modification, is presented in Figure 4.11.

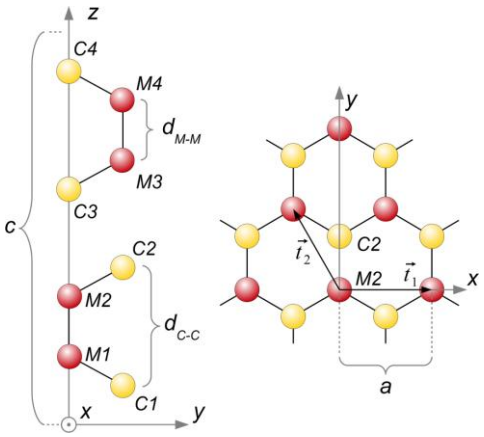

Figure 4.11 The atomic structure of β – type of III-VI compound family.

High-quality samples of β-InSe can be grown by modified Bridgman–Stockbarger method [48]. The possibility to exfoliate β-InSe nanoflakes from a parental bulk single crystal makes this phase suitable for up-scaling, due to the higher ease of the nanofabrication process.

We report a study on the electronic properties of β-InSe by spectroscopy techniques detailed in previous sections of this chapter (LEED, XPS and EELS).

4.5.3 Sample characterization by LEED and XPS:

A single crystalline slab of β-InSe, grown by Bridgman-Stockbarger method by foreign collaborators, has been cleaved in-situ by micromechanical cleavage. To investigate surface **cleanliness and order**, X-Ray photoelectron spectroscopy and low-energy electron diffraction experiments have been performed.

The LEED pattern of the as-cleaved sample of β-InSe acquired with an impinging electron energy of 100 eV is reported in Figure 4.12. The diffraction pattern clearly indicates the hexagonal arrangement of atoms in the surface and the absence of diffused light is an evident sign of the high crystalline quality of the samples.

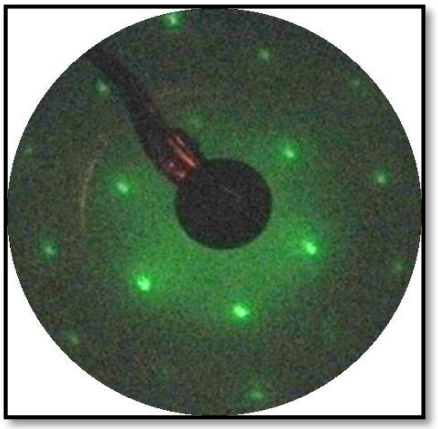

Figure 4.12 LEED pattern of the InSe sample.

For XPS experiments, we used the emissions of a magnesium X-ray source. Photoelectrons, emitted by the sample, have been collected by a hemispherical electron analyzer (Figure 4.13). The angle between the X-Ray beam and the electron analyzer is 60°. The energy of the Mg emission is , so the XPS spectrum is reported in binding energy through the equation (1).

(1)

The XPS spectrum of the β-InSe surface is shown in Figure 16. The predominant peaks in the XPS spectrum are core levels and the MNN Auger peak of In and the , and peaks ( ) of Se. Structures related to oxygen, carbon and tantalum elements are also present, as indicated by the existence of O-1s and C-1s core levels and O-KLL and C-KVV Auger peaks and a weak peak related to the Ta core level. These lower signals were recorded from elements present on the sample holder and most likely they are not coming out from the β-InSe crystal.

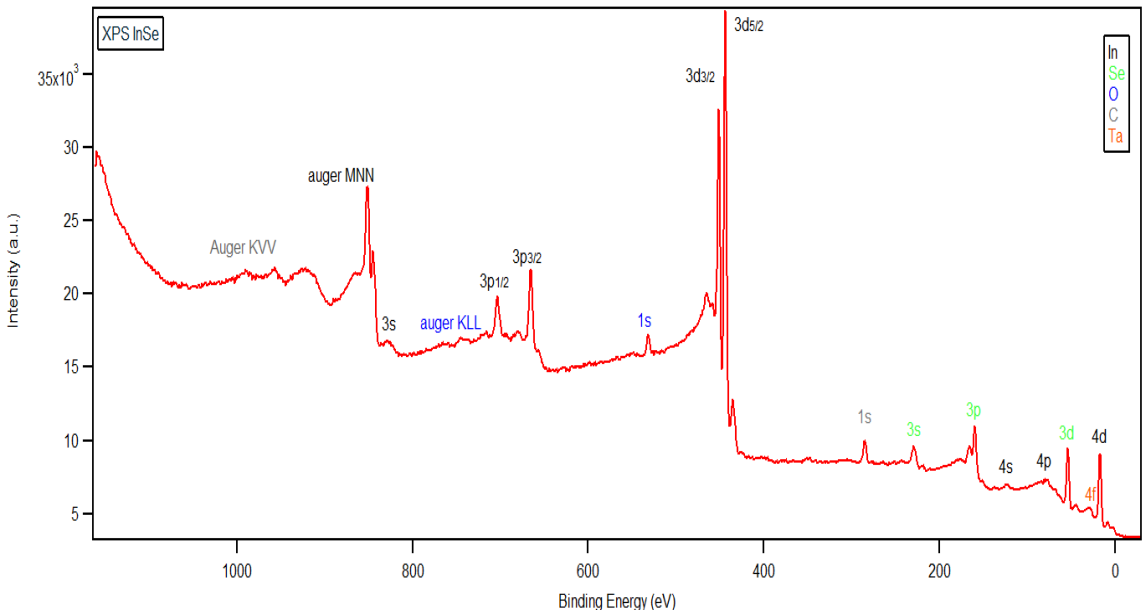

Figure 4.13 XPS spectrum (Mg K_α emission) of InSe.

4.5.4 Loss function probed by EELS and comparison with theory:

The angle-resolved EELS measurements were carried out at room temperature using an apparatus for HREELS with two 50 mm hemispherical deflectors both for monochromator and rotating analyzer. An average energy resolution of 60 meV was set to achieve the best signal-to-noise ratio. The incident electron beam was at a fixed angle of incidence = 43° with respect to the surface normal, with 100 eV kinetic energy (Figure 4.14). The momentum transfer component parallel to the surface was calculated from the following kinematic expression (2), which reflects the conservation of energy and of in-plane momentum

(2)

where is the energy of the primary electron beam, the loss energy, is the mass of the free electron, and are the angles with respect to the surface normal of the sample for incident and scattered electrons, respectively.

The EELS measurements were performed at different scattering angles, i.e., for different values of parallel momentum transfer $q_{||}$. The sample has been oriented along the

- direction of the surface Brillouin zone.

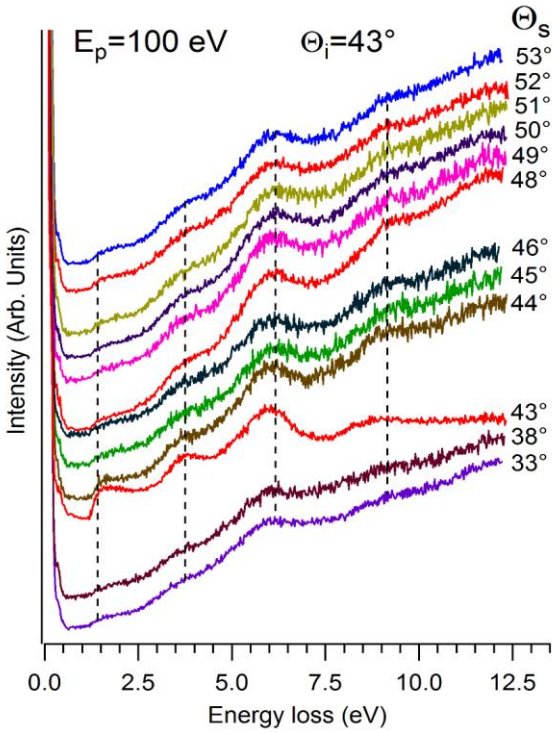

Figure 4.14 EELS spectra at different values of the scattering angle θs. The impinging energy is 100 eV.

The momentum-resolved EELS spectra of β-InSe sample are represented in figure 17 with, on the right side of each curves, the respective value of scattering angle|.

A prominent loss feature, located around 6 eV, dominates all spectra. Its energy position and intensity is nearly independent on $q_{||}$.

The dispersion ($q_{\parallel}$) of collective electronic excitations has a characteristic behavior. In the case of surface or volume plasmons of bulk samples, the plasmon dispersion curve shows a quadratic dependence of the momentum . In our case, we do not observe any dispersion relation, since the energy position of the peak at 6 eV does not change at different analyses angles, and therefore it is independent on the $q_{\parallel}$ value. Consequently, we can affirm that this excitation is not a "proper" plasmon mode but it is more likely a single-particle transition.

In our EELS measurements also less intense peaks around 2, 4 and 9 eV exist. They are also ascribed to single-particle excitations. To support this hypothesis, in Figure 4.15 we compare the energy of peaks in our EELS spectra with a DOS calculation provided by theoretical researchers who collaborated on this work.

The symmetry-projected DOS shows three distinct structures. The energetically lower VB is situated between -16 and -14 eV. The upper VB extends from -8 eV up to Fermi level E_F. The third region is that of the conduction band (CB). The state forming the bottom of VB has contributions from *s* states of Se, while the top of the VB has contributions from both *p* states of Se and *sp* states of In, with minor contribution from *p* states of In. The CB has *sp* character, with contributions from both In and Se.

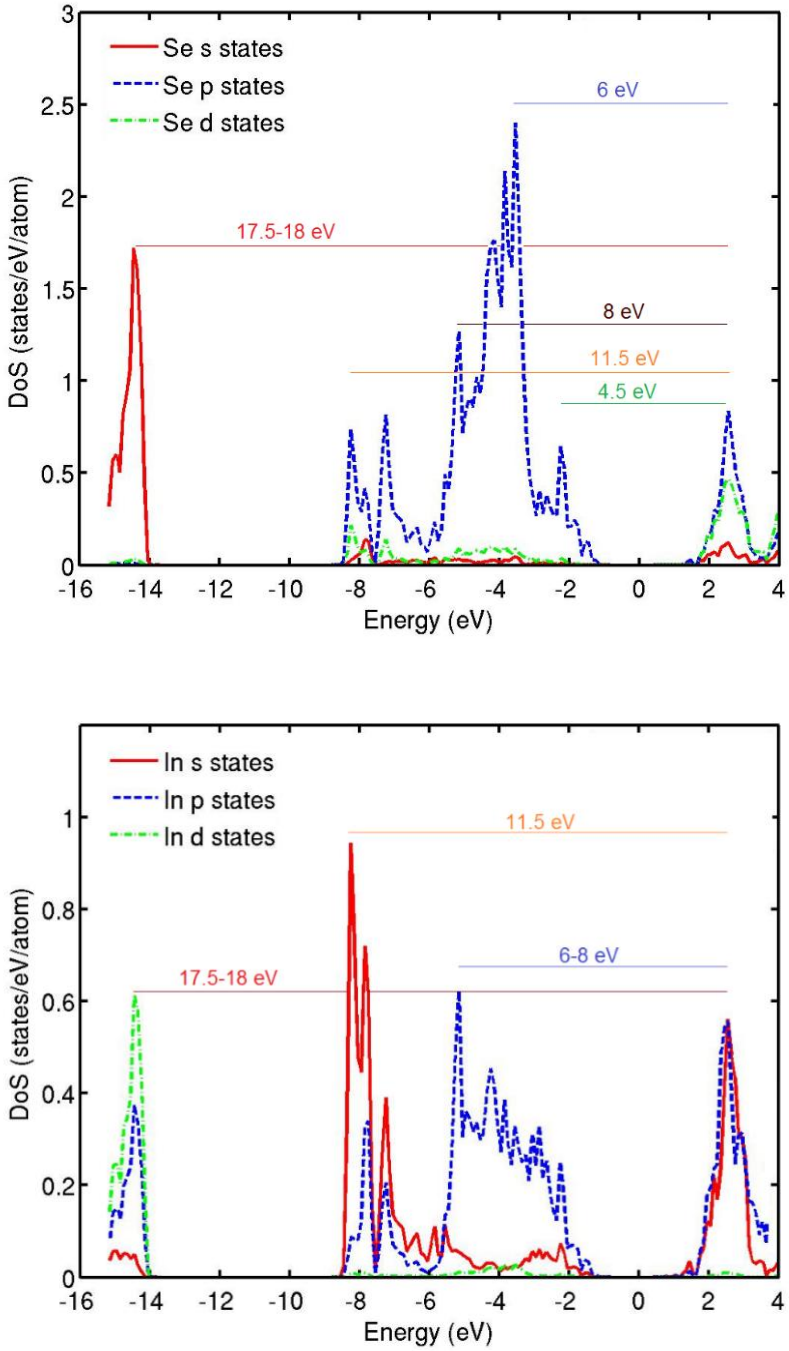

Figure 4.15 Single-particle transition energies, obtained from our EELS measurements, compared with theoretical DOS (calculated with HSE06) for Se- and In-derived states.

A good agreement between the DOS and modes observed in EELS is found. In details, the peak at a loss energy of ~6 V in EELS spectra should be related to a plasmon mode originated from transitions from the 5*p* states of In to unoccupied 6*s* states of In. The

loss peak at ~9 eV measured by EELS is derived from the same transition, with an additional spectral contribution from transitions from the 4*p* states of Se to unoccupied 5*d* states of Se. The inspection of the DOS suggests the possible occurrence of a mode around 4 eV, related to a transition from 4*p*-derived valence-band states of Se to the 5*d* CB states of Se. The corresponding interband excitation is observed in our EELS spectra at 3.8 eV.

We would like to point out that the energies of the EELS peaks cannot be exactly the same of optical transitions, since maxima in the loss function correspond to the maxima in —— . Conversely, optical transitions correspond to the maxima in [61], which are shifted compared to maxima of —— [52].

By increasing the impinging energy of the electron beam, it is possible to extend the excitation spectrum, including also modes at higher loss energies. Figure 4.16 reports the EELS spectra acquired at different values of E_p, ranging from 400 to 1000 eV, in an extended energy loss range (0-34 eV) with respect to EELS measurements at E_p=100 eV in Figure 4.16. We observe two additional peaks at 12 and 22 eV, while the mode at 8 eV has decreased weight, likely due to the modification of the cross-section for its excitation at higher values of E_p. The mode at 12 eV has the highest intensity in the EELS spectrum acquired with E_p in the 400-1000 eV range. By examining the theoretical DOS, we assign it to an interband excitation, originated from single-particle transitions with contribution from 5*s*→ 5*p* between In-derived states and from 4*p*→ 5*d* between Se-derived states. Moreover, the interplay of different excitations in the 11.5-17.5 eV range explains the broadness of the experimental peak, as well as its high intensity.

In our EELS spectra we observe also another feature around 1.4 eV. The line-shape of this mode suggests that it represents the onset of single-particle transitions from the highest occupied states to the lowest unoccupied electronic states. We thus suggest that this mode is related with the energy gap of InSe.

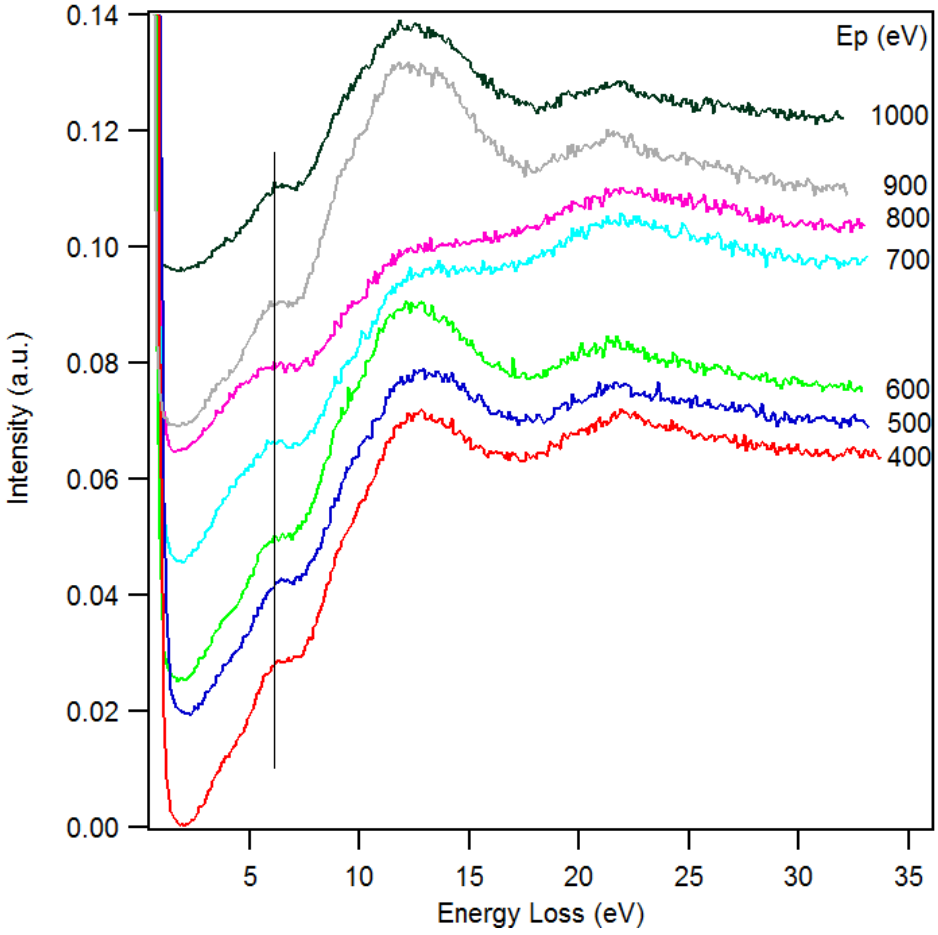

Figure 4.16 EELS spectra at different primary energies (Ep).

4.5.5 Surface chemical reactivity:

As already stated in introduction, we have chosen to work with InSe for its characteristics quite similar compared to phosphorene (mechanical exfoliation, finite energy gap and high hole mobility).

Ambient stability would be an essential prerequisite for up-scaling of InSe-based devices. In order to study the robustness of the InSe band structure, the sample, exfoliated in UHV conditions, was exposed to ~10^3 L (1 L=10^{-6} torr·s) of O_2 and to air at room temperature. All EELS experiments and exposures have been made at room temperature. The impinging energy is 100 eV. The incidence and the scattering angles are 43° with respect to the sample normal.

In Figure 4.17 the evolution of the loss function upon O_2 and air exposure is shown. No perceptible change can be appreciated by EELS, even after 24 hours in air, except a slight modification of the background.

On the basis of EELS data in Figure 4.17, we can affirm that the β-InSe sample is stable in atmospheric conditions and scarcely reactive to ambient gases, due to the protection of the Se termination of the crystal. By contrast, rapid surface degradation in ambient conditions has been reported for the cases of black phosphorus [55], Bi_2Se_3 [56], and MoS_2 [57].

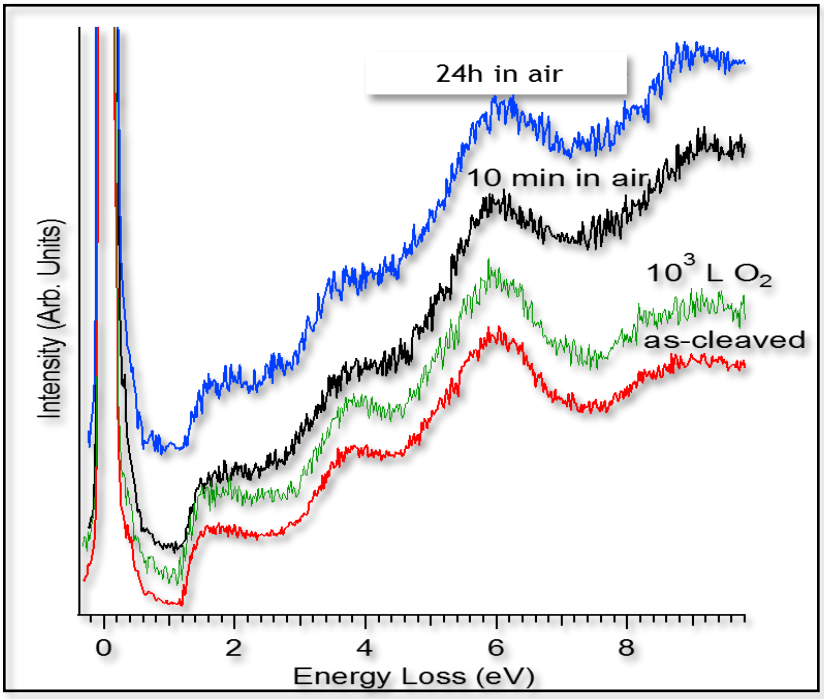

Figure 4.17 Evolution of the loss function of the as-cleaved InSe sample (red curve) upon exposure to O2 (10^3 L, green curve) and after 10 minutes (black curve) and 24 h (blue curve) in air.

4.6 Conclusions

We report the first experimental characterization of the electronic properties of InSe measured by Electron Energy Loss Spectroscopy.

Electronic excitations of InSe bulk crystal have been investigated for different energy ranges both at low and high resolution mode. The origin of electronic transitions measured by EEL spectroscopy have been identified by analyzing the total and partial densities of states (DOS and pDOS). The loss function, probed by EELS, shows several dispersionless features, all ascribed to single-particle excitations, originated from interband

transitions. The absence of plasmon dispersion is due to the flatness of the bands involved in the transitions.

In addition, we find that the band structure is stable in ambient conditions without the emergence of oxygen- or water-induced adsorbate electronic states. Ambient stability is crucial in the prospect of InSe-based nanoelectronics and optoelectronics. These results make InSe a challenging material for applications, which should work under realistic conditions.

4.7 References

[1] A.A. Lucas and M. Sunjic, Fast Electron Spectroscopy of Surface Excitations, Phys. Rev. Lett. 26, 229 (1971).

[2] E. Evans and D.L.Mills, Theory of inelastic scattering of slow electrons length surface optical phonons, Phys. Rev. B 5, 4126 (1972).

[3] Evans and D.L.Mills, Phys. Rev. B 7 853 (1973).

[4] D.L Mills, Surf. Sci. 48, 59 (1975).

[5] F. Wooten "Optical Properties of Solids". Acc. Press, N.Y. (1972)

[6] K. Hara, K. Sayama, H. Arakawa, Sol. Energy Mater. Sol. Cells 62, 441(2000).

[7] T. Nishino, Y. Hamakawa, J.Appl.Phys.16, 1291 (1977).

[8] K. Takarabe, H. Kawamura, K. Wakamura, Phys.Status Solidi B 142, 605 (1987).

[9] F. E. Faradev, N.M. Gasanly, B. N. Mavrin, N. N. Melnik, Phys. Status Solidi B 85, 381 (1978).

[10] N. M. Gasanly, A. Aydinli, Solid State Commun. 101, 797 (1997).

[11] A. F. Qasrawi, N. M. Gasantly, Semicond. Sci. Technol. 17, 1288 (2002).

[12] X. Gan, R.-J. Shiue, Y. Gao, I. Meric , T. F. Heinz, K. Shepard, J. Hone, S. Assefa, D. Englund, Nat. Photonics, 7, 883 (2013).

[13] F. H. L. Koppens, T. Mueller, Ph. Avouris, A. C. Ferrari, M. S. Vitiello, M. Polini, Nat. Nanotechnol., 9, 780 (2014).

[14] Q. H. Wang, K. Kalantar-Zadeh, A. Kis, J. N. Coleman, M. S. Strano, Nat. Nanotechnol., 7, 699 (2012).

[15] F. Bonaccorso, A. Lombardo, T. Hasan, Z. Sun, L. Colombo, A. C. Ferrari, Mater. Today, 15, 12 (2012).

[16] S. Das, W. Zhang, M. Demarteau, A. Hoffmann, M. Dubey, A. Roelofs, Nano Lett., 14 5733 (2014).

[17] L. Britnell, R. M. Ribeiro, A. Eckmann , R. Jalil , B. D. Belle , A. Mishchenko, Y. J. Kim, R. V. Gorbachev, T. Georgiou, S. V. Morozov, Science, 340, 1311 (2013).

[18] H. Fang , M. Tosun , G. Seol , T. C. Chang , K. Takei , J. Guo , A. Javey , Nano Lett., 13, 1991 (2013).

[19] M. Houssa, A. Dimoulas, A. Molle, J. Phys.: Condens. Matter, 27, 253002 (2015).

[20] M. Derivaz, D. Dentel, R. Stephan, M. C. Hanf, A. Mehdaoui, P. Sonnet, C. Pirri, Nano Lett., 15, 2510 (2015).

[21] H. Liu , A. T. Neal , Z. Zhu , Z. Luo , X. Xu , D. Tomanek , P. D. Ye , ACS Nano, 8, 4033 (2014).

[22] P. Vogt, De Padova, C. Quaresima, J. Avila, E. Frantzeskakis, M. C. Asensio, A. Resta, B. Ealet, G. Le, Phys. Rev. Lett. 108, 155501 (2012).

[23] L. Li , Y. Yu , G. J. Ye , Q. Ge , X. Ou , H. Wu , D. Feng , X. H. Chen ,Y. Zhang , Nat. Nanotechnol., 9, 372 (2014).

[24] Y. Cai, G. Zhang, Y.-W. Zhang, Sci. Rep., 9, 6677 (2014).

[25] F. Xia, H. Wang, Y. Jia, Nat. Commun. 5, 4458 (2014).

[26] H. Wang, X. Wang, F. Xia, L. Wang, H. Jiang, Q. Xia, M. L. Chin, M. Dubey, S.-J. Han, Nano Lett., 14, 6424 (2014).

[27] M. Buscema, D. J. Groenendijk, S. I. Blanter, G. A. Steele, H. S. J. van der Zant, A. Castellanos-Gomez, Nano Lett., 14, 3347 (2014).

[28] J. F. Sánchez-Royo, G. Muñoz-Matutano, M. Brotons-Gisbert, J. P. Martínez-Pastor, A. Segura, A. Cantarero, R. Mata, J. Canet-Ferrer, G. Tobias, E. Canadell, J. Marqués-Hueso, B. D. Gerardot, Nano Res., 7, 1556 (2014).

[29] C. H. Ho, 2D Materials, 3, 025019 (2016).

[30] S. Sucharitakul, N. J. Goble, U. R. Kumar, R. Z. A. Sankar, Bogorad, F.-C. Chou, Y.-T. Chen, X. P. A. Gao, Nano Lett. 15, 3815 (2015).

[31] Lei, S.;Wen, F.;Ge, L.;Najmaei, S.;George, A.;Gong, Y.;Gao, W.;Jin, Z.;Li, B.;Lou, J.;Kono, J.;Vajtai, R.;Ajayan, P.; Halas, N. J. Nano Lett., 15 (2015) 3048.

[32] C. H. Ho, Y. J.Chu, Advanced Optical Materials, 3, 1750 (2015).

[33] Tamalampudi, S. R.;Lu, Y. Y.;Kumar, R.;Sankar, R.;Liao, C. D.;Moorthy, K.;Cheng, C. H.;Chou, F. C.; Chen, Y. T. Nano Lett., 14, 2800 (2014).

[34] Politano, A.;Chiarello, G.;Samnakay, R.;Liu, G.;Gurbulak, B.;Duman, S.;Balandin, A. A.; Boukhvalov, D. W. Nanoscale, 8, 8474 (2016).

[35] Yandong, M.;Ying, D.;Lin, Y.;Chengwang, N.; Baibiao, H. New J. Phys., 15, 073008 (2013).

[36] Yüksek, M.;Yaglioglu, H. G.;Elmali, A.;Aydin, E. M.;Kürüm, U.; Ateş, A.; Opt. Commun., 310, 100 (2014).

[37] T. Mueller, F. Xia and P. Avouris, Nat. Photonics, 4, 297 (2010).

[38] A. Pospischil, M. Humer, M. M. Furchi, D. Bachmann, R. Guider, T. Fromherz and T. Mueller, Nat. Photonics, 7, 892 (2013).

[39] B. Radisavljevic, M. B. Whitwick and A. Kis, ACS Nano, 5, 9934 (2011).

[40] Y. Yoon, K. Ganapathi and S. Salahuddin, Nano Lett., 11, 3768 (2011).

[41] B. Radisavljevic, A. Radenovic, J. Brivio, V. Giacometti and Kis, Nat. Nanotechnol., 6, 147 (2011).

[42] D. J. Late, B. Liu, J. Luo, A. Yan, H. Matte, M. Grayson, C. Rao and V. P. Dravid, Adv. Mater., 24, 3549 (2012).

[43] P. Hu, Z. Wen, L. Wang, P. Tan and K. Xiao, ACS Nano, 6, 5988 (2012).

[44] P. Hu, L. Wang, M. Yoon, J. Zhang, W. Feng, X. Wang,Z. Wen, J. C. Idrobo, Y. Miyamoto and D. B. Geohegan, NanoLett., 13, 1649 (2013).

[45] L. Liao, Y.-C. Lin, M. Bao, R. Cheng, J. Bai, Y. Liu, Y. Qu,K. L. Wang, Y. Huang and X. Duan, Nature, 467, 305 (2010).

[46] Han, G.; Chen, Z.-G.; Drennan, J.; Zou, J. Small, 10, 2747 (2014).

[47] Lei, S.; Ge, L.; Najmaei, S.; George, A.; Kappera, R.; Lou, J.; Chhowalla, M.; Yamaguchi, H.; Gupta, G.; Vajtai, R.; Mohite, A. D.; Ajayan, P. M.; ACS Nano, 8, 1263 (2014).

[48] Gürbulak, B.;Şata, M.;Dogan, S.;Duman, S.;Ashkhasi, A.; Keskenler, E. F. Physica E, 64, 106 (2014).

[49] Mudd, G. W.;Patanè, A.;Kudrynskyi, Z. R.;Fay, M. W.;Makarovsky, O.;Eaves, L.;Kovalyuk, Z. D.;Zólyomi, V.; Falko, V. Appl. Phys. Lett., 105 (2014).

[50] Julien, C. M.; Balkanski, M. Materials Science and Engineering: B, 100 263 (2003).

[51] Zhao, H.; Guo, Q.; Xia, F.; Wang, H. Nanophotonics, 4 (2015).

[52] Viti, L.; Hu, J.; Coquillat, D.; Knap, W.; Tredicucci, A.; Politano, A.; Vitiello, M. S. Adv. Mater., 27, 5567 (2015).

[53] Garry W. Mudd , et al. Adv. Mater., 27, 3760 (2015).

[54] J. P. Perdew, K. Burke, and M. Ernzerhof, Phys. Rev. Lett. 77, 3865 (1996).

[55] Island, J. O.; Steele, G. A.; van der Zant, H. S. J.; Castellanos-Gomez, A. 2D Materials, 2, 011002 (2015).

[56] Kong, D.; Cha, J. J.; Lai, K.; Peng, H.; Analytis, J. G.; Meister, S.; Chen, Y.; Zhang, H. J.; Fisher, I. R.; Shen, Z. X.; Cui, Y. ACS Nano, 5, 4698 (2011).

[57] Jariwala, D.; Sangwan, V. K.; Late, D. J.; Johns, J. E.; Dravid, V. P.; Marks, T. J.; Lauhon, L. J.; Hersam, M. C. Appl. Phys. Lett., 102, 173107 (2013).

Accomplishments

Papers published/submitted

D. Coello-Fiallos, C. Vacacela Gómez, and G. Tubón Usca D. Cid Pérez P. Tavolaro G. Martino L. S. Caputi A. Tavolaro, Removal of acridine orange from water by graphene oxide, AIP Conference Proceedings, 1646, 38 (2015); http://doi.org/10.1063/1.4908580.

G. Tubón Usca, C. Vacacela Gómez, D. Coello Fiallos, P. Tavolaro, G. Martino, L. S. Caputi, Preparation of graphene oxide as biomaterials for drug adsorption, AIP Conference Proceedings 1646, 79 (2015); http://doi.org/10.1063/1.4908586.

D. Coello-Fiallos, E. Cazzanelli, A. Tavolaro, P. Tavolaro, M. Arias and L.S. Caputi, Cresyl violet adsorption on sonicated graphite oxide, Journal of Nanoscience and Nanotechnology, **accepted**.

D. Coello-Fiallos, T. Tene, J. L. Guayllas, D. Haro, A. Haro, C. Vacacela Gomez, DFT comparison of structural and electronic properties of graphene and germanene: monolayer and bilayer systems, **submitted.**

Conferences

1. 11th International Conference on Nanosciences & Nanotechnologies (NN14).
2. International Conference on Diamond and Carbon Materials.
3. NanotechITALY2014 Cross-Cutting KETs for Responsible Innovation.
4. 6th Czech-Italian-Spanish Conference on Molecular Sieves and Catalysis (CIS6).
5. GIC2015 (XVII NATIONAL Congress of Catalysis.
6. AIZ2015 XII National Congress of Zeolites Science and Technology.
7. International Conference NanotechITALY2015s Cross-Cutting KETs for Responsible Innovation.
8. 13th International Conference on Nanosciences & Nanotechnologies (NN16)

Seminars/Capacitations

1. MEMBRANE MATERIALS BASED ON POLYMERS OF INTRINSIC MESOPOROSITY (PIMs) AND GRAPHENE

2. Percorso Informativo in Materia di Innovazione, Ricerca e Transferimento Tecnologico.

3. “ARMONICAMENTE” Arte e Scienza a confronto.

4. Scuola per Dottorato “LNF Test Labs” (LTL-2014): Laser, Synchrotron Radiation and Particle Beam Test Facilities at LNF.

5. Scuola per Dottorato “LNF/Cs Test Laboratories” (LTL-2014): Science and Technologies at UNICAL.

6. NDRA 2016 Summer School on Neutron Detectors and Related Applications